UNIVERSITY OF SOUTHAMPTON

FACULTY OF ENGINEERING, SCIENCE AND MATHEMATICS

School of Physics and Astronomy

Point Contact Studies of Rare Earth – Transition Metal Compounds

by

Christopher Glen Morrison

Thesis for the degree of Doctor of Philosophy

May 2009

UNIVERSITY OF SOUTHAMPTON

ABSTRACT

FACULTY OF ENGINEERING, SCIENCE AND MATHEMATICS
SCHOOL OF PHYSICS AND ASTRONOMY

Doctor of Philosophy

POINT CONTACT STUDIES OF RARE EARTH – TRANSITION METAL COMPOUNDS

by Christopher Glen Morrison

Mechanical point contact techniques have been used to study the spin-dependent properties of rare earth-transition metal compounds and transition metal thin films and bi-layers. The transport spin polarisation of Cu, Co and Fe has been measured using point contact Andreev reflection (PCAR), and found to be in good agreement with previous results. In addition, bi-layers of Co/Y and Co/Cu have been used to demonstrate suppression of the spin polarisation of the Co underlayer via a non-magnetic capping layer. The spin diffusion length of Cu has been estimated to be larger than 600nm. The spin polarisation of molecular beam epitaxy (MBE) deposited RFe_2 (R = Dy,Y,Er) Laves phase intermetallic films was determined, and found to be close to that of Fe. This suggests that the spin transport behaviour in these materials is dominated by the Fe sub-lattice. Preliminary evidence for spin transfer torque effects in an RFe_2 multilayer and tri-layer is also presented and discussed. Point contact measurements of an $ErFe_2/YFe_2$ multilayer at 4.2K show a step in the differential resistance at a positive current value. It is suggested that this is due to the formation of a nano-domain beneath the tip. Measurements of a $DyFe_2/YFe_2/DyFe_2$ tri-layer show peaks in differential resistance for negative applied currents. This is tentatively attributed to the generation of spin waves within the YFe_2 layer.

DECLARATION OF AUTHORSHIP

I, Christopher Glen Morrison,

declare that the thesis entitled

Point Contact Studies of Rare Earth – Transition Metal Compounds

and the work presented in the thesis are both my own, and have been generated by me as the result of my own original research. I confirm that:

- this work was done wholly or mainly while in candidature for a research degree at this University;
- where any part of this thesis has previously been submitted for a degree or any other qualification at this University or any other institution, this has been clearly stated;
- where I have consulted the published work of others, this is always clearly attributed;
- where I have quoted from the work of others, the source is always given. With the exception of such quotations, this thesis is entirely my own work;
- I have acknowledged all main sources of help;
- where the thesis is based on work done by myself jointly with others, I have made clear exactly what was done by others and what I have contributed myself;
- parts of this work have been published as:

Determination of the Spin Polarization of $DyFe_2$ and YFe_2 Epitaxial Films by Point Contact Andreev Reflection
C. G. Morrison, D. Wang, G. J. Bowden, R. C. C. Ward and P. A. J. de Groot, submitted to *J. Magn. Magn. Mater.* (2009)

Signed: ……..

Date:……

Acknowledgements

Firstly, I would like to thank my supervisor Prof. Peter de Groot for his help and guidance throughout my research project. I would also like to thank my advisor Prof. Graham Bowden for his suggestions and useful discussions. I wish to thank Kevin Martin and Sasha Zhukov for showing me how to use the equipment, and Kevin in particular for his company during our experimental work in Grenoble. I would like to thank Daowei Wang for his assistance with Matlab and for interesting discussions, and I would also like to thank Roger Buckingham and Prof. Alan Fox for their stimulating conversation.

Finally, and on a more personal note, I would like to thank my partner Emma for her untiring support during my time as a research student at Southampton, and for her understanding regarding long and irregular working hours. I would also like to thank my parents Pat and Glen for their help and advice and for supporting me, whatever I choose to do in life.

Chapter 1: Introduction

Spintronics research has proceeded at a fast pace in recent years. Since the discovery of interlayer exchange coupling in magnetic nanostructures[1,2,3], magnetic multilayers have attracted much attention. This research lead to the discovery of giant magnetoresistance (GMR) independently by the groups of Fert and Grünberg in the late 1980s[4,5], which essentially launched the modern field of spintronics. Devices based on magnetic nanostructures have found applications in a wide range of devices, but most notably GMR-based hard disk drive read heads. This is due to their greatly increased sensitivity, which allows data to be stored at a higher density than their conventional counterparts. Recent advancements in thin film deposition technologies, in particular magnetron sputtering and molecular beam epitaxy (MBE), have also allowed an unprecedented range of materials to be studied, on very small length scales.

Rare earth – Transition metal (R-TM) materials are an interesting class of materials that have many useful magnetic properties. They possess both high magnetic anisotropy and a large saturation magnetisation, provided by the rare earth and the transition metal site respectively. When layered together in hard/soft magnetic phases, an exchange spring configuration can be formed, where the magnetisation of the soft layer 'winds up' in an applied magnetic field. Initially, interlayer exchange coupled R-TM hard/soft composites were proposed as candidates for improving the maximum energy product for permanent magnet applications[6,7]. More recently, exchange spring media have been proposed for applications in data storage, providing improved thermal stability while maintaining a low write field[8,9,10]. This allows continued improvement of areal density of data storage media while avoiding instability and data loss due to the superparamagnetic effect.

There is an active programme of research at the University of Southampton focussing on R-TM exchange spring multilayer systems and the exotic magnetic behaviour they exhibit. Recently, emphasis has been on the spin transport behaviour of

these multilayers, as a model system for applications in spintronics. An important parameter in spintronic devices is the spin polarisation of the component layers, and this may be measured, among other techniques, by using point contact Andreev reflection.

The aim of the work presented in this thesis is to study the spin properties of rare earth – transition metal thin films and multilayers through point contact techniques. In particular, the transport spin polarisation of three R-TM intermetallics ($DyFe_2$, YFe_2 and $ErFe_2$) is determined using point contact Andreev reflection. This project builds on extensive previous research into multilayers comprising of composites of the above materials. Exchange spring multilayers consisting of alternating $DyFe_2/YFe_2$ layers have been used to demonstrate (i) GMR, with exchange spring magnetoresistance of 32%[11], (ii) tunable coercivity and spring bending field[12,13] and (iii) negative coercivity[14], where the exchange spring unwinds before reversal of the applied field direction. More recently, $ErFe_2/YFe_2$ multilayers have revealed exotic spin flop behaviour, where the normally perpendicular-to-plane $ErFe_2$ moment flops into an in-plane direction under application of a high magnetic field[15]. In addition, it has been shown that the anomalous Hall effect (AHE) is driven primarily by the Fe sub-lattice[16].

In Chapter 2 of this thesis an overview is presented of some of the most notable research undertaken in the field of spintronics, including GMR, interlayer exchange coupling, and spin transfer torque. In section 2.2 a brief description is given of exchange spring magnetism and related research. In Section 2.3 the specifics of the magnetism of R-TM intermetallic materials are described, from the perspective of exchange interactions, and the magnetocrystalline anisotropy observed in these materials. In addition the role played by strain, induced during MBE deposition, is also described, since this gives rise to a reorientation of the magnetocrystalline easy axes in these materials.

In chapter 3 the physics relevant to point contact techniques are briefly outlined. Section 3.1 contains a concise history of research into point contact junctions, followed by a description of the various regimes in which point contacts can be characterized, typically by the radius of the contact. In section 3.2 the theory of

Andreev reflection is presented, starting with the widely accepted Blonder-Tinkham-Klapwijk (BTK) model, and its modification to describe spin polarised materials. Finally, a summary is given of notable point contact Andreev reflection (PCAR) results.

The experimental techniques and equipment used to obtain the results presented in this thesis are presented in chapter 4. In particular, the superconducting magnet inserts, built for the purpose of making low temperature measurements of point contact junctions in high magnetic fields, are described in some detail, alongside the electronics used to make and record these differential conductance measurements. The operation and specification of a Leo 1455 VP Scanning Electron Microscope (SEM) system is also described, since this microscope was used for characterization of both thin films and mechanically polished metal tips. Finally, details are given of the MBE setup used to deposit thin films and multilayers with near-atomic sharpness, and operation of a DC magnetron sputtering system, used for rapid prototyping of metal films and bi-layers.

In chapter 5 point contact Andreev reflection (PCAR) measurements of simple transition metal films are presented and discussed. These measurements were performed as a precursor to the measurement of bi-layers and R-TM films presented in subsequent chapters. PCAR measurements of a Cu film demonstrate an almost 100% enhancement of zero bias conductance, moreover by fitting to a model of spin polarised Andreev reflection, this allows confirmation of zero transport spin polarisation in the non-magnetic metal. Finally, subsequent measurements of Co and Fe films show a high degree of spin polarisation, consistent with the findings of previous workers.

PCAR measurements carried out on bi-layers of both Co/Y and Co/Cu are presented in chapter 6. These results show suppression of the spin polarisation of the Co under-layer through sufficient non-magnetic material. These results are important for the Laves phase intermetallics discussed in chapter 7, since these are capped with a thin layer of Y to prevent oxidation. Analysis of curves from Co/Cu bi-layers of varying Cu layer thickness allows an estimate to be made of the spin diffusion length

in Cu, which in turn allows estimates to be made of the reliability of PCAR measurements, as a whole.

PCAR measurements of R-TM ($DyFe_2$, YFe_2 and $ErFe_2$) MBE-grown films are presented in chapter 7. Experimental curves are presented, and compared to a model of spin polarised Andreev reflection, thus allowing the transport spin polarisation to be determined with an accuracy of 1-2%. Additional features are observed in the experimental curves at high bias voltages. A potential explanation for these features is given, based on critical current and critical field hypotheses. Application of an external magnetic field allows an estimate to be made of the local upper critical field H_{c3}. Further, measurements carried out at varying temperatures reveal the temperature dependence of the additional features mentioned above.

In chapter 8 some preliminary experiments demonstrating spin transfer phenomena under spin-polarised currents are reported. Magnetoresistance features are observed at the switching field of the hard $ErFe_2$ layers in an $ErFe_2$ / YFe_2 multilayer. This can be explained by a model of localised spin transfer at the tip causing the creation of a nanodomain with associated domain walls, inducing domain wall magnetoresistance. Peaks in differential resistance are observed in a $DyFe_2$ / YFe_2 / $DyFe_2$ tri-layer. These are attributed to spin wave excitation in the sample under the applied current. The observed peaks are independent of an applied magnetic field, suggesting that the generation of spin waves in this sample is largely dependent on the constraint imposed by the exchange spring.

Finally, a summary of the results is presented in chapter 9, together with a discussion of the main conclusions that can be drawn from this work.

Chapter 2: Nanomagnetism

A brief overview of the origins of the field of spintronics is given, as viewed from the physics observed in magnetic materials, on the nanoscale. An overview is given of the discovery of the giant magnetoresistance (GMR) effect, and how this was instigated by the discovery of interlayer oscillatory exchange coupling. A review of spin transfer torque is also given, alongside details of the early discoveries of this effect in experimental systems. In addition, the exchange spring configuration that can arise in hard/soft component multilayers is outlined, and the physical mechanisms giving rise to the coupling observed in RFe_2 compounds is described. Finally, the magnetocrystalline anisotropy in these materials is described, together with the effects of strain, induced during crystal growth, on the overall magnetocrystalline anisotropy.

2.1: Giant Magnetoresistance and Spin Transfer Torque

Interest in magnetic nanostructures and their associated phenomena began in earnest in 1986, with the discovery of oscillatory interlayer exchange coupling in magnetic multilayers[1,2,3]. The magnetisations of two ferromagnetic layers separated by a non-magnetic (thin) spacer can become coupled through Ruderman-Kittel-Kasuya-Yoshida (RKKY) exchange mediated by the conduction electrons[17,18,19]. This effect was observed in the antiferromagnetically coupled Fe/Cr/Fe system by Grünberg *et al.*. This led directly to the discovery of the giant magnetoresistance (GMR) effect two years later, independently by Grünberg[4] and Fert's[5] groups. GMR has been one of the most important discoveries of the last 20 years, and has given rise to much research and applications for devices. Notably, read heads utilising GMR have revolutionised hard disk drive technologies. GMR is observed in multilayer devices as the change in resistance to current flow that occurs when the relative magnetisation orientation in two separate ferromagnetic layers changes. As an example, in Fe/Cr/Fe tri-layers the magnetisation in the two Fe layers is antiferromagnetically coupled, that is the magnetisations are constrained to align anti-parallel to each other. This results in a relatively large electrical resistance in the sample. On the application of an external magnetic field, the magnetisations can be brought into parallel alignment, causing the resistance of the sample to drop.

The concept of spin transfer torque, in which a spin polarised current flowing through a material can produce rotation of magnetisation within that material, has been around for a considerable amount of time. Berger predicted in 1978 that theoretically a spin polarised current should be able to produce domain wall motion within a sample[20]. His group then went on to show experimentally in subsequent years that this domain wall motion is possible in thin ferromagnetic films[21]. However, the currents required were very large, due to the samples being of the order of mm in size. As will be seen in the following discussion, it took a shift to the nanometre scale to generate interest in spin transfer research; when elements are of the order of nm then the currents required to switch them is typically of the order of mA. This is a much more practical current regime to operate in, and opens up possibilities for applications in devices such as magnetic storage media.

The modern field of spin transfer torque was launched in part by predictions by both Berger[22] and Slonczewski[23], independently, that a current applied perpendicular to the plane in a magnetic multilayer could generate sufficient spin transfer torque to switch the magnetisation of the soft layer. Spin transfer torque is phenomenologically closely related to giant magnetoresistance (GMR). In GMR the magnetisation of the sample produces a torque on the conduction electrons flowing through the sample; conversely, in spin transfer torque the conduction electrons produce a torque on the magnetisation. Both arise from an exchange interaction of the local magnetisation with the conduction electron spin.

In his theoretical work, Slonczewski described two potential different behaviours of a magnetic sample under the application of a DC current. Firstly, the sample can undergo a simple switching from one magnetic state to another. Alternatively the magnetisation could behave dynamically, entering a steady-state precession. This important initial work prompted much enthusiasm theoretically and experimentally. Spin transfer torque type excitations were first observed in magnetic multilayers by Tsoi *et al.*[24], two years after the initial predictions of Slonczewski and Berger. They utilised an experimental geometry consisting of a mechanical point contact to a metallic multilayer. Shortly afterwards results were published by Myers *et al*[25]. and Katine *et al.*[26] demonstrating magnetic reversal by spin transfer torque in lithographically patterned CPP multilayer pillars.

In magnetic spin electronic devices, the effectiveness of the device increases with increasing spin polarisation. This can be readily seen from the work of Slonczewski regarding excitation of spin waves in a typical spin valve structure[23,27], consisting of two magnetic layers separated by a non-magnetic spacer, shown schematically in figure 2.1. To determine the critical value of current required to excite spin waves in the free ferromagnetic layer F1, consider a first-order expression for the current-induced torque L_1 acting on the layer due to the current density j in the $+z$ direction

$$L_1 = \frac{\hbar \varepsilon j \theta}{2e} + \ldots , \qquad [2.1]$$

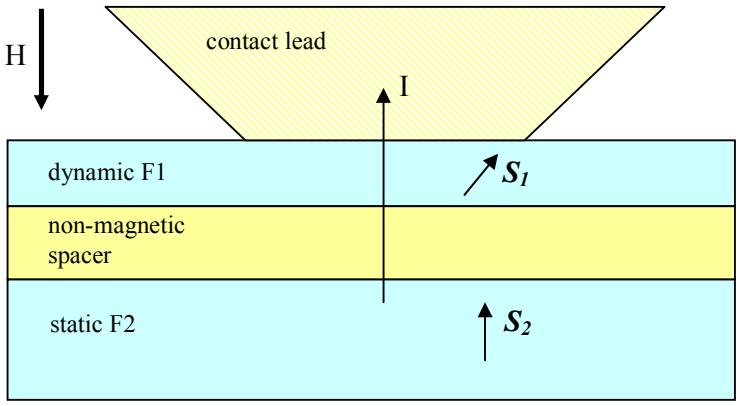

Figure 2.1: Schematic diagram showing an ideal contact to a metallic tri-layer comprising two ferromagnetic layers (F1 dynamic, F2 static) separated by a non-magnetic spacer layer. The applied field H is in the negative z direction, anti-parallel to the steady electric current I. S_1 and S_2 represent the macroscopic spin vectors in the associated ferromagnetic layers.

where θ is the angle subtended by the macroscopic spin vector $\boldsymbol{S_1}$ in layer F1 on the z axis. The dimensionless efficiency, ε, for conversion of current to spin torque appears in this expression and is an effective way to consider the efficiency of a given device with regards to spin torque effects. The efficiency can be written[23]

$$\varepsilon = [-4 + \frac{(1+P)^3(3+\hat{\mathbf{s}}_1 \cdot \hat{\mathbf{s}}_2)}{4P^{3/2}}]^{-1}, \text{ where } P = \frac{N_\uparrow(E_F) - N_\downarrow(E_F)}{N_\uparrow(E_F) + N_\downarrow(E_F)}, \qquad [2.2]$$

and where the macroscopic unit spin vectors $\hat{\mathbf{s}}_\mathbf{i} = \mathbf{S_i} / S_i$. For two ferromagnetic layers of like composition ($\hat{\mathbf{s}}_1 = \hat{\mathbf{s}}_2$) this expression can be simplified to

$$\varepsilon = 2[(P^{1/2} + P^{-1/2})^3 - 4]^{-1}. \qquad [2.3]$$

This model assumes a ballistic free-electron-like spin transport within the layered magnet, with the layer thicknesses smaller than the mean free path of electrons in the material, and is calculated within the Wentzel-Kramers-Brillouin (WKB)

approximation. The Fermi level polarisation factor P is that described in equation 3.15 with $n = 0$; it is only based on the difference in density of states for two spin channels at the Fermi energy, and includes no weighting by the Fermi velocity. However, this equation highlights that the efficiency of spin torque is highly dependent on the spin polarisation of the materials within a device.

2.2: Exchange Spring Magnetism

Exchange spring systems have received much attention in recent years. Exchange coupled superlattices comprising hard and soft composite layers were studied by Skomski and Coey[6,7], with a view to improving the maximum energy product $(BH)_{max}$ for permanent magnet applications. They derived the theoretical limit of the energy product as

$$(BH)_{\max} = \frac{1}{4}\mu_0 M_s^2 \left(1 - \frac{\mu_0 (M_s - M_h) M_s}{2K_h}\right) \qquad [2.4]$$

where M_s is the saturation magnetisation of the soft layer, M_h is the saturation magnetisation of the hard layer and K_h is the anisotropy constant for the hard layer, assuming zero anisotropy in the soft layer ($K_s = 0$). Using a different theoretical approach they derived the maximum energy product for multilayer systems which is slightly lower than that obtainable from the optimal hard/soft composition where the nucleation field is half the remanence. Inserting values for $Sm_2Fe_{17}N_3$ / FeCo multilayers gives a theoretical maximum energy product $(BH)_{max}$ of 1 MJ/m^3, over twice that obtainable in $Nd_2Fe_{14}B$ magnets[28].

Exchange spring systems are characterised by a hard-soft magnetic composite configuration, where typically the spring is set up in the soft layer(s). The hard layer provides a large anisotropy and large coercive field to the system, while the soft layer provides enhanced magnetic moment. Within the soft layer, the atomic layers near to the adjacent hard layers are pinned via the exchange interaction, while the center of the layer is free to align with an applied magnetic field. Thus, under the application of

an external magnetic field, a 'spring-like' structure of canted magnetic moments can be set up within the soft layer, where the center rotates but the edges are pinned to the same magnetisation direction as the hard layer.

Fullerton *et al.* studied SmCo/TM (TM = Fe, Co) bilayer systems, with ferromagnetic exchange coupling between the hard and soft layers[29]. The large in-plane anisotropy field afforded by the SmCo (up to 20T) allowed study of bilayers with a soft TM layer of <20nm. They concluded that exchange coupling does not depend strongly on the crystalline matrix matching at the hard-soft interface, as was previously thought[30], because Fe and Co have different crystalline symmetries but were found to both couple strongly to the hard SmCo layer.

Victora *et al.* propose that a hard-soft composite system could be used for applications in data storage. The main block to continued miniaturisation and increased areal density in data storage media is that of the superparamagnetic effect. The barrier to random thermal switching of data storage elements is proportional to the product of the anisotropy of the material and the volume of the element. Therefore, if the volume of elements decreases sufficiently, the storage medium is no longer stable and data loss will occur. High anisotropy materials can be used to counter this effect, but this has the disadvantage of increasing the write field required. Victora *et al.* propose the use of hard-soft composite elements, which can benefit from the high anisotropy afforded by the magnetically hard component, while taking advantage of the low coercive field of the soft component.

Recently a $DyFe_2/YFe_2/DyFe_2$ tri-layer exchange spring cylindrical nanopillar system has been studied computationally under the application of an electric current by Franchin *et al.*[31], using a finite element micromagnetic model. They found that current excitation produced a precession of the magnetisation in the soft YFe_2 layer around the axis of the cylinder, and also a compression of the exchange spring in the direction of electron flow. This can be explained through current induced domain wall motion, with the exchange spring acting as an artifical domain wall.

2.3: Magnetism of RFe_2 Laves Phase Intermetallics

The RFe_2 Laves phase intermetallics, where R is a heavy rare earth (eg. Dy, Tb, Er), display both strong Fe-Fe exchange and also strong anti-ferromagnetic R-Fe exchange. The Fe-Fe exchange interaction is very strong, up to 1000K in pure samples of Fe, and typically around 600K in the RFe_2 intermetallics, and the interaction is also long range. Heisenberg-like direct exchange is not responsible for the inter-atomic Fe-Fe exchange coupling. The 3*d* electrons, responsible for magnetism in Fe, have highly localised wavefunctions, extending over only roughly half of the inter-atomic distance[32]. Indeed, the experimentally measured Curie temperature T_C is much larger than that implied from calculations of direct exchange in Fe, demonstrating that direct exchange cannot be responsible for the strong Fe-Fe interactions[33].

It is known that 3d electrons are partially hybridized with the conduction bands. In 1951, Zener proposed a model of Fe-Fe exchange in which the 3*d* electrons polarise the conduction electrons, which then in turn align the localised moments on neighbouring atoms in the lattice, due to their extended wavefunctions[34,35]. This theory therefore contains both direct exchange between the 3*d* and conduction electrons and ultimately an indirect exchange between localised *d* electrons. This theory of indirect exchange mediated by conduction electrons was further developed independently by Ruderman and Kittel[17] and also by Kasuya[18] and Yosida[19], referred to as the RKKY model, initially developed to explain the hyperfine interaction between nuclei and the conduction electrons. This theory can also be applied to the closely related problem of the indirect exchange coupling of the core electron spins with the conduction electrons. The interaction between localised electron spins and the conduction electrons results in an oscillatory indirect exchange coupling, which varies in sign dependent on the distance between atomic sites in the crystal lattice. Therefore, the RKKY interaction can give rise to both ferromagnetic and anti-ferromagnetic coupling, dependent on the distance between interacting atoms.

The RKKY function is plotted in figure 2.2, showing clearing the crossover between the two coupling regimes as a function of distance from a site in the lattice. For many years this was accepted as the mechanism for Fe-Fe indirect exchange,

however, Stearns demonstrated that this is not possible. Through NMR and Mössbauer measurements she showed that the conduction electron spin is in fact negative, out to two nearest-neighbours from the central atom[36,37,38,39]. As the conduction electrons have the opposite spin to the localised electrons on the neighbouring sites, the interaction will give rise to anti-ferromagnetic coupling. Therefore, indirect exchange through coupling of localised *d* electrons to the itinerant *s* electrons cannot account for the strong ferromagnetic exchange in Fe.

Stearns proposed an alternative explanation for the strong Fe-Fe exchange, suggesting that the mediating factor in the indirect exchange interaction is in fact itinerant *d* electrons, produced through *s*-*d* band mixing[40]. These should give rise to longer range interactions than for the *s* conduction electrons, potentially allowing nearest-neighbours to sit inside the first crossover in the RKKY function, resulting in a positive exchange and ferromagnetic coupling (See figure 2.2). Stearns argued, using the calculated band structure for Fe, that 5-8% of the *d* electrons are sufficiently itinerant to mediate interatomic exchange by a RKKY type interaction. The mechanism behind the strong, long range exchange in Fe is still very much an open question.

The coupling of R-TM moments depends on the position occupied by the rare earth in the series. For the light rare-earths (e.g. Nd, Pr) the total moment $J = L - S$, the spin moment and the total moment are anti-parallel. In the heavy rare-earths (e.g. Dy, Er), $J = L + S$, and the total moment and spin moment are parallel. With the exception of Gd, $L \geq S$ for the rare-earth species. Therefore, the effective moment, proportional to J, is reduced for light rare earths and increased for heavy rare earths. The spin-spin coupling in R-TM intermetallics is always antiferromagnetic. Ferromagnetic coupling is observed of transition metal moments with light rare-earth moments ($\boldsymbol{J.S} > 0$), and antiferromagnetic coupling for heavy rare-earths ($\boldsymbol{J.S} < 0$). This is illustrated schematically in figure 2.3.

It is tempting to try to explain R-TM coupling through the antiferromagnetic conduction electron mediated RKKY exchange interaction. However, as variations in R-TM separation do not change the sign of the coupling, as evidenced by the common

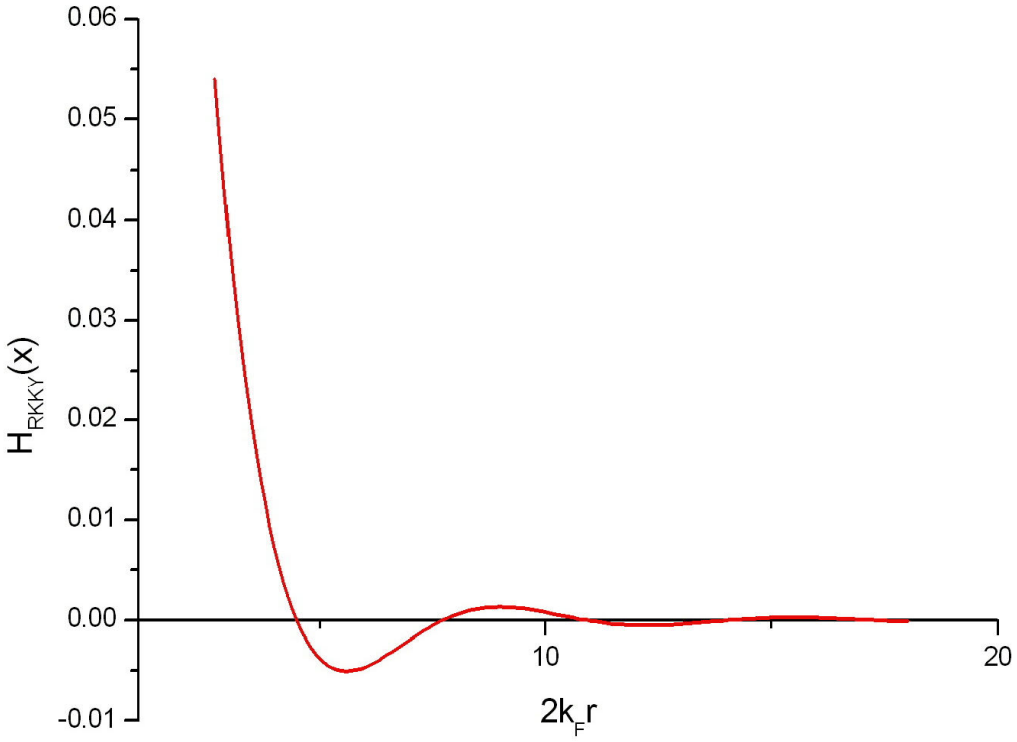

Figure 2.2: Spatial variation of the RKKY exchange Hamiltonian. The sign of the exchange interaction can be positive or negative, dependent on the inter-atomic distance within the lattice.

ferromagnetic/antiferromagnetic coupling shared by all light/heavy rare earth based compounds, use of the RKKY model is questionable. Campbell offers an alternativemechanism, focussing on the 5*d* conduction electrons in the rare earth, which are spin parallel to the 4*f* electrons[41]. He proposed the creation of a moment on the 5*d* electrons through exchange with the 4*f* electrons, and then direct *d*-*d* exchange with the ferromagnetic elements in the compound, as well as with other rare earth sites. As the magnetic transition metals are at the opposite end of the transition series from the rare earths, their 3*d* spin moments will tend to couple antiferromagnetically to the moments on the rare earth site. Therefore, this proposed mechanism can account for the antiferromagnetic spin-spin coupling that is always observed inR-TM compounds, and consequently the ferromagnetic/antiferromagnetic coupling observed with light/heavy rare earth species.

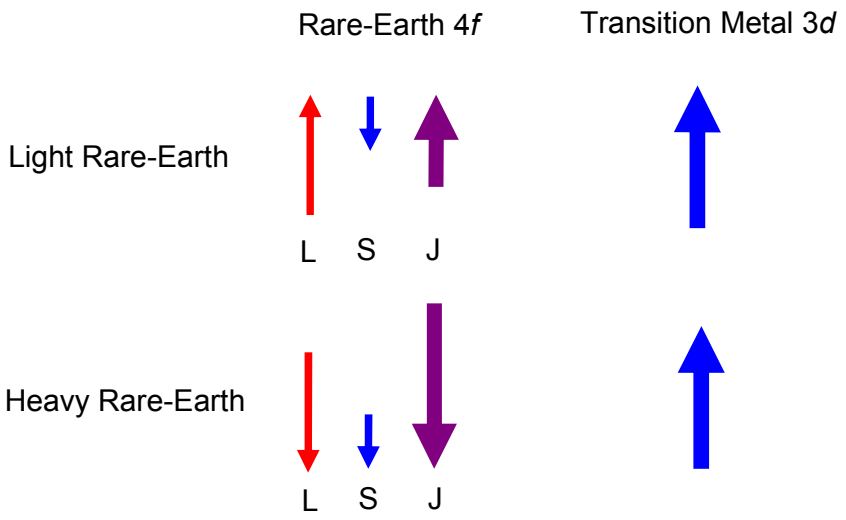

Figure 2.3: Diagram illustrating the coupling between moments in R-TM intermetallics, for both light and heavy rare-earth species. L and S are anti-parallel (parallel) in light (heavy) species, resulting in an overall reduction (increase) in the moment. R-TM coupling is ferromagnetic (antiferromagnetic) for light (heavy) R species.

The R-TM compounds with a heavy rare earth element have a high degree of magnetic anisotropy, the strength and directionality of which is determined by the rare earth magneto-crystalline anisotropy. The easy axis in bulk $DyFe_2$ is along the [001] direction, whereas in $ErFe_2$ the easy axes lie along the <111> body diagonals. Anisotropy in the rare earth compounds is traditionally described by the Callen-Callen model, which has been very successful in describing these compounds[42]. The magnetic free energy of a cubic crystal can be expanded in terms of the directional cosines (α_1 α_2, α_3) along the axes of the magnetisation **M**

$$E(\mathbf{M},T) = K_0 + K_1(\alpha_1^2\alpha_2^2 + \alpha_2^2\alpha_3^2 + \alpha_3^2\alpha_1^2) + K_2(\alpha_1^2\alpha_2^2\alpha_3^2)\,. \qquad [2.5]$$

This model, which contains the anisotropy constants K_1 and K_2, allows for easy axis directions along the major cubic symmetry axes only ([001], [101] and [111]) upon minimisation of the free energy.

However, in certain rare earth compounds such as $CeFe_2$, $SmFe_2$, $HoFe_2$ and the ternary compound $Ho_{0.6}Tb_{0.4}Fe_2$ it was found that the easy axis lies in a non-major cubic symmetry axis, which cannot be explained using the Callen-Callen model[43,44]. Atzmony and Dariel showed that by introducing a third, 8th power anisotropy constant K_3 that this behaviour can be explained satisfactorily[45]

$$E(\mathbf{n},T) = K_0 + K_1(...) + K_2(...) + K_3(\alpha_1^4\alpha_2^4 + \alpha_2^4\alpha_3^4 + \alpha_3^4\alpha_1^4)\,. \qquad [2.6]$$

They also found other unusual behaviour, deducing that there should be a change of sign in the anisotropy constants K_1 or K_2 for $HoFe_2$ and $DyFe_2$, respectively, as the temperature is varied. This change of sign occurs rapidly at 30K and 70K, respectively. This behaviour has recently been explained by Martin *et al.*, through extending the Callen-Callen model with second order perturbation theory[46]. They are also able to explain the origin and behaviour of the phenomenological K_3 term introduced by Atzmony and Dariel previously. In addition, they found that the 10th order K_4 term dominates over K_3 at low temperatures.

The magnetic behaviour of MBE-deposited films of R-TM compounds, in particular $DyFe_2$ and $ErFe_2$ which are studied in this thesis, can vary significantly from the bulk. In particular, strain induced through MBE deposition results in a modification of the bulk magnetic easy axes in the film. Typically, strain in epitaxial thin films arises as a result of misfit of the lattice parameters of the buffer and the deposited layer. However, in RFe_2 films deposited on a NbFe buffer, the observed strain is much lower than that which would be expected from mismatch alone[47]. Also, the strain parameters have the opposite sign to that expected from lattice mismatch; as the Laves phase parameters are larger than the buffer, there should be an in-plane reduction and an out of plane expansion of the lattice parameters, but experimentally the opposite is observed. Mougin *et al.* proposed that the strain in MBE-grown RFe_2 is in fact due to cooling after deposition has taken place[48]. The deposited layer and the buffer have different coefficients of thermal expansion, and therefore experience different rates of contraction, inducing strain in the deposited film.

The change in the strain term is much less temperature dependent than the magnetocrystalline anisotropy, resulting in some cases in a temperature dependence of the easy axis. In MBE-grown $DyFe_2$, the easy axis is found to be [001] at low temperatures (the bulk easy axis). As the temperature is increased, the axis rotates to point along the $[1\,\bar{1}\,0]$ direction, as the contribution from strain increases. In $ErFe_2$ the strain moves the easy axis from the bulk orientation to the out of plane [111] axis. At higher temperatures the strain dominates, and the easy axis lies along the growth direction [110].

Chapter 3: Point Contact Andreev Reflection

A review of early point contact spectroscopy experiments is given, followed by a description of point contact regimes and the determination of point contact resistance. The spin polarisation of a material can be defined in a number of ways, dependent on the experimental geometry used, and these are summarised in this chapter. The physics behind Andreev reflection and application of this theory to a point contact geometry are detailed, followed by modifications that may be made to the model to account for spin-dependent transport. This allows the spin polarisation in a material to be determined using point contact Andreev reflection (PCAR), and the theory described here is applied throughout the experimental chapters to determine the spin polarisation in a range of materials (Chapters 5-7). Finally, a review is given of recent research using the PCAR technique, and discoveries that can be applied to the PCAR experiments presented in this thesis.

3.1: Point Contact Theory

Point contact spectroscopy has been in use for many years, since the pioneering experiments of Yanson in 1974, who studied tunnel junctions with a short circuit in the tunnel layer[49]. He observed non-linearity of current-voltage characteristics of these contacts at liquid helium temperatures, and characterised this behaviour by measuring the second voltage derivative with respect to current d^2V/dI^2 as a function of the applied voltage V. He observed structure in these characteristics at voltages corresponding to the bulk phonon frequencies in the metal forming the contact, and therefore deduced that the technique was a direct measurement of the electron-phonon interaction within the contact. Point contact spectroscopy has since been extensively used for the study of the electron-phonon interaction and the associated Eliashberg function α^2F, where F is the phonon density of states and α is the matrix element for the average electron-phonon interaction over the Fermi sphere.

This interaction can be understood by considering the nature of electron transport through the contact. If the contact radius is small when compared to the mean free path of electrons in the contact metal, as is typically the case in point contact spectroscopy, then the electrons will be accelerated within a mean free path distance across the contact by the electric field due to the applied voltage ie ballistic transport. These accelerated electrons are then brought back to equilibrium through inelastic scattering with phonons within the metal. Thus immediately it can be seen that the voltage-dependent behaviour of the electrons within the contact will reveal the nature of the electron-phonon interaction within the contact. Scattering at specific energies results in a sudden increase in resistance, corresponding to a sharp peak in the d^2V/dI^2 spectra, and these peaks can then be matched to the phonon spectra of the contact metal.

In early experiments, Yanson studied homo-junctions of metals (Pb, Sn, In, Cu, Ag, Al) formed by producing a short in an oxide layer between two identical metal layers[49]. This was achieved by introducing adenine into the barrier during oxidation to provide small electrical shorts. Jansen *et al.* used point contact spectroscopy to study hetero- and homo-junctions of noble metals (Cu, Ag, Au), comparing the spectra with

$F(\omega)$ taken from neutron scattering experiments[50]. However, for these measurements they used a new technique for the formation of the point contact junction – an electrolytically etched wire with a point ~0.5μm in diameter was used to form a contact with a metal film, by pressing the point carefully into the film. This method has the advantage of allowing relatively quick and easy measurements of a wide range of materials, without time-consuming fabrication steps. They then extended the technique to measurement of the alkali metals (K, Na, Li), using a sealed container to prevent exposure of the metal to air, keeping the sample in an inert He atmosphere[51].

The resistance of a small point contact in the diffusive regime was initially treated by Maxwell over 100 years ago[52]. The current flowing through a circular contact of radius a produces contours of potential energy, described by

$$\phi(\boldsymbol{r}) = \pm\frac{1}{2}eV[1-(2/\pi)\tan^{-1}(1/\xi)] \qquad [3.1]$$

in oblate spherical coordinates, obtained using the equation $r^2/a^2 = (1+\xi^2)(1-z^2/\xi^2a^2)$ which contains r and z from classical spherical coordinates. Surfaces of constant ξ form oblate spheroids centred on the contact. To obtain the contact resistance we take the total voltage V across the contact and divide by the current through any contour of constant potential from equation 3.1. Taking ξ = 0, the centre of the contact, equation 3.1 gives $\phi(\boldsymbol{r})$ = 0. The total current through the contact is given by

$$I = \int d\boldsymbol{A}\,.\,\boldsymbol{j} = \int_0^{2\pi} d\varphi \int_0^a r dr \frac{1}{\rho e}\left(\frac{\partial\phi}{\partial z}\right)_{z=0} \qquad [3.2]$$

where $\boldsymbol{A}$ is the area of the contact and $\boldsymbol{j}$ is the current density, taken from Ohm's law in the form $j_z = \sigma E_z = (1/\rho e)(\partial\phi/\partial z)$, where σ and ρ are the conductivity and resistivity, respectively. Performing the integral gives an expression for the resistance of the point contact

$$R_M = \frac{\rho}{2a} \qquad [3.3]$$

known as the Maxwell resistance. This solution only holds while transport across the contact is still diffusive, and is described well by Ohm's law. If the contact diameter becomes comparable to the mean free path of electrons in the contact material l then it becomes difficult to fully describe the nature of the contact using the Maxwell method, as transport across the contact becomes more ballistic in nature. The intersection of the two regimes is described by the Knudsen ratio $K = l/a$ after Knudsen, who first considered the problem of crossover between diffusive and ballistic gas flow through constrictions[53], which can be considered a parallel case.

We now consider the opposite limit to that of Maxwell, in which the Knudsen ratio is very large, i.e. $l >> a$. Transport across the contact in this limit is due to acceleration of conduction electrons by the applied voltage, due to the large potential gradient near the contact. Electron flow is wholly ballistic within a sphere of radius approximately equal to the mean free path. This limit was first considered by Sharvin, who proposed a method of studying the Fermi surfaces of metal samples using microcontacts to the sample surface[54]. These microcontacts were of a small radius a, which is significantly smaller than the mean free path of electrons in the metal, and therefore the resistance will depend entirely on the acceleration of electrons near the contact, independent of the mean free path. The speed increment Δv of electrons flowing in either direction through the contact due to the voltage V is $\pm eV/p_F$, where p_F is the Fermi momentum. This speed increment results in a total current through the (assumed circular) contact of

$$I = \pi a^2 eN\Delta v = \pi a^2 N\left(\frac{e^2 V}{p_F}\right), \qquad [3.4]$$

where N is the electron density, giving a contact resistance of

$$R = \frac{p_F}{\pi e^2 a^2 N}. \qquad [3.5]$$

Following the method of Jansen *et al.*[55], substitution of the Drude resistivity formula $\rho = p_F / Ne^2 l$ and integrating over all possible angles gives

$$R = \frac{4\rho l}{3\pi a^2}. \qquad [3.6]$$

The resistance of the contact is independent of the mean free path ($\rho \propto l^{-1}$), as is characteristic of ballistic transport across the junction.

Between the two limits in which the Knudsen ratio is very large or close to zero, the Sharvin and Maxwell limits, an interpolation can be arrived at for determination of the resistance for any given Knudsen ratio. Wexler studied the problem of this intermediate regime[56], and through solving the Boltzmann equation using the variational principle for the resistance of the contact, arrived at

$$R = \frac{\gamma(K)}{2\sigma a} + \frac{4K}{3\pi\sigma a} = \frac{\gamma(K)\rho}{2a} + \frac{4\rho l}{3\pi a^2} \qquad [3.7]$$

Where $\gamma(K)$ is a slow varying function of $K = l/a$ with the limits 1 when K=0 and 0.694 when K = infinity. The function is plotted in figure 3.1, showing the variation from low to high K.

We again follow the methodology of Jansen *et al.* in order to demonstrate the dependence of the second voltage derivative on the electron-phonon interaction, as stated earlier. The second derivative d^2V/dI^2 is proportional to the first voltage derivative of resistance dR/dV, and therefore the energy dependence of equation 3.7 must be considered,

$$\frac{dR}{dV} = \frac{\gamma(K)\rho l}{2a}\frac{d}{dV}\left(\frac{1}{l(\varepsilon = eV)}\right). \qquad [3.8]$$

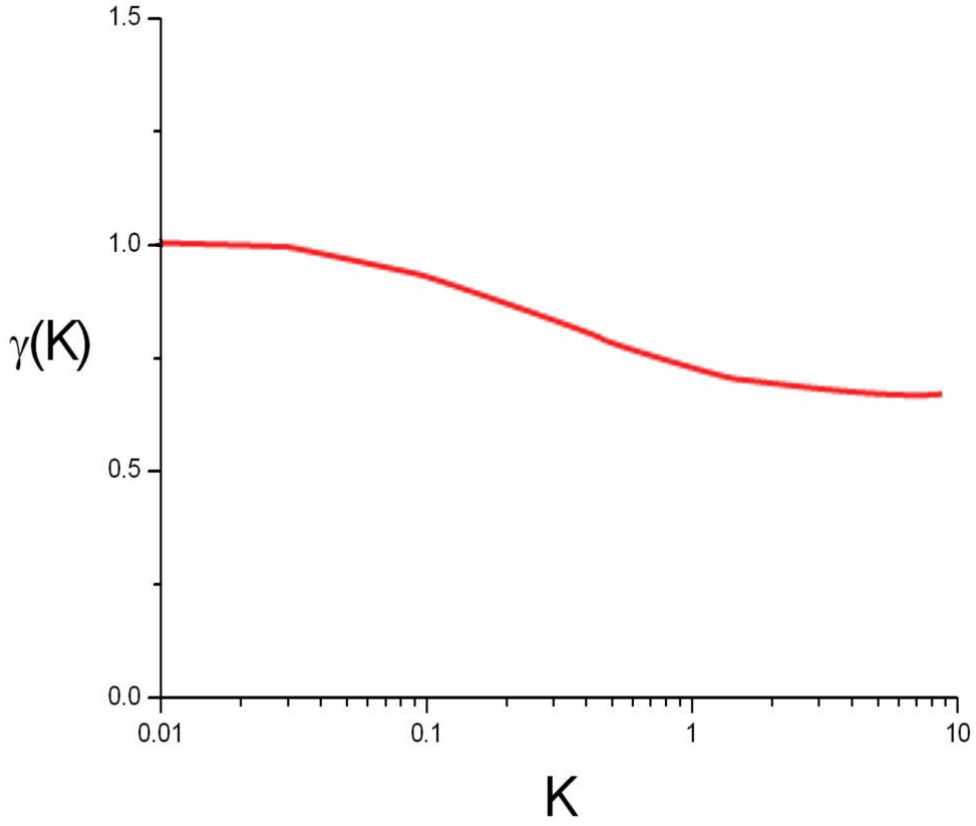

Figure 3.1: Variation of the interpolation γ(K) from equation 3.7 as a function of K.

The second term in equation 3.7 therefore results in no structure, which is to be expected as this term represents ballistic transport of electrons with no scattering – it does, however, allow an electric field to exist within the metal, essential for electron-phonon interaction. The total mean free path arises from two contributions, those due to impurity scattering (elastic) and phonon scattering (inelastic) – we consider only phonon scattering, as impurity scattering is energy independent, giving rise to no features in a voltage spectra. Applying Fermi's golden rule[57], the scattering time of an electron at an energy ε above the Fermi level is

$$\tau^{-1} = \frac{2\pi}{\hbar}\sum_{k}\left|g_q\right|^2 \delta(\varepsilon_p - \varepsilon_k - \hbar\omega_q)(N_q + 1 - f_k) + \delta(\varepsilon_p + \hbar\omega_q - \varepsilon_k)(N_q + f_k) \quad [3.9]$$

Where g_q is the electron-phonon interaction matrix element for a phonon of wavevector q and energy $\hbar\omega_q$, N_q the Bose distribution function for the phonons, ε_p

and ε_k the energies of electrons with momenta p and k respectively, and f_k is the Fermi distribution function of the electrons evaluated at the energy ε_k. The Eliashberg function can be defined as

$$\alpha^2 F(\omega) = \frac{N_0}{2} \int \frac{qdq}{2k_F{}^2} \left| g_q \right|^2 \delta(\hbar\omega - \hbar\omega_q) \qquad [3.10]$$

where N_0 is the density of states at the Fermi level. Converting the summation over k in equation 3.9 to an integral and substituting equation 3.10 gives, for zero temperature

$$\tau(\varepsilon)^{-1} = 2\pi \int_0^{e/\hbar} d\omega \alpha^2 F(\omega) \,. \qquad [3.11]$$

Substituting this result into equation 3.8 by writing $\tau(\varepsilon) = l(\varepsilon) / v_F$ gives, at low temperatures where the approximation holds,

$$R\frac{d^2V}{dI^2} = \frac{dR}{dV}(V) = \frac{\gamma(K)\rho l}{2a} \frac{2\pi e}{\hbar v_F} \alpha^2 F(eV) \,, \qquad [3.12]$$

demonstrating that, as previously stated, by measuring the second derivative of voltage as a function of voltage a signal proportional to the electron-phonon interaction is recorded.

3.2: Point Contact Andreev Reflection

Andreev reflection, discovered by Alexander F. Andreev in 1964, is an effect observed at the interface between a normal metal and a superconductor[58]. Consider an interface of this type – any electron incident on the interface from the normal metal must be a member of a pair in order to propagate into the superconductor, as the electrons in the superconductor form a Bose-Einstein condensate. The electron required to allow this supercurrent conversion to occur is taken from the normal metal.

This results in the creation of a hole which propagates away from the interface. These holes form a parallel conduction channel to that of the electrons, resulting in a doubling of the normal state conductance dI/dV for voltages $eV < \Delta$ where Δ is the superconducting gap at the interface. If the voltage and hence the incident energy of electrons at the interface is pushed above this value then superconductivity at the interface breaks down and normal conductance is observed.

Figure 3.2 illustrates this effect through a simple band structure comparison of the two materials. Note this is for the case of a completely non-spin polarised normal metal (P=0% where P is the spin polarisation). Figure 3.3 illustrates the case of a completely spin polarised material (P=100%). As a superconducting pair is composed of a spin-up and a spin-down electron, an incident spin-up electron requires an electron from the spin-down band for supercurrent conversion to take place. This results in the creation of a spin-up hole, which is considered to be in the spin-down density of states as it results from the removal of an electron from this sub-band. If, as in the case of a spin polarised material, there is a deficit in the population of one spin sub-band, then the process of supercurrent conversion will be suppressed, manifesting in a reduction in the increase in differential conductance for voltages below Δ. If the spin polarisation is sufficiently high then the differential conductance is in fact reduced, as conversion of single electrons to pairs becomes more difficult due to the reduced population of the minority spin band which provides the other member of the superconducting pair.

The spin polarisation of a material can be defined in a number of ways, each based of different parameters. In tunnelling experiments, which can also be used to measure spin polarisation, the parameter that best defines the measured result is a tunnelling polarisation. In point contact measurements such as those described in this thesis, the polarisation can be most accurately described using the Fermi velocity[59]

$$P_C = \frac{N_\uparrow(E_F)v_{F\uparrow} - N_\downarrow(E_F)v_{F\downarrow}}{N_\uparrow(E_F)v_{F\uparrow} + N_\downarrow(E_F)v_{F\downarrow}} \qquad [3.13]$$

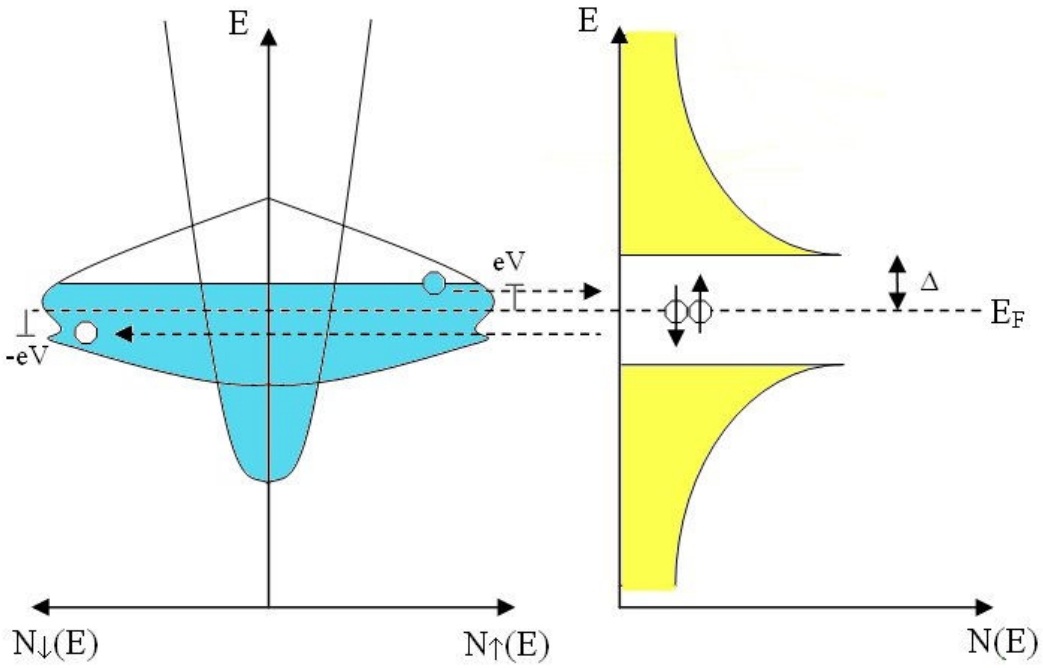

Figure 3.2: Schematic density of states as a function of energy for an ideal metal with zero spin polarisation. A full unsuppressed Andreev reflection process is possible due to the availability of states in both spin sub-bands at the Fermi energy E_F.

where $v_{F\sigma}$ is the Fermi velocity of electrons and $N_\sigma(E_F)$ is the density of states at the Fermi level in the respective spin sub-bands σ. If one notes that $I \propto N(E_F)v_F$ in the ballistic regime, where I is the current in a specific spin channel then equation 3.13 may be re-written as

$$P_C = \frac{I_\uparrow - I_\downarrow}{I_\uparrow + I_\downarrow} \qquad [3.14]$$

A more general expression for the spin polarisation of a material can be written, describing three different types of spin polarisation[60]

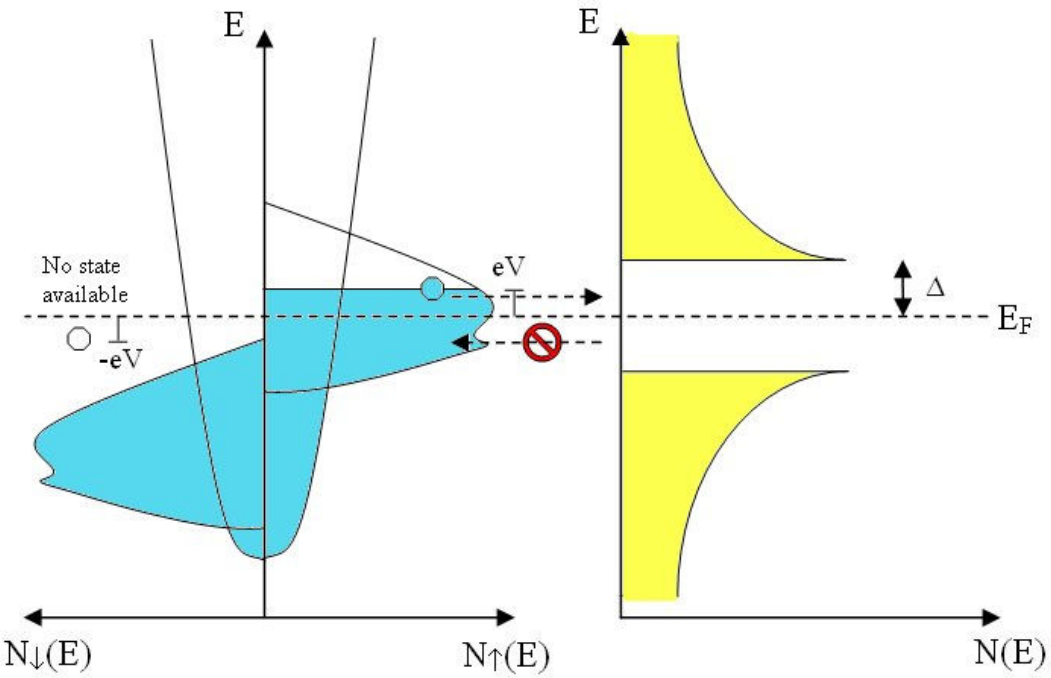

Figure 3.3: Schematic density of states for an ideal half-metal, with 100% spin polarisation. Andreev reflection is a forbidden process due to a lack of states in the minority spin-sub band at the Fermi energy.

$$P_n = \frac{\left\langle N_\uparrow(E_F) v_{F\uparrow}^n \right\rangle - \left\langle N_\downarrow(E_F) v_{F\downarrow}^n \right\rangle}{\left\langle N_\uparrow(E_F) v_{F\uparrow}^n \right\rangle + \left\langle N_\downarrow(E_F) v_{F\downarrow}^n \right\rangle}, \qquad [3.15]$$

where $n = 0, 1, 2$ signifies the regime in which the spin polarisation is considered. P_0 is the polarisation determined only by the DOS imbalance at the Fermi level, and is typically measured in, for example, spin-resolved photoemission. For transport measurements the Fermi velocity plays a role, in the ballistic regime (n=1), where the Knudsen ratio K is large, the polarisation is weighted by v_F, as can be seen in equation

3.15. $n = 2$ signifies the diffusive regime, where K is close to zero, and the weighting of P_2 is quadratic in v_F. It is possible to extend this formalism to include the polarisation typically measured in tunnelling experiments, P_T, by replacing the Fermi

velocity with spin-dependent tunnelling matrix elements in the $n = 2$ regime. It can be shown that for a tunnel barrier with a low transparency, P_T reduces to P_2[61].

A theoretical framework for the analysis of Andreev reflection in spin-polarised materials has been developed by R J. Soulen Jr. *et al.*[62], based on the Blonder-Tinkham-Klapwijk (BTK) theory of conventional Andreev reflection in non-spin polarised materials[63]. Interfacial scattering may be included into the BTK model via the Z parameter, which is governed by the ratio of a scattering potential to the Fermi velocity $Z = H / \hbar v_F$ where H is the repulsive scattering potential. Note that as $H \rightarrow \infty$, Z becomes infinite, and this extreme represents the tunnelling case. A truly ballistic point contact with zero scattering has $Z = 0$, the other extreme. For the purposes of the spectra presented in this thesis we shall assume Z is small and the contact is essentially ballistic in character.

The current flow through the contact can be decomposed into spin polarised and non-polarised components

$$I = I_{\uparrow} + I_{\downarrow} = 2I_{\downarrow} + (I_{\uparrow} - I_{\downarrow}) = I_{unpol} + I_{pol} \qquad [3.16]$$

The unpolarised current I_{unpol} carries no net spin polarization and obeys conventional BTK theory. The polarized remainder I_{pol} carries all of the spin polarization P_C and is therefore an entirely quasiparticle current (supercurrent can carry no net spin polarization, being comprised of pairs of spin up/spin down electrons).

Typically in PCAR the data obtained will be dI/dV differential conductance curves. In order to extract P_C from these curves it can be noted that

$$\frac{dI}{dV} = (1 - P_C)\frac{d}{dV} I_{unpol} + P_C \frac{d}{dV} I_{pol} \ . \qquad [3.17]$$

Assuming $Z \approx 0$ then for $eV << \Delta$ and $k_B T << \Delta$,

$$\frac{d}{dV} I_{unpol} = 2G_n \quad \text{and} \quad \frac{d}{dV} I_{pol} = 0 , \qquad [3.18]$$

giving

$$\frac{1}{G_n} \frac{dI}{dV} = 2(1 - P_C) . \qquad [3.19]$$

Where G_n is the normal state conductance of the point contact. This simple result provides an easy method for determination of the spin polarisation from the conductance curve of a superconductor–ferromagnet (SC-FM) point contact. However, we have assumed $Z = 0$, which will generally not be the case for real point contact junctions, where interface effects and the size of the contact will result in a non-zero and potentially large Z. Also we have neglected temperature effects, which will act to broaden the PCAR spectrum.

For accurate determination of P_C for arbitrary Z we must fit to the full Blonder-Tinkham-Klapwijk (BTK) model of Andreev reflection in small SC-metal contacts[4]. The BTK model is a generalised 'semiconductor model' in which the Bogoliubov equations are considered, matching wavefunctions at the boundary. In this manner it is possible to consider all situations from a clean metallic contact to a tunnelling regime using the same formalism. Through these equations the probability current of the various excitations may be determined. The analysis is restricted to clean metals in which momentum may be considered a good quantum number.

For energies $E > \Delta$, the conventional Bardeen, Cooper and Schrieffer (BCS) quasiparticle excitations of energy

$$E_k = (\Delta^2 + \varepsilon_k{}^2)^{1/2}, \qquad \text{where} \qquad \varepsilon_k = \frac{\hbar^2 k^2}{2m} - \varepsilon_F , \qquad [3.20]$$

may be identified with the incident, transmitted and reflected particles. As the square of ε_k enters the expression there is a pair of k associated with each energy, $\hbar k^{\pm}$. Because of BCS pairing of $-k$ and k this results in a fourfold degeneracy of states.

Twofold spin degeneracy is neglected in the original BTK model, and is included in later authors modifications of the model to describe ferromagnetic materials, as will be described later. The nature of these quasiparticle excitations is given by a Bogoliubov transformation

$$\gamma_{k0}^{*} = u_k c_{k\uparrow}^{*} - v_k c_{-k\downarrow} \qquad [3.21]$$

Equation 3.21 describes electron creation at $+k$ ($u_k c_{k\uparrow}^{*}$) and hole creation at $-k$ ($v_k c_{-k\downarrow}$) and may be described as a two element column vector

$$\varphi_{k0} = \begin{pmatrix} f_k(x,t) \\ g_k(x,t) \end{pmatrix} \qquad [3.22]$$

And in a time independent regime, may be replaced with stationary states of energy E. It is convenient to introduce operators of the form

$$\begin{aligned} \gamma_{ek0}^{*} &= u_k c_{k\uparrow}^{*} - v_k S^{*} c_{-k\downarrow} \\ \gamma_{hk0}^{*} &= u_k S c_{k\uparrow}^{*} - v_k c_{-k\downarrow} = S\gamma_{ek0}^{*} \end{aligned} \qquad [3.23]$$

where S^* adds a pair to the condensate and S destroys one. These operators create excitations and change the charge by $\pm e$. For a system with fermionic excitations of this type, the total energy may be written

$$E = E_G + \sum_k E_k \gamma_k^{*} \gamma_k + \mu N \qquad [3.24]$$

Where N is the number of electrons in the system and E_G is the ground state energy. Table 3.1 summarises the possible charge-conserving processes involving two subsystems with their corresponding energy conditions. All these transitions are 'horizontal' if quasiparticle branches in the lower half plane are included, as in the right hand side of figure 3.4.

Process	Energy condition
Electron from system 1 to 2 / 2 to 1	$\mu_1 + E_{k1} = \mu_2 + E_{k2}$
Hole from system 1 to 2 / 2 to 1	$\mu_1 - E_{k1} = \mu_2 - E_{k2}$
Create electron in 1 and hole in 2 / destroy both	$\mu_1 + E_{k1} = \mu_2 - E_{k2}$
Create hole in 1 and electron in 2 / destroy both	$\mu_1 - E_{k1} = \mu_2 + E_{k2}$

Table 3.1: Summary of processes involving transfer of unit electronic charge across two fermionic subsystems (From Blonder et al. 1982).

Figure 3.4 shows the boundary between a normal metal and a superconductor. Relevant quasiparticle states are labelled 0-5, with the hole state at $-E$ labelled 6. Four processes can be identified across the barrier, with probabilities A(E), B(E), C(E) and D(E) as labelled on the figure. C(E) and D(E) are electron transmission probabilities with a wavevector on the same side of the Fermi surface and opposite side, respectively. B(E) is the probability of ordinary reflection of electrons. A(E) is the probability of Andreev reflection, which is a special case not featured in the consideration of single particle excitations in table 3.1. Equating the energy of the initial electron state with that of the final hole state plus a cooper pair at the chemical potential gives

$$E_{ek} = E_{hk} + 2\mu \qquad \text{implying} \quad |E_e| = |E_h|. \qquad [3.25]$$

And so the hole is generated as far below μ as the electron was above. This model is one dimensional only, the three dimensional aspect appearing only in the boundary conditions: the junction is well-cooled and that the energy gap and electric potential rise to their full values on a scale shorter than ξ, the coherence length, on each side of the neck.

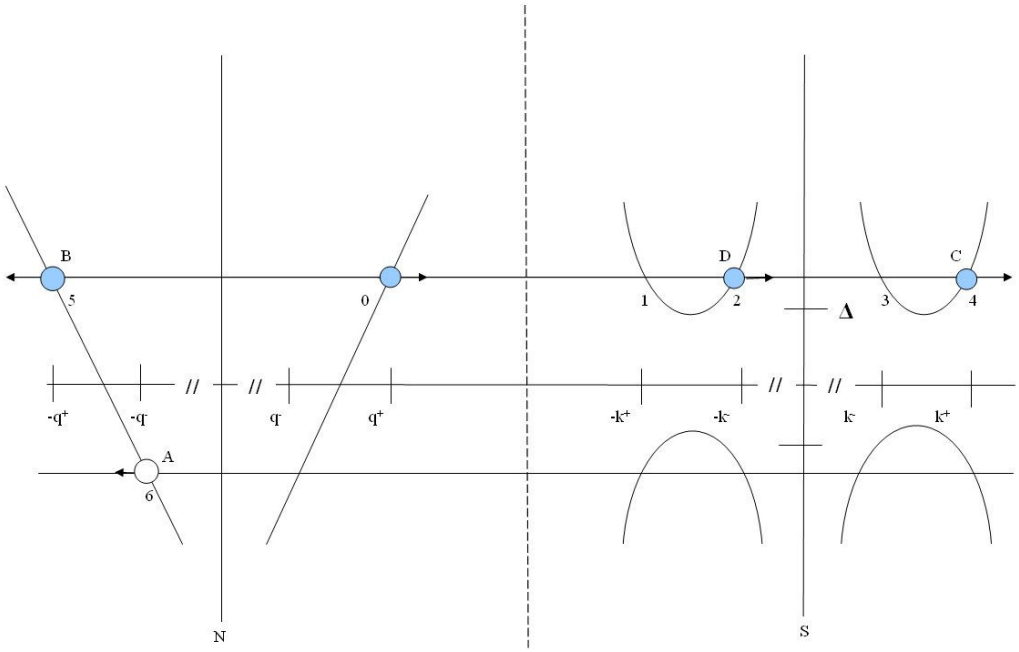

Figure 3.4: Schematic band structure of an N-S contact, showing the possible transition states at the interface. C and D represent quasiparticle states with a wavevector on the same side of the Fermi surface and opposite side, respectively. B represents ordinary reflection of electrons, and A represents an Andreev reflected hole.

To incorporate interfacial scattering into the model Blonder, Tinkham and Klapwijk introduce a dimensionless barrier strength Z which is considered to be a delta function located at the interface, $Z = k_F H / 2\varepsilon_F = H / \hbar v_F$, which includes effects such as an oxide layer on the surface, or disorder in the interface region. The probabilities A- D(E) can be calculated within the Bogoliubov equation formalism, and are given in table 3.2. An important point to note is that at E = Δ, A = 1, independent of Z, implying that the probability of all other processes is zero, by probability conservation.

Typically, experimentally, we measure the electrical behaviour of the junction, recording V-I or V-dI/dV characteristics. In order to compare our expectations from the BTK model to experimental data we must consider how these probabilities correspond to effective current and conductance across the junction. In general, on application of a bias voltage non-equilibrium quasi-particle populations will be

	A	B	C	D
$E<\Delta$	$\frac{\Delta^2}{E^2+(\Delta^2-E^2)(1+2Z^2)^2}$	$1-A$	0	0
$E>\Delta$	$\frac{u_0^2 v_0^2}{\gamma^2}$	$\frac{(u_0^2-v_0^2)^2 Z^2(1+Z^2)}{\gamma^2}$	$\frac{u_0^2(u_0^2-v_0^2)(1+Z^2)}{\gamma^2}$	$\frac{v_0^2(u_0^2-v_0^2)Z^2}{\gamma^2}$

Table 3.2: Reflection (A,B) and transmission (C,D) coefficients for arbitrary Z, $\gamma^2=[u_0^2+Z^2(u_0^2-v_0^2)]^2$*, and* $u_0^2=1-v_0^2=\frac{1}{2}[1+\sqrt{(E^2-\Delta^2)/E^2}]$ *(From Blonder et al. 1982).*

generated, which can only be found through solving the Boltzmann equation. However, this approach may be simplified if the junction is in the ballistic regime – this is a good approximation if the contact diameter is smaller than the mean free path within the metal. Choosing the chemical potential of the pairs within the superconductor as a reference, incoming electrons from the superconducting (S) side have the distribution $f_0(E)$ and those incident from the normal metal (N) side have distribution $f_0(E-eV)$. To calculate the total current, take the difference between the distribution functions at two points on either side of the interface and integrate over all energies, giving[4]

$$I = 2N(0)ev_F\sigma\int_{-\infty}^{\infty}[f_{\rightarrow}(E)-f_{\leftarrow}(E)]dE \qquad [3.26]$$

where σ is the effective cross-sectional area of the contact. As stated before

$$f_{\rightarrow}(E) = f_0(E-eV), \qquad [3.27]$$

and it follows that

$$f_{\leftarrow}(E) = A(E)[1 - f_{\rightarrow}(-E)] + B(E)f_{\rightarrow}(E) + [C(E) + D(E)]f_0(E) \qquad [3.28]$$

from the probabilities laid out earlier in this chapter. Substituting equations 3.27 and 3.28 into equation 3.26 provides, after simplifying, the total current I_{NS}

$$I_{NS} = 2N(0)ev_F\sigma\int_{-\infty}^{\infty}[f_0(E - eV) - f_0(E)][1 + A(E) - B(E)]dE\,. \qquad [3.29]$$

The second portion of the integral is an effective transmission coefficient for electrical current, enhanced by Andreev reflection A(E) and reduced by normal reflection B(E). By substituting in $A(E) = 0$ and $1 - B(E) = C(E) = (1 + Z^2)^{-1}$ equation 3.29 reduces to the form

$$I_{NN} = \frac{2N(0)e^2v_F\mathrm{A}}{(1 + Z^2)}V \equiv \frac{V}{R_N} \qquad [3.30]$$

for the case of a normal state junction. From this it may be noted that even in the absence of a barrier (Z=0) there is still an intrinsic resistance to the junction.

The BTK model, while a complete and widely accepted description of normal metal/superconductor junctions, does not address the case in which the metal is a ferromagnet. As has been stated before, Andreev reflection is a useful tool for determination of the spin polarisation of magnetic materials; indeed, this is the focus of chapter 5 of this thesis, where PCAR is used to determine the spin polarisation of several rare earth-intermetallic compounds. A simple model of spin polarised Andreev reflection was described earlier in this chapter (Equation 3.19). While this model holds in some simple cases, it includes no consideration of interfacial scattering (the Z parameter), neither of the local temperature of the contact, nor of the spreading resistance.

For a more complete model of Andreev reflection, including spin-split conduction channels and inclusion of the physics mentioned above, we look to the work of Mazin *et al.*[64]. Firstly, the half-metallic regime where the metal is 100% spin

polarised must be considered. Following the notation of the BTK formalism we consider an incoming plane wave

$$\psi_{in} = \begin{pmatrix} 1 \\ 0 \end{pmatrix} e^{ikx}. \qquad [3.31]$$

The reflected state of this wave will differ from that of the zero spin polarisation case; the Andreev reflection component with coefficient a is now described by an evanescent wave, with the normal reflection described as a plane wave

$$\psi_{refl} = a\begin{pmatrix} 0 \\ 1 \end{pmatrix} e^{\kappa x} + b\begin{pmatrix} 1 \\ 0 \end{pmatrix} e^{-ikx}. \qquad [3.32]$$

The transmitted components are described as stated in the BTK method

$$\psi_{tran} = c\begin{pmatrix} u \\ v \end{pmatrix} e^{ikx} + d\begin{pmatrix} v \\ u \end{pmatrix} e^{-ikx} \qquad [3.33]$$

including the two components c and d (with and without branch crossing). Here $u^2 = 1 - v^2 = (1+\beta)/2$, where $\beta = V / \sqrt{\left| V^2 - \Delta^2 \right|}$. The total current due to half-metallic conduction channels is

$$\frac{G_{HS}}{G_0} = \frac{4\beta[1+(K-2Z^2)^2]}{4(1-\beta^2)Z(K-Z)+[1+(K-2Z)^2][(1+\beta)^2+4\beta^2Z^2]} \qquad [3.34]$$

for $eV > \Delta$, where the Landauer conductance of a single electron $G_0 = e^2/h$, and $K = \kappa/k$. Taking K as infinity, as the value of K is only important for a small region of voltages above the gap, the total interface current in the ballistic non-magnetic (P=0%) and half-metallic (P=100%) regimes is given in table 3.3, for $E < \Delta$ and $E > \Delta$. Note that the conductance is zero in the half-metallic regime for energies below Δ, as required, Andreev reflection is completely suppressed in a 100% spin polarised

	$eV < \Delta$	$eV > \Delta$
Ballistic non-magnetic	$\frac{2(1+\beta^2)}{\beta^2+(1+2Z^2)^2}$	$\frac{2\beta}{1+\beta+2Z^2}$
Ballistic half-metallic	0	$\frac{4\beta}{(1+\beta)^2+4Z^2}$

Table 3.3: Total interface current in the ballistic non-magnetic (P=0%) and half-metallic (P=100%) regimes, for the two regions separated by the superconducting band gap Δ (From Mazin et al. 2001).

material.

As stated earlier in this chapter, interfacial scattering is incorporated into the BTK theory of Andreev reflection through the *Z* parameter, which models the effect of interfacial scattering through a delta function potential at the N-S interface. *Z* is, naturally, also included in the Mazin *et al.* model of spin-polarised Andreev reflection as detailed by equation 3.34 and table 3.3. The effect of varying *Z* within this model can be seen in figure 3.5, where Z is varied from 0 to 0.255, while maintaining *P* at a constant value of 0.42, approximately the spin polarisation of Fe obtained from PCAR measurements[62,65]. The superconducting gap energy Δ is also fixed at the bulk value for Nb at 0K, known as 1.525meV from BCS theory. The curves were generated using the MATLAB software suite, through substitution of the interface transparency [1 + *A*(*E*) - *B*(*E*)] from table 3.3 into the expression for the total interface current (eq. 3.29). The Mazin *et al.* model was used throughout this thesis for fitting of experimental data, due to its high applicability to ballistic SC-FM junctions, allowing extraction of the spin polarization parameter P for junctions displaying varying degrees of interfacial scattering.

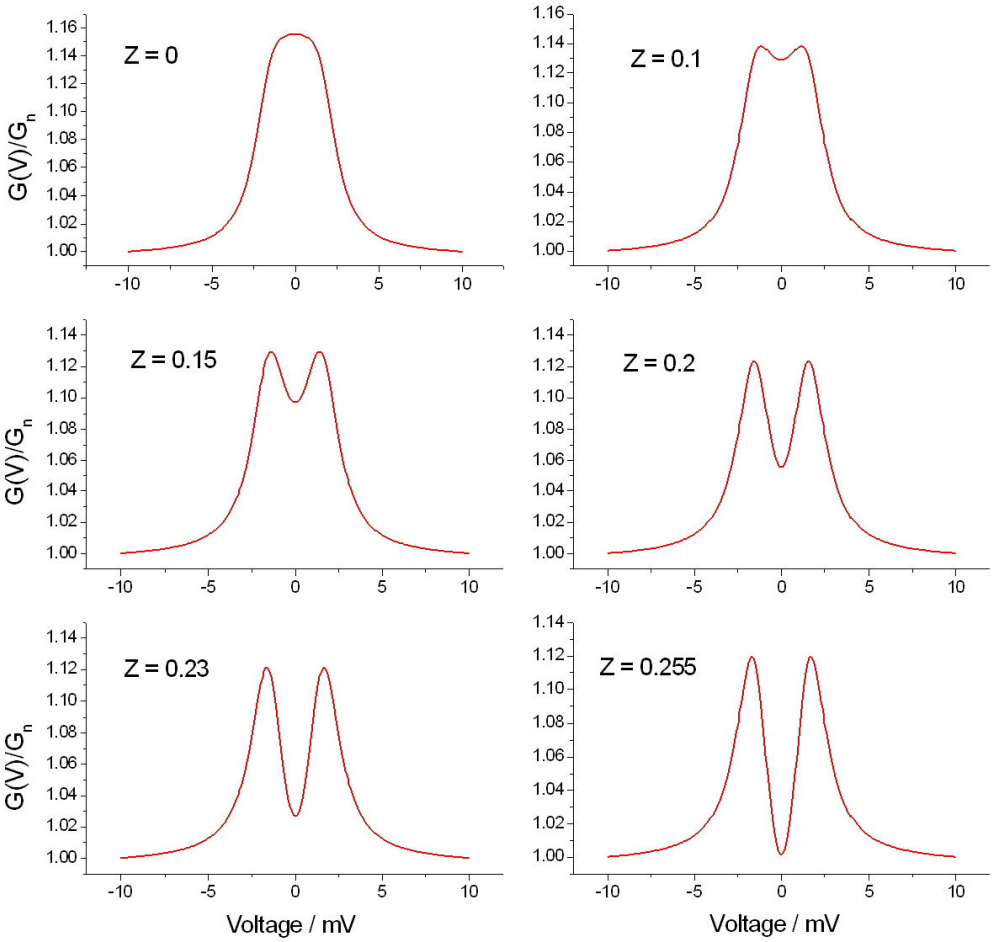

Figure 3.5: Theoretical differential conductance plots for hypothetical junctions displaying point contact Andreev reflection, with varying degrees of interfacial scattering characterised by the Z parameter, calculated within the Mazin et al. model. Additional parameters: P = 0.42 , Δ = 1.525meV , T = 4.2K.

3.3: Recent PCAR Research

Shortly after publishing their seminal theoretical paper detailing the I-V behaviour of normal metal (N) to superconductor (S) microconstrictions, Blonder *et al.* demonstrated the agreement between experiment and theory by examining point contacts of Nb wire to a Cu disc[66]. Through use of a mechanical polishing technique followed by a chemical etch in HNO_3:HF:acetic acid (5:4:1) they created a rough yet clean surface on the Cu, finding that this provided for a wider variation in the interfacial scattering Z than for a smooth disc. They created a point on a 75μm

diameter wire by using electrochemical etching in the same solution as was used for polishing the Cu disc. The point contact was made at ~1.3K in a pumped helium bath, and upon initial contact they found the resistance to be in excess of 100Ω, and the I-V curve obtained to be completely ohmic in character, with no superconducting behaviour observed.

This led them to define three regions in which the point contact could be categorised; in the high resistance (>100Ω) region they surmised that the contact was between the oxide layers at the surface, Cu_2O, a semiconductor, and Nb_2O_5 a semiconductor with a high density of states near to the surface of the Nb. The electric field remains entirely contained within this oxide layer, and as such a linear I-V curve is observed, the layer acting to decouple the conduction electrons. On remaking the contact several times, they saw contact resistances of 1-100Ω with strong non-linear behaviour as expected from theory, and they considered that the oxide layer had been largely eroded away and the contact has entered the Sharvin limit with the contact radius smaller than the mean free path. In this region they observed behaviour consistent with their theoretical work, confirming their predictions for a wide range of Z values. Despite having to make a number of simplified assumptions, their results demonstrated that the behaviour of N-S point contacts is dominated by Andreev reflection at bias voltages near the superconducting band gap Δ.

Studies have been made, using Andreev reflection, on exotic high temperature superconductors, in order to determine critical parameters such as Δ and the coherence length ξ. Pleceník *et al.*[67] studied the superconductor $Bi_2Sr_2CaCu_2O_y$ (BSCCO) using a point contact of a sharp tip of Au to a film of the superconductor at a temperature of 10K, well below the critical temperature of 80K. They found that the characteristic peaks in the PCAR differential resistance curve near to the superconducting gap Δ were smeared, with the BTK model giving a poor fit to the data. They proposed the idea of inelastic scattering at the interface, causing the lifetime of quasi-particles near to the surface to be shortened, as a consequence of degradation of the surface layers at the N/S interface. This was introduced into the BTK model as an additional inelastic scattering term in the Bogoliubov equations, in the expressions for the functions $F(x,t)$ and $G(x,t)$

$$i\hbar\frac{\partial F(x,t)}{\partial t} = -\frac{i\hbar}{\tau}F(x,t), \qquad [3.35]$$

where τ is the lifetime of the quasiparticles between collisions. Solving the Bogoliubov equations in the manner of BTK gave them expressions for the reflection coefficients A and B, allowing the total interface current to be determined as shown previously. Utilising the concept of an effective value for Z (Z_{eff}) as introduced by Blonder *et al.* for a junction between two metals with non-identical Fermi velocities, they were able to extract a value for the Fermi velocity in BSCCO, and from this the coherence length using the relation $\xi = \hbar v_F / \pi\Delta(0)$, yielding ξ = 3.5nm.

Building on earlier work examining contacts of the type-I superconductors Sn, In and the type-II superconductor Nb to normal metals (Ag, Cu, W), in which Naidyuk *et al.* similarly introduced an inelastic scattering term to the BTK model to fit their experimental curves, Häussler *et al.*[68] studied point contacts of Ag to $(Mo_{0.55}Ru_{0.45})_{0.8}P_{0.2}$, an amorphous superconductor, under an applied magnetic field. They found that features associated with Andreev reflection at low voltage bias could persist up to fields greatly exceeding B_{c2}, the second critical field in the bulk superconductor, and proposed that this was due to significant shortening of the mean free path and therefore the coherence length due to introduction of defects while forming the contact mechanically. However, in the amorphous superconductor, where the high normal state resistivity gives a mean free path of a few Å, Andreev behaviour disappears at the bulk critical field B_{c2}, implying that the dominant mechanism is indeed the presence of local defects at the point contact.

Additionally, they saw peaks in the differential resistance characteristic dV/dI at current density values of the order of 1×10^6 A/cm^2. This is sufficient to generate a local field of the order of the thermodynamic critical field, estimated as 86mT from specific heat measurements. These peaks move as the contact temperature is raised, towards decreasing voltage values, representing a decreasing critical field, in line with the temperature dependence of the critical field from BCS theory. Additionally the behaviour of the contact under an applied magnetic field agrees closely with that expected of a type-II superconductor in the vortex state, with the order parameter

dependence $(1-B/B_{c2})^{1/2}$, where B_{c2} is the bulk second critical field. Rybaltchenko *et al.* studied point contacts of Ag to RNi_2B_2C compounds (R=Y, Er, Ho) in which they observed similar effects[69], which they attributed to the suppression of superconductivity in the contact area by the applied current, resulting in an increase in resistance. These features behaved in a similar manner to those observed by Häussler *et al.* as the temperature was increased towards T_c, vanishing at this point. They also found that the extracted value of T_c was larger than expected for the Ho based compound, by comparison to the other compounds, with $2\Delta/k_BT_c = 2.8$, 3.7 in the Y and Er based compounds. They attributed this to an unknown superconducting state developing between 6.5K and T_c = 8.5K, due to an antiferromagnetic transition at these temperatures; at 6K a spiral magnetic order sets in, followed by commensurate antiferromagnetic order at 5K.

The first measurements of Andreev reflection spectra between a ferromagnetic metal and a superconductor were made roughly simultaneously by Soulen Jr. *et al.* and Upadhyay *et al.* in 1998, the primary difference between their methods being the type of point contact used – mechanical or thermally deposited respectively. Upadhyay *et al.*[70] studied the Andreev behaviour of three metals, non-magnetic Cu and ferromagnetic Co and Ni through thermal deposition of the metal onto a nitride inter-layer with a tapered nano-hole of 3-10nm in diameter, on a layer of superconducting Pb. They found a clear suppression of the Andreev-related peak at zero bias for Co and Ni from the value expected for a non-magnetic metal; for Cu they found the behaviour expected, with full Andreev behaviour, extracting the contact spin polarisation P_C = 0%. They used a model based on that of de Jong *et al.*, that includes the spin polarisation as a modification of the Andreev reflection parameter A by the factor $(1-P_C)$[71], and generalised this model based on the methods of BTK to account for arbitrary scattering at the interface. Fitting of this model to their data allowed them to extract values of P_C = 37±2% and 32±2% for Co and Ni respectively. Measurements of dR/dV for these junctions showed clear peaks corresponding to the phonon frequencies of Pb, suggesting that their contacts were of good quality, with negligible impurity scattering.

Soulen Jr. *et al.*[62] measured a wider range of materials, also studying PCAR spectra of Co and Ni, with both Nb and Ta, NiFe, and also three candidates for fully spin polarised materials (half metals), NiMnSb (A Heusler alloy), $La_{0.7}Sr_{0.3}MnO_3$ and CrO_2. They used a mechanical point contact technique, pressing a tip of mechanically polished Nb or Ta into a film or foil of the material studied. They also reversed the geometry of the experiment for Fe, pressing a tip of Fe into a film of superconducting material; they found this gave little deviation of the extracted spin polarisation from the initial geometry, as would be expected. Extracted spin polarisations, using fitting to a modified BTK model, were significantly larger than those observed by Upadhyay *et al.*, with P_C = 42±2% and 44-46.5% for Co and Ni respectively, the value for Ni varying slightly dependent on the superconductor used to make the contact, and on the sample type (foil or sputter-grown film). It is worthwhile to note that for the half-metal candidates examined, only CrO_2 came close to full occupation of a single spin sub-band, with an extracted P_C = 90±3.6%.

Continuing their earlier work, Upadhyay *et al.* moved to studying ultra-thin films of Co, again using a thermal deposition technique[72]. Their samples comprised a relatively thick film of Pb, on which they deposited a film of Co of 0.2 to 3.5nm in thickness, followed by a thin membrane of silicon nitride with a nanohole in it. Deposition of Cu onto this structure allowed formation of a point contact 3-10nm in diameter to the Co/Pb underlayer. PCAR spectra at a range of resistances between 5-50 ohms revealed, upon fitting, a clear reduction in the transmission spin polarisation of the Co. This was most notable at 0.2nm thickness, with a 25% reduction, on increasing the thickness they found the spin polarisation tended towards the bulk value reported they had reported previously.

Repeating the PCAR measurements of the ferromagnetic 3d transition metals (Ni, Co, Fe) by Soulen Jr. *et al.* and Upadhyay *et al.*, Strijkers *et al.* aimed to present a methodical approach to spin polarisation determination[65]; previously reported values varied wildly by up to 10%. They utilised a mechanical point contact technique, with a differential screw system for adjustment of the contact, the point being fashioned by electrochemical etching in potassium hydroxide. They found, by measuring PCAR differential conductance spectra between niobium and the three metals, P_C values of 37±1%, 45±2% and 43±3% for Ni, Co and Fe respectively. These polarisation values

agree well with those obtained using a superconducting tunnel junction method[73], within a few percent. P_C was found to strongly depend on the extracted value of Z, the interfacial scattering parameter, a higher Z typically resulting in a reduced contact polarisation. They attributed this to the negative effect of scattering at the interface on the spin polarisation; formation of oxides at the surface and also metal/Nb alloying can be expected to cause spin mixing effects that will dilute the intrinsic spin polarisation of the bulk transition metal.

PCAR spectra obtained by the same authors for point contacts of Nb to Cu showed pronounced dips in the differential conductance at voltage bias values close to the bulk superconducting gap Δ for Nb. The authors attributed this behaviour to the development of a proximity layer at the surface of the Cu, generated by close contact to the Nb tip. This behaviour can be modelled by considering the system to have two effective gap values, Δ_1 and Δ_2, where the second value represents the bulk, and the first value is lower and represents the proximity layer, which can be expected to have a lower transition temperature and gap value[74]. The Andreev reflection process can now be considered to be occurring at the interface between the metal and the proximity layer, and thus can only occur at bias voltages below Δ_1, however quasi-particles can only enter the superconductor above Δ_2. Incorporating this effect into their modified BTK model produced the expected dips, in good agreement with experiment. The authors also found a dependence of the observed superconducting gap values with resistance, a sharp decrease approaching 3Ω that they attribute to suppression of superconductivity in the tip as the contact diameter approaches the coherence length ξ = 38nm for Nb. The ratio Δ_1/Δ_2 was found to remain constant at 0.5 for clean contacts, where the proximity effect should be most pronounced.

Expanding on the initial work of R.J. Soulen Jr. *et al.* in studying $La_{0.7}Sr_{0.3}MnO_3$, much interest has been shown in this series of LaSrMnO (LSMO) compounds. These doped manganates have generated a lot of interest, and they notably show what is known as colossal magnetoresistance (CMR), an effect which can show magnetoresistance ratios of several thousand percent. They are also potential candidates for half metals, that is materials with no minority spin sub-band, and have been examined by Andreev reflection in an attempt to determine their degree of spin polarization. PCAR differential conductance spectra obtained by Osofsky *et al.* using a

standard mechanical point contact technique demonstrated contact spin polarizations P_C of approximately 70% for a sputtered thin film of $La_{0.7}Sr_{0.3}MnO_3$ and 80% for a crystal sample[75], using a simple model assuming $Z = 0$ and using the peak conductance value at zero bias to estimate P_C[62]. They attributed this variation in polarization values to effects due to variation in surface morphology and also paramagnetic impurity inclusions, suggesting that the extracted polarization values should be treated as a lower bound to the intrinsic value of the material.

Further measurements on the same material by Nadgorny *et al.* revealed a strong dependence of P_C on the residual resistivity of the LSMO film[76], engineered by variation of the substrate temperature and the deposition rate during sputtering and pulsed laser deposition. The spin polarisation was found to vary from ~58% for a 40μΩcm film, increasing to a maximum of 92% for a 2000μΩcm film, again demonstrating a strong dependence of the observed spin polarisation on the sample quality. They directly correlated this with the calculated carrier mean free path in the material, showing that as the residual resistivity is changed the sample moves between regimes, from ballistic to diffusive. They considered that LSMO can be defined as a transport half-metal, as the spin polarisation approaches 100% in the high resistivity limit. However, the presence of minority spin electrons at the Fermi level suggests that LSMO is not a true half metal, and that the high spin polarisation is primarily due to the difference in mobility between the spin channels, manifesting in a high transport spin polarisation. Ji *et al.* studied a different composition ($La_{0.6}Sr_{0.4}MnO_3$), in which they found a very similar value for P_C (83%)[77], through extrapolation to $P_C(Z = 0)$, the intrinsic value of spin polarisation. They considered that this was valid due to spin-flip scattering processes being more prevalent with a large barrier at the interface and also bulk scattering, both playing a role in increasing Z. Spin-flip scattering can be expected to dilute the effective spin polarisation, hence extrapolating to $P_C(Z = 0)$ is expected to give the intrinsic polarisation of the material.

There are two extremes that exist in point contact Andreev reflection measurements, corresponding to the nature of transport across the interface: Ballistic and diffusive. Mazin *et al.* developed two models[64], each describing one of these extremes, by extending the BTK model to spin-dependent transport, and generalising to the diffusive regime, as detailed earlier. Local-density approximation calculations

performed by Xia *et al.*[78] on experiment results obtained by different authors[70] suggested that these models may in fact be oversimplified for accurate fitting of experimental data, due to the catch-all nature of the Z parameter. Woods *et al.* performed PCAR measurements on ferromagnetic oxides[79], fitting to both ballistic and diffusive models in order to make a systematic study of the applicability of these two models. It had been shown previously that, generally, both models can provide a good fit to the data, however dependent on the model used the value of the interfacial scattering parameter Z extracted will change[76]. P_C is typically found to remain roughly constant, independent of the model chosen to fit the experimental data. Woods *et al.* performed a theoretical test of this observation, generating a large number of diffusive PCAR curves and then fitting these with the ballistic model. The difference in Z between the two regimes was found to be large, around 0.5-0.6 for the lowest values of Z_d (fixed diffusive parameter). However, P_C was found to be largely constant, with ~3% maximum difference between the input diffusive parameter and the ballistic parameter extracted from fitting. This finding illustrates the power of the BTK formalism, which may at first appear to be over-simplified – the Z parameter, which is essentially a δ-function at the interface, manages to absorb the additional physics of the diffusive regime, and reproduce the same value of contact spin polarisation.

Woods *et al.* also noted the importance of interface effects on the superconductivity of the tip, particularly magnetic scattering of Cooper pairs, resulting in suppression of the critical temperature T_C and smearing of the density of states[80]. These effects can be modelled by incorporating an effective temperature into the model that is higher than that which has been experimentally measured. In addition, this approximation can be used to incorporate local heating of the contact due to the potentially high current density through the typically nm-size constriction[81]. If the temperature is left as a free parameter in the fitting, typically it is found to be higher than that measured experimentally, due to incorporation of the above effects.

Chapter 4: Experimental Techniques

Through producing the results detailed in this thesis a range of equipment and techniques were used. This chapter outlines the techniques used and gives details of the specific equipment used to obtain experimental data. Construction of two superconducting magnet inserts is described, with CAD diagrams and photographs. These inserts were designed to fit a 20mm bore Oxford Cryogenics 14/16T superconducting helium-cooled magnet system, for the purposes of carrying out point contact measurements on thin film samples. These measurements are described in the following chapters (5 through 8) where details are given of Andreev reflection and other point contact transport phenomena in non-magnetic and ferromagnetic metallic film samples. Details are also given of the electronics set-up used to measure and record point contact I-V and dI/dV-V curves in these experiments. A Leo Scanning Electron Microscope (SEM) system was used to image the mechanically fabricated metal tips used in these point contact experiments, and for film thickness characterisation. The basic physics behind scanning electron microscopy are described in this chapter, alongside details of the particular microscope used. The RFe_2 films and multilayers measured in the following chapters were deposited using the Molecular Beam Epitaxy (MBE) technique, which is also described in this chapter, alongside the typical growth conditions used for deposition of these samples. Additionally, a number of film and bi-layer transition metal samples were deposited using DC magnetron sputtering, and this technique is described here.

4.1: Inserts for Point Contact Measurements

In order to carry out point contact measurements of thin films a pair of superconducting magnet inserts were designed and constructed in-house. The 14/16T magnet system used requires inserts to fit a 25mm bore. The inserts are of similar construction overall but with different sample holders, designed to facilitate different orientations of samples with respect to the applied magnetic field, which is along the long axis of the magnet. Required configurations are with magnetic field in the plane and perpendicular to the plane of the thin film sample. For field perpendicular-to-plane measurements the design is more straightforward, as shown in figure 4.1. The system is designed so that the point may be screwed down directly onto the surface, using a control knob at the top of the insert that is easily accessible. The knob is connected to the tip holder via a rod with a differential screw system, mounted on beryllium copper leaf springs. The top portion of the screw has a coarser thread than the lower portion (see inset, figure 4.1), and by running the top portion through a fixed thread while the lower is sprung using leaf springs, the resultant motion of the lower portion on a full rotation of the screw is 100μm. The differential screw allows micron scale adjustment of the tip position, essential to make contact while avoiding damage to the tip or sample surface.

To carry out field in-plane measurements the sample holder design was modified to allow the sample to be mounted along the side wall of the insert. To make a point contact to the sample in this configuration requires the point to be brought in horizontally; this is achieved by mounting the tip on a spring loaded cantilever as shown in figure 4.2. This allows use of a similar design for the main body of the insert as for the perpendicular-to-plane insert, instead of pressing the tip directly into the sample surface the differential screw presses on the cantilever, moving the tip horizontally towards the sample. All sprung elements throughout the system are manufactured from beryllium copper to give excellent and consistent spring flexibility down to liquid helium temperatures. The sample holder is made of brass for good thermal conductivity and also because of its non-magnetic nature, and the main body of the inserts comprises thin stainless steel tubing of a highly non-magnetic grade.

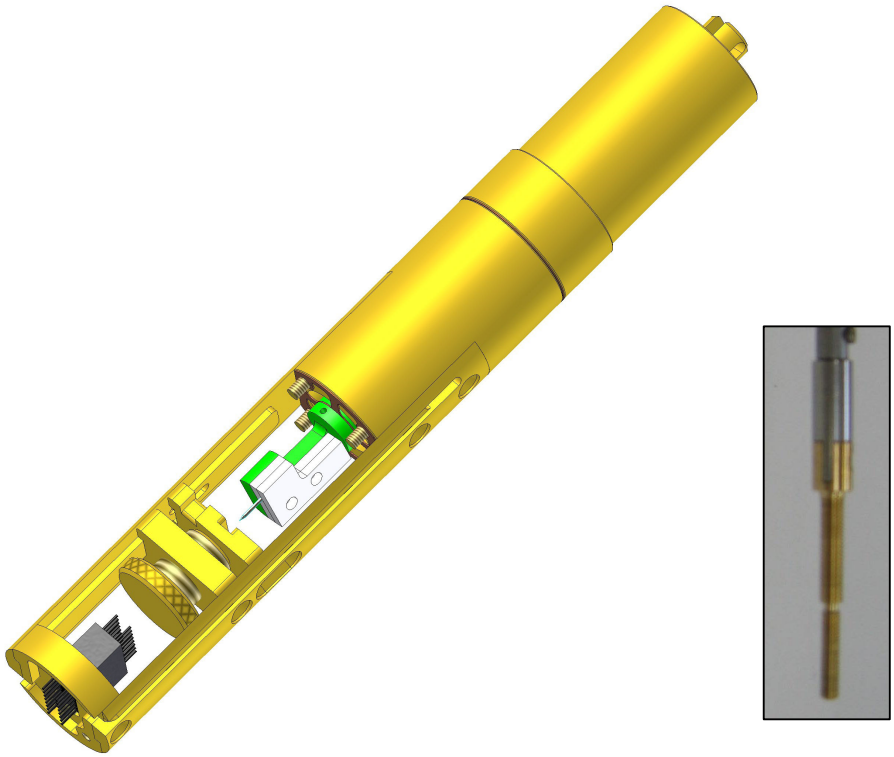

Figure 4.1: CAD construction showing the layout and construction of a point contact insert designed for field perpendicular-to-plane measurements. Inset: Differential screw used for fine adjustment of tip height relative to sample.

Electrical contact to the sample surface and the tip is made using fine copper wires, terminated at the base of the insert. Accurate temperature control at the sample/tip interface is required for obtaining reliable results, and also reliable fitting to theoretical models in which temperature is a parameter. A Lakeshore 340 Intelligent Temperature Controller (ITC) was used to control temperature at the sample surface; temperature is read via a Cernox temperature sensor mounted on the sample platform, directly beneath the sample itself. The sample can be heated through a wound constantan wire heater, with high resistivity. Using this method it is possible to maintain a constant temperature to within 10-100mK of the target temperature. All wires contacted to the sample surface, and those used for temperature control, run up through the body of the insert, interfacing with the electronics via a 16-pin connector.

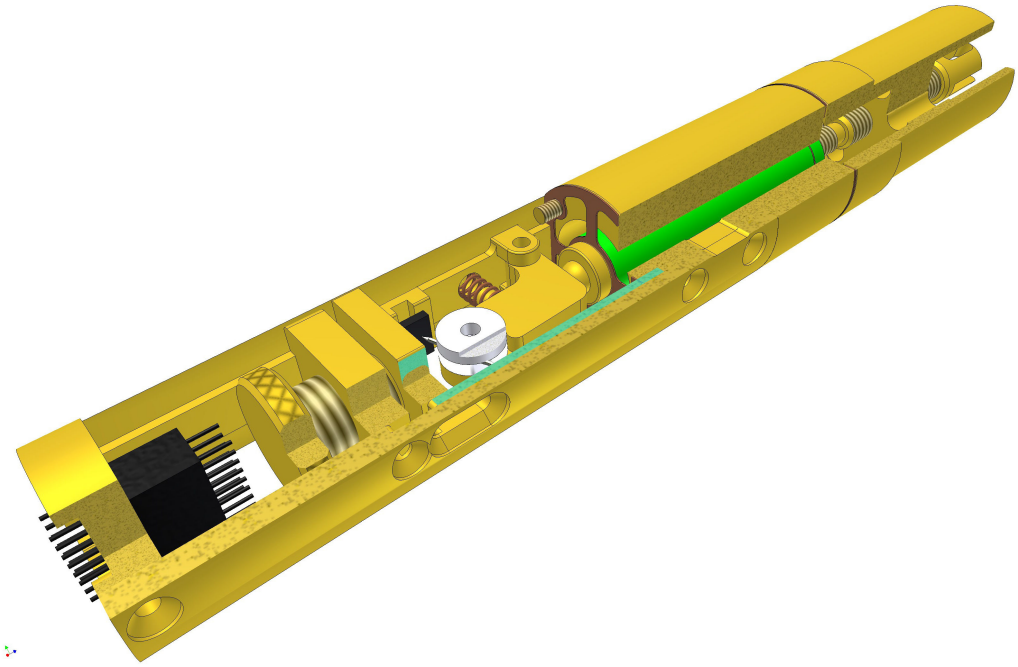

Figure 4.2: CAD drawing showing the layout and construction of a point contact insert designed for field in-plane measurements. Also visible is the differential screw system within the body of the insert.

For measurements in which an external magnetic field was required, a superconducting magnet with a maximum field strength of 14T was used. The magnet itself is cooled with liquid helium, a jacket of which surrounds the magnet. To reduce He losses, this system is isolated from the laboratory environment through a vacuum space at ~10^{-6}mbar, followed by a liquid nitrogen jacket, and finally a second vacuum space at a similar pressure to the first. The sample, mounted on an insert, is placed in a variable temperature insert between the magnet coils, into which liquid He can be leaked at a slow rate through a needle valve from the magnet He jacket. An Oxford Instruments ITC4 is used to control the temperature in the sample space externally to the insert. A Cernox sensor is used to measure the temperature, and a wound heater can be used to provide heating to balance the cooling rate provided by the small He flow rate, allowing a constant temperature to be maintained, or a controlled rate of cooling/heating.

When no external field is required and measurement at 4.2K is sufficient, the insert was placed directly into a liquid He dewar to perform the measurements. While

this method provides no way to vary the temperature of the sample, the temperature can be measured accurately using the Cernox sensor mounted beneath the sample. If the system is allowed to settle for a period of time before measurements are taken, the temperature will stabilise sufficiently. Complete immersion in liquid He prevents local heating effects from causing anomalies in the measured curves.

A schematic representation of the electronics used for measuring *I*-*V* and d*I*/d*V*-*V* curves can be seen in figure 4.3. In order to make *V*-*I* and d*I*/d*V* measurements across the contact between a tip and a given sample, a voltage is applied using a function generator with a high output impedance. The resultant current flow is measured in series using a digital multimeter (DMM), while a second DMM measures the voltage across the contact. Detection of the differential conductance signal is made by application of a 2kHz sinusoidal 6mV signal across a Wheatstone bridge resistor arrangement, and detection using a lock-in amplifier at this frequency. The difference between the points A and B in the circuit measures the differential conductance relative to the balanced state, determined by the value of the variable resistor.

The tip and sample are both connected to a Keithley 199 Digital Multimeter (DMM), which allows measurement of the voltage drop across the junction. A second pair of wires connects the tip and sample to a Wheatstone bridge arrangement with 2kΩ resistors. A variable resistor box is used to balance the bridge, providing maximum sensitivity when the balancing resistance is equal to the contact resistance. A Thurlby Thandar Instruments TG1010 Programmable 10MHz DDS Function Generator is used to apply a slow varying (~3mHz) DC voltage across the point contact. The resultant current is measured in series using a second Keithley 199 DMM. A 2kHz sinusoidal 600mV signal is superimposed on this DC voltage, using the sine out function of a Stanford Research Systems (SRS) SR830 DSP Lock-in Amplifier. This is passed through an SRS SR554 Transformer Pre-Amplifier to provide isolation from the common ground potential, preventing the formation of ground loops. The measured d*I*/d*V* signal is obtained by using the lock-in amplifier set to a frequency of 2kHz, recording the difference in signal between points A and B on the bridge circuit (A-B). The signals *I*, *V* and d*I*/d*V* are recorded on a PC using HP Vee, via an IEEE interface.

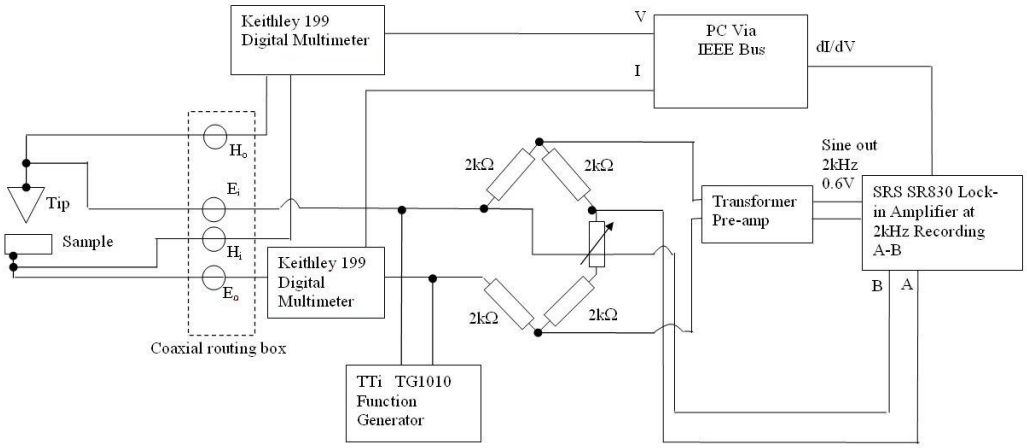

Figure 4.3: Schematic showing the electronics used for measuring I-V and dI/dV-V curves across point contact junctions.

For comparison of experimental V-dI/dV ($G(V)$) curves to the theoretical description outlined in section 3.2, we require that they are normalised relative to the normal junction conductance, when Andreev reflection effects are completely suppressed due to high applied voltage across the contact. Experimentally, this normal state conductance G_n is approximated to the value of $G(V)$ at high bias voltage, when the curve is essentially flat. If we consider the contributions to the resistance of the contact, we can split the signal into two parts: R_n, the normal state resistance, and ΔR, the additional resistance due to, for example (but not limited to), Andreev reflection

$$\frac{dV}{dI} = R_n + \Delta R \,. \qquad [4.1]$$

Inverting this expression to obtain the differential conductance, and dividing through by the normal state conductance, we can obtain an expression for the normalised conductance

$$\frac{G(V)}{G_n} = \frac{R_n}{R_n + \Delta R} \quad \text{where} \quad G_n = \frac{1}{R_n}. \qquad [4.2]$$

Experimentally we measure ΔR as a voltage signal on a lock-in amplifier, which may be converted into a resistance value using a normalisation parameter α. This parameter was determined by maintaining the point contact side of the bridge at a constant resistance value, while incrementally varying the variable resistor and monitoring the lock-in voltage signal V. For the results presented in the following chapters, $\alpha = 28.59\mu V/\Omega$. Inserting $\Delta R = V / \alpha$ into equation 4.2 and simplifying, we find

$$\frac{G(V)}{G_n} = \left(1 + \frac{V}{\alpha R_n}\right)^{-1} . \qquad [4.3]$$

This expression is used throughout the PCAR results presented in chapters 5, 6 and 7 to normalise the curves relative to the normal state conductance of the contact, facilitating fitting of the data to the model of Mazin *et al.* outlined in section 3.2.

4.2: Scanning Electron Microscope

Scanning electron microscopy (SEM) is a powerful technique for obtaining topographical images of surfaces and features with potentially nanometre resolution[82]. SEM is a surface and near surface technique, in contrast with for example transmission electron microscopy which, while similar, provides information about internal structure. Figure 4.4 shows a photograph of the Leo 1455 VP SEM system used to obtain the images shown in this thesis. The electron source used in this microscope was initially a simple tungsten filament, with electrons emitted via thermionic emission. Towards the end of the author's period of use the microscope was upgraded to use a Lanthanum Hexaboride (LaB_6) emission source, which provides improved brightness and allows for a reduced spot size, improving microscope resolution limits.

SEM systems operate by producing a scan or raster of the electron beam across the sample, and using the detected current of secondary electrons (or other radiation) from the surface to build up an image. Magnetic lenses are used to condense and focus the beam to a point of a few nanometres. In traditional SEMs, the beam is

Figure 4.4: Photograph showing the LEO 1455 VP scanning electron microscope in the Nanomaterials Rapid Prototyping Facility at the University of Southampton.

deflected by a set of scan coils to produce a raster of the surface. Simultaneously the spot of a CRT is scanned across the screen, the brightness modulated by the amplified current from the detector. In modern digital SEMs this scan is produced by digital control of the electron beam, with direct display of the image on a computer screen. Image magnification is straightforward – the raster on the sample surface is set to be smaller than that on the screen, resulting in linear magnification that requires no lenses.

On interaction with a material, electrons incident with energies typical for SEM (1-20keV) scatter inelastically, resulting in the generation of various types of radiation. Secondary electrons, produced mainly from interaction with the primary electrons entering the specimen, are used to produce standard topographical electron micrograph images in the SEM. The yield of secondary electrons from the sample is roughly constant as the atomic number of the sample atoms varies. However for backscattered electrons there is a strong dependence, making backscatter detection

ideal for determining crystallographic or compositional information about the sample. Secondary electrons have the smallest sample interaction volume (excluding Auger electrons, not detected in standard SEM systems) and thus provide the best spatial resolution.

Detection of secondary electrons is made via a scintillator-photomultiplier system which is known as an Everhart-Thornley detector. Secondary electrons have typical energies of 10-50eV, which is too low to excite a scintillator, therefore an aluminium film carrying a bias voltage of around 10keV covers the scintillator, to energise the electrons. A metal grid called the collector surrounds the scintillator, this is at a potential of a few hundred volts and serves two purposes. The collector improves the efficiency of electron collection, by attracting secondary electrons, including those with trajectories away from the detector which would not have been otherwise collected. This improves the signal obtained through secondary electron detection. In addition to this purpose, the collector also shields the main electron beam incident on the sample, preventing deflection of the beam by the highly biased aluminium film.

4.3: Molecular Beam Epitaxial Growth

Molecular beam epitaxy (MBE) is a technique that was originally developed for semiconductor growth. However, more recently it has been applied with great success to metallic systems, allowing highly epitaxial growth of magnetic films and multilayers with almost atomically sharp interfaces. The RFe_2 samples measured in this thesis, both films and multilayers, were deposited using this technique, by Roger Ward of Clarendon Laboratory, Oxford using a Balzers UMS 630 UHV facility. A schematic drawing of this equipment is shown in figure 4.5. The apparatus is split into two parts, with sample deposition taking place in the main chamber, and a separate loadlock that allows samples to be inserted and removed from the chamber without returning the entire system to atmospheric pressure. Deposition is typically performed under a base chamber pressure of $\sim 4\times10^{-8}$mbar, using two effusion cells and three

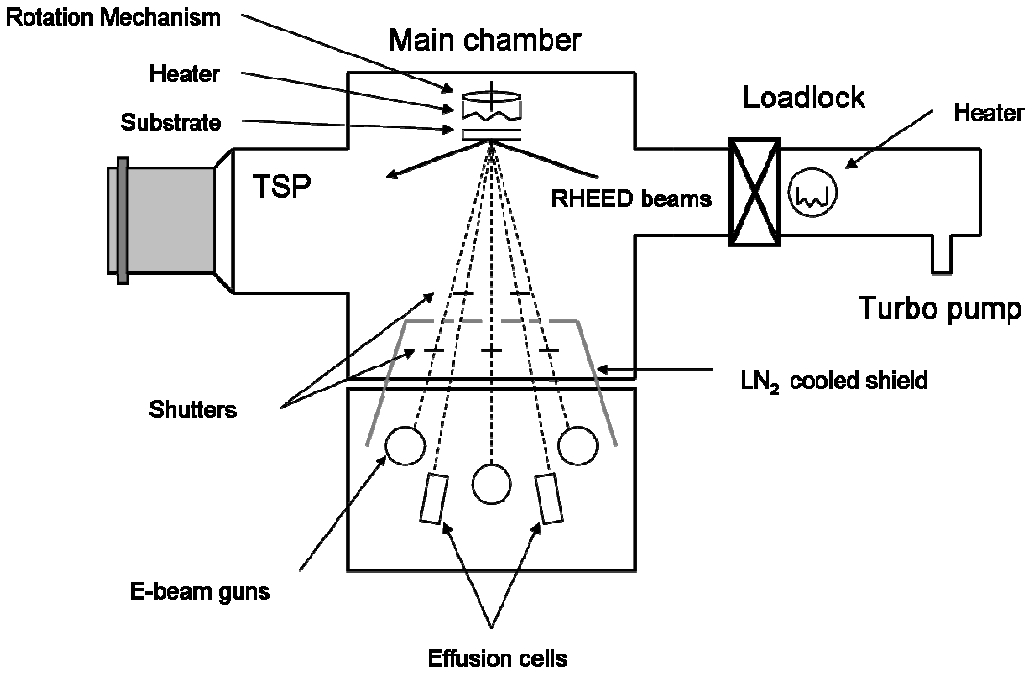

Figure 4.5: Schematic diagram of an MBE system, used for epitaxial growth of films and multilayers (Courtesy of K.N. Martin).

e-beam guns. The chamber is pumped by both a Titanium Sublimation Pump (TSP) and a turbo pump. Effusion cells are heated using a resistive heating element, and are suitable for evaporating sources with a high vapour pressure below 1300°C. When this technique is insufficient, the e-beam guns may be used to bombard the sources with high energy electrons, allowing deposition of materials which do not easily evaporate. Shutters are used to isolate sources of which deposition is not immediately required, which can be opened and closed within a fraction of a second, allowing very precise control of layer composition. The substrate is heated from behind, allowing control of the deposition temperature. A liquid nitrogen cooled shield between the sources and the growth chamber provides additional trapping of impurities. Deposited samples can be analysed *in-situ* using Reflection High Energy Electron Diffraction (RHEED) to determine the surface crystallography in real time.

The growth conditions used for deposition of individual samples depends largely on the crystalline structure and material composition desired. The samples measured in this thesis were grown using a very similar procedure to that described by

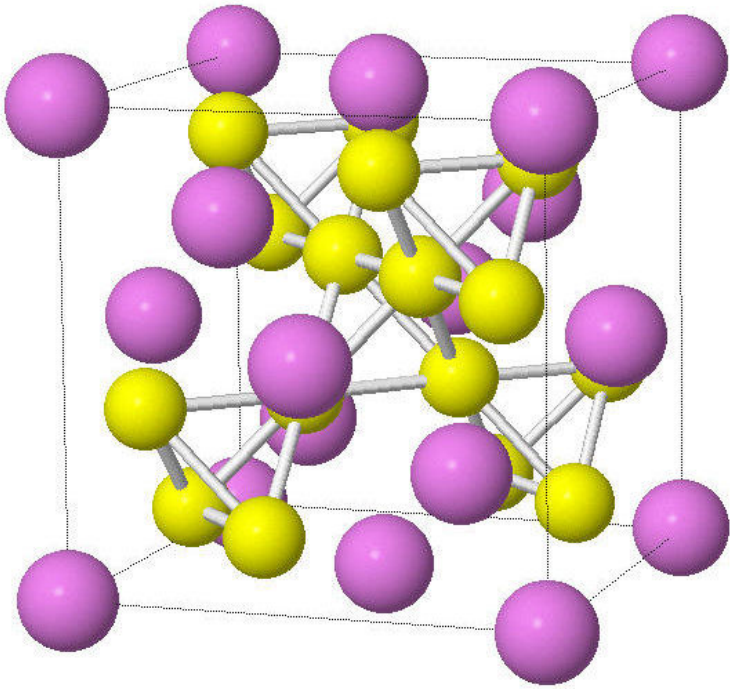

Figure 4.6: The cubic Laves phase structure of the RFe_2 samples deposited by MBE. The pink spheres denote the R (Dy, Er, Y) atoms in the lattice, while the yellow spheres denote the Fe atoms. The R atoms arrange in a face centred cubic diamond structure, with the Fe atoms in a tetrahedral arrangement within the R sub-lattice.

Bentall *et al.*[83]. Deposition is carried out onto a sapphire substrate with a $(11\bar{2}0)$ orientation, with a variable thickness chemical buffer layer of (110) Nb, onto which a thin layer of Fe is deposited to aid improve epitaxial growth. Deposition of the sample is carried out by co-deposition of elemental fluxes at a substrate temperature of 450-750°C, with growth occurring along the [110] direction. The RFe_2 layers grow in a cubic Laves phase structure, as shown in figure 4.6. The R (Dy, Er, Y) atoms form a face centred cubic diamond arrangement, with the Fe atoms in a tetrahedral arrangement inside the R sub-lattice. There is a total of 8 R atoms and 16 Fe atoms per cubic unit cell, and the structure has bulk lattice parameters of 7.324Å, 7.28Å and 7.362Å for $DyFe_2$, $ErFe_2$ and YFe_2 respectively[47].

4.4: Magnetron Sputtering

The sputtering process has been known and used for a number of years. More recently, developments such as the use of magnetrons in the sputtering process and the introduction of 'unbalanced' magnetrons has transformed sputtering into a highly reliable deposition technique which sees a wide range of use in both industry, for producing thin film coatings, and in research for prototyping of thin film samples of a wide range of materials. A review of recent advances in sputtering technology is given by Kelly *et al.*[84]. DC magnetron sputtering has been used to deposit a series of thin films and multilayers which were subsequently investigated using PCAR, the results of which are presented in chapters 5 and 6. A Kurt J. Lesker sputtering rig was used for the deposition of these samples, and the configuration and operation of this system is described here.

The layout of the sputtering rig is shown schematically in figure 4.7. Four magnetron sputter targets allow co-deposition of materials, allowing the creation of alloys and compounds. Two targets operate on the DC principle and are suitable for deposition of metallic, conducting materials, one of which has a stronger magnetic field for deposition of strongly magnetic materials. A further two targets operate at radio frequencies (RF), and are suitable for the deposition of insulators – charge build-up on the cathode (target) is avoided by alternating the applied voltage.

Prior to deposition, the chamber is pumped to a typical pressure of $\sim 1\times10^{-6}$ mbar using a roughing pump followed by a liquid nitrogen cooled cryo-pump. A small flow of Ar gas is leaked into the chamber, typically around 2-5 standard cubic centimetres per minute (sccm). On application of a bias voltage to the target, ions from the discharge plasma in front of the target bombard the surface. This results in removal of atoms from the surface which can then condense onto the sample substrate. In addition, secondary electrons are also generated during ion bombardment. Magnets mounted behind the target generate a field that confines secondary electrons in the vicinity of the target, resulting in a much higher rate of electron-Ar atom collision and a more dense plasma of Ar ions. This in turn increases the rate of sputtering from the target and the deposition rate at the substrate.

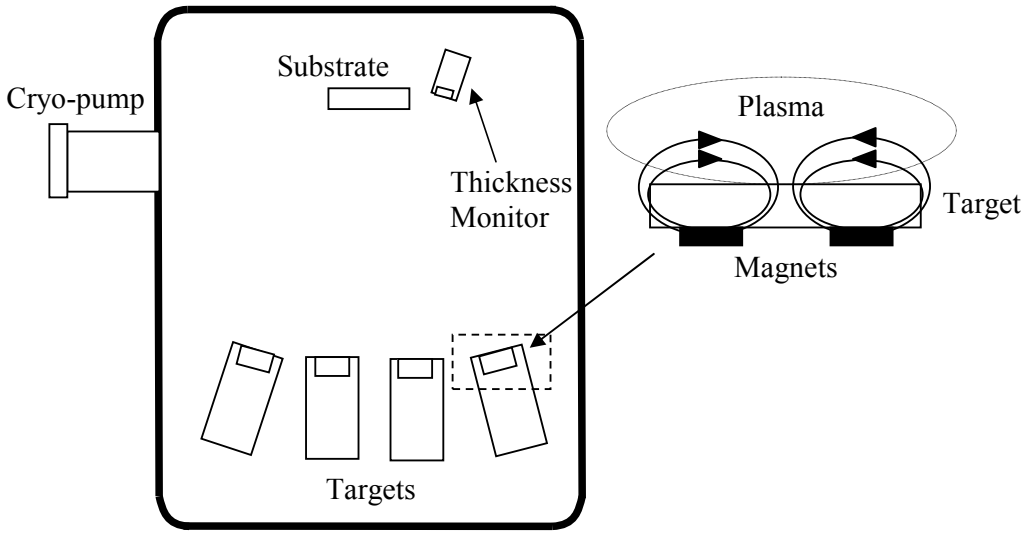

Figure 4.7: Schematic diagram of the sputtered deposition system used. Magnets mounted behind the targets allow a denser plasma to be created, increasing the rate material is sputtered from the targets.

The rate of deposition is monitored using a film thickness monitor mounted near the sample substrate, which must be calibrated for the deposition rates of individual targets. The substrate is rotated to improve the uniformity of film deposition. If required, the substrate may be heated using four lamps mounted around the substrate, and a liquid nitrogen stage may be used for sample cooling.

Chapter 5: Point Contact Andreev Reflection in Transition Metals

This chapter details point contact experiments demonstrating Andreev reflection in superconductor/normal metal (SC/N) junctions. It will be demonstrated that Andreev reflection can be suppressed by an imbalance in electron spin populations at the Fermi level in ferromagnetic materials (FM). Through measurement of the suppressed Andreev reflection in SC/FM junctions it is possible to determine the degree of spin polarisation exhibited by the material. In chapter 3 it was shown that the degree of spin polarisation of the material can be determined by fitting the point contact Andreev reflection (PCAR) data to a model of ballistic transport through a SC/FM point contact. The spin polarisation determined via this method is the ballistic transport spin polarisation P_C, weighted by the Fermi velocity in each spin sub-channel. In this chapter measurements are presented that show additional features at high bias voltages that are inconsistent with standard models of Andreev reflection, and a discussion is made of the origins of these features.

5.1: PCAR in a Cu Film

Current-voltage (I-V) and differential conductance (dI/dV-V) curves were obtained for a range of ferromagnetic and non-magnetic materials. In order to provide a basis for Andreev reflection results presented here, resistance and differential conductance curves were first obtained for Cu. Cu is non-magnetic and hence the full Andreev reflection effect should be observed at zero bias. A sample of Cu was deposited onto a glass substrate by DC sputtering using a Kurt J Lesker sputtering chamber at 5sccm (standard cubic centimetres per minute) argon gas flow, under an initial chamber pressure of 1.6×10^{-6}mbar. The sample thickness obtained was 300nm, after 1 hour of sputtering at 150W. Point contact tips were fabricated from commercially available Nb wire of 1mm diameter, using mechanical polishing by increasingly fine degrees of sandpaper to produce a sharp point. In order to facilitate ballistic conduction from the tip to the surface, a contact diameter smaller than the mean free path in the material is required[55]. Scanning electron micrograph (SEM) images of the tip, in figure 5.1, show that the tip is ~10μm in diameter. However, higher magnification images reveal a large number of small protrusions on the extremity of the tip, and it is believed that these provide numerous ballistic conduction channels, where at first it would appear that the transport should be predominantly diffusive due to the large radius of the tip.

A typical I-V and dI/dV-V curve for Cu at a temperature of 4.2K are shown in figure 5.2. At first sight the I-V curve appears to be a simple straight line. However, on magnification of the centre region around zero bias, a bending of the curve towards a lower resistance can be seen. This effect is more noticeable in the differential conductance dI/dV (G), measured independently by lock-in detection of a 2kHz voltage signal passed across the Wheatstone bridge (See chapter 4). The conductance is normalised relative to the normal state resistance, approximated to the resistance of the point contact at energies $eV>>\Delta$ where superconductivity can be considered to have completely broken down. This resistance value is taken from the gradient of the I-V curve. The differential conductance (G) is obtained as a voltage signal from the lock-in amplifier. This may then be converted to Ω^{-1}, using a conversion factor determined by varying the balancing resistance R_x with a fixed sample resistance and

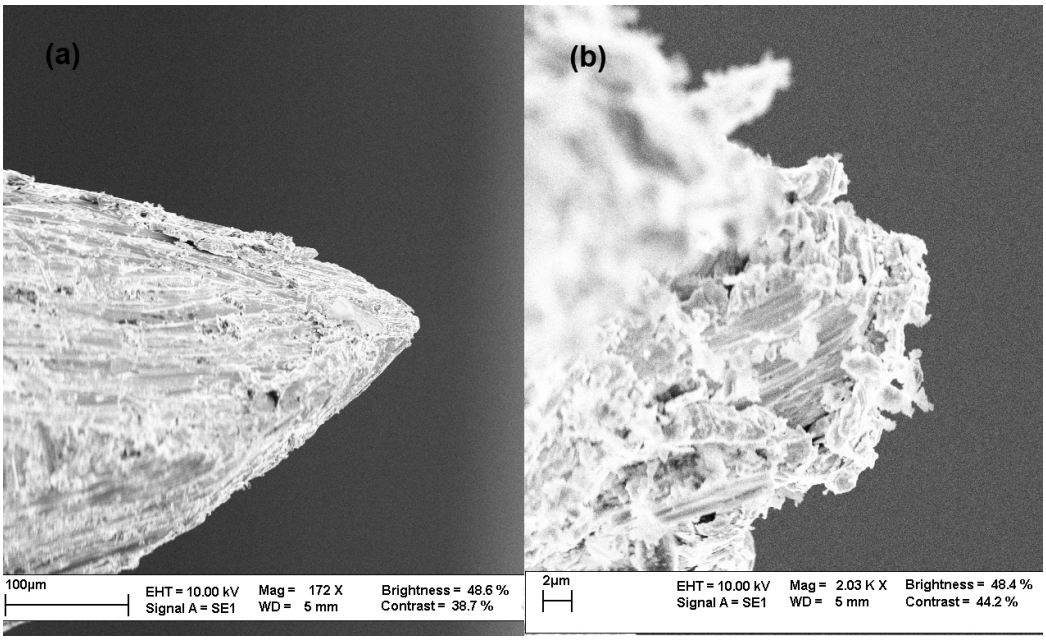

Figure 5.1: SEM micrograph showing a mechanically polished Nb wire. (a) 172x magnification shows tip of ~10µm across. (b) increased magnification of 2030x shows that the tip actually comprises multiple protrusions ~1µm across.

recording the variation in $G(V)$. The normalised differential conductance $G(V)/G_n$ may be written

$$\frac{G(V)}{G_n} = \left(1 + \frac{V}{\alpha R_n}\right)^{-1} \qquad [5.1]$$

Where α = 28.59µV/Ω is a constant converting the lock-in voltage into resistance in ohms and R_n is the normal state resistance of the contact. This formula was derived in section 4.1. Applying this formula to experimental data results in a normalised $G(V)/G_n$ where the conductance is expressed as a numerical factor of the normal state conductance. This allows straightforward comparison with Andreev reflection theory.

Upon normalisation it can be seen from figure 5.2 that the conductance at zero bias of the point contact has increased by approximately a factor of 1.9 from the normal state. This behaviour is in line with expectations from Andreev theory – which

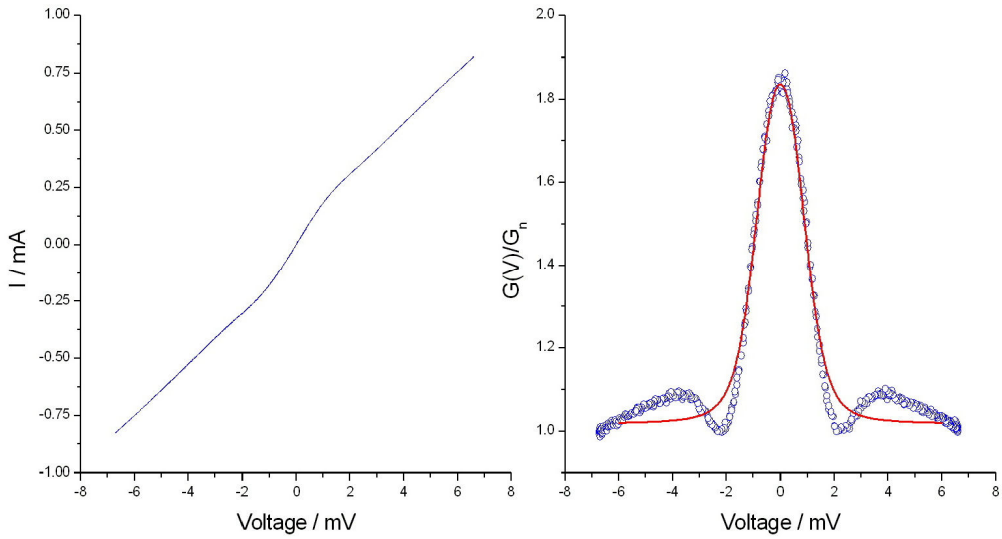

Figure 5.2: Normalised I-V and differential conductance curve for sputtered Cu on glass, showing experimental (blue circles) and fitted (red line) curves.

reveals that one should expect a doubling of conductance, due to the creation of a parallel hole conductance channel. In Cu the Andreev reflection would be expected to be at a maximum, given that Cu is a non-magnetic metal with zero spin polarisation. This expectation is upheld by the data shown in figure 5.2. Dips in the conductance are observed at approximately ±2mV, slightly higher than the superconducting gap Δ=1.5meV in bulk Nb. These features at the interface between superconducting Andreev reflection behaviour and normal junction behaviour can be attributed to the proximity effect[85]. The proximity effect is a well known superconducting effect in which Cooper pairs from a superconductor can diffuse into a metal in close proximity, thereby creating a layer at the metal surface which is weakly superconducting. This proximity layer has a lower superconducting gap Δ and a lower transition temperature than in the bulk.

Previous authors have incorporated this effect into their analysis by considering a two-gap model, in which there are two superconducting gaps Δ_1 and Δ_2, corresponding to the proximity layer and the tip respectively[65]. Theoretical curves show that this modification to the BTK theory produces dips at voltages close to the superconducting gap energy of the superconductor.

In order to accurately determine the spin polarisation, and to confirm that the behaviour observed matches the modified BTK model of Mazin *et al.*[64], least squares fitting of the data using the theoretical expressions of chapter 3 was carried out, using the MATLAB software suite. The resulting fitted curve can be seen in figure 5.2 (red line), the 3 free parameters used in the fitting are Δ, Z and P, with the temperature T fixed at 4.2K. The spin polarisation, P, as expected, was found to be $7\text{x}10^{-10}$, effectively zero. Z is also very small, indicating that there is very little interfacial scattering effect for this measurement. The value of Δ we would expect to be close to 1.5meV, the superconducting gap of bulk Nb, however the fitting gives this parameter as 0.767meV. Reasons for this disparity could include the effect of using a confined tip geometry, reducing the value of superconducting band gap from the bulk value. Also, our fitting has not taken into account the spreading resistance of the film, R_S, that is the resistance between the contact point and the electrical contacts on the film.

Work by previous authors on the relationship between Δ and R_S shows that there is a clear interdependence of the two parameters, and that they produce similar effects on the $G(V)$ curve[79]. Therefore if R_S is appreciable, a large reduction in the extracted value of Δ could be observed. However, as the sample material is Cu, which has a very high conductivity, we would expect the spreading resistance to be very low. This hypothesis is supported by rudimentary measurements carried out by pressing the Nb tip fully into the sample surface, thus eliminating any resistance due to the point contact, and in principle measuring only the resistance of the film. These measurements give an approximate value for the spreading resistance of below 0.01Ω, well below a typical total resistance of 5-10Ω, suggesting that R_S is largely unimportant in the analysis of this Nb-Cu point contact.

We must therefore look elsewhere for an explanation for the low value of Δ. As noted above, the dips in the conductance spectra indicate that there is a sizable proximity effect occurring at the interface between the Nb tip and the Cu film, and this can produce a second effective superconducting gap in the system, corresponding to the proximity layer. Therefore, the gap value extracted from the fitting procedure may in fact be the reduced proximity layer value Δ_1, and this is supported by the value being roughly half of the bulk value as observed by previous authors[65]. As can be seen

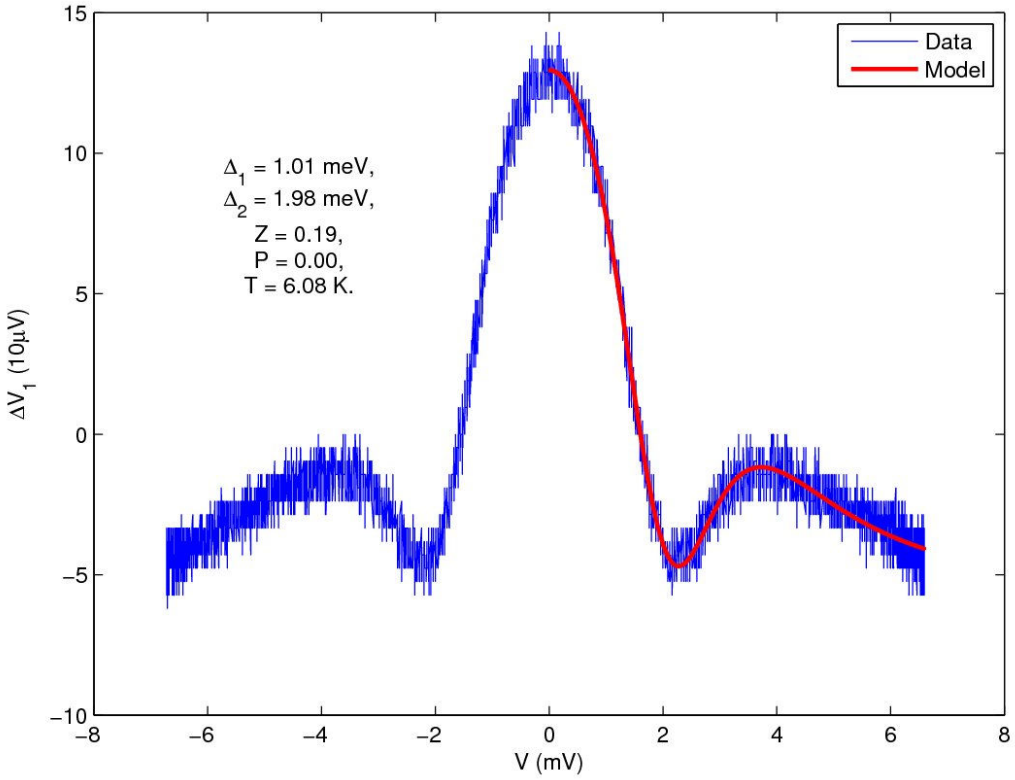

Figure 5.3: Two gap model fitting of Nb tip to Cu film experimental data. 5 free parameters were used, these are indicated within the figure (Δ_1, Δ_2, Z, P and T).

from an examination of figure 5.2, while the fitting procedure reproduces the main Andreev reflection peak accurately, the fitting breaks down as the voltage approaches voltages near to the energy of the superconducting gap. As mentioned earlier this can be explained via the proximity effect. To this end, a two gap model was used to fit the experimental data, with 5 free parameters (Δ_1, Δ_2, *Z*, *P* and *T*). As can be seen in figure 5.3 this theory produces a very good fit to the experimental data, accurately accounting for the observed dips at ±2mV. Thus it is likely that these dips are due to the proximity effect, that is a diffusion of Cooper pairs into the Cu near to the Nb tip, an effect that is not included in the original BTK model of Andreev reflection, nor in the modifications for metals with non-zero spin polarisations. The two gap values Δ_1 and Δ_2 are larger than the single gap extracted from the previous fitting in figure 5.2, which seems erroneous. However note that the temperature has also been extracted from the fitting procedure as 6K – this value is higher than the experimentally measured local temperature of 4.2K. This may account for why the gap values

obtained are larger than expected, as an increase in temperature will broaden the curve, moving the dips to higher bias values. Thus, when the curve is fitted using the modified two gap model, the extracted parameters Δ_1 and Δ_2 will be increased, as they represent the position of the coherence peak and the dip minimum, respectively.

5.2: PCAR in a Co Film

Although Cu provides a clear demonstration of the full unsuppressed Andreev reflection process, it is an uninteresting system in that we can only expect zero spin polarisation from Cu as the band structure is symmetrical in electron spin. From the perspective of this thesis magnetic materials are more interesting, in that spin-related phenomena can be observed. To provide a basis for measurements on MBE-grown RFe_2 materials, 300nm thick samples were prepared of Co by DC sputtering at 60W, using a gas pressure of 5sccm with an initial chamber pressure of 1.2×10^{-6}mbar, onto a Si substrate. Again, a Nb tip was used, mechanically polished to a fine point as described above. Co was chosen since the material provides a well known spin polarisation value of 42 ± 2%[62] (Soulen Jr. *et. al*) and 45±2% (Strijkers *et al.*)[65].

Figure 5.4 shows typical $G(V)$-V curves for sputter deposited Co on a glass substrate. Again the I-V curve (not shown) is distorted towards lower resistance at low bias voltages, an enhancement of the conductance due to Andreev reflection. Examining the differential conductance curves reveals a definite enhancement of zero bias conductance from the normal state behaviour. This enhancement is suppressed from full Andreev reflection behaviour, giving zero bias $G(V)/G_n$ values of 1.05 to 1.15, dependent on the individual contact made, distinguished here by their resistances obtained from the I-V measurements. At different tip heights, different resistances are obtained, corresponding to varying contact areas.

In the low bias region (>5mV) the behaviour is as expected for Andreev reflection, with a sharp increase in conductance, that drops off sharply with increasing voltage. For curves (b)-(d) a decrease in conductance is observed at zero bias, this is due to interfacial scattering, as characterised by the Z parameter. The effects of non-

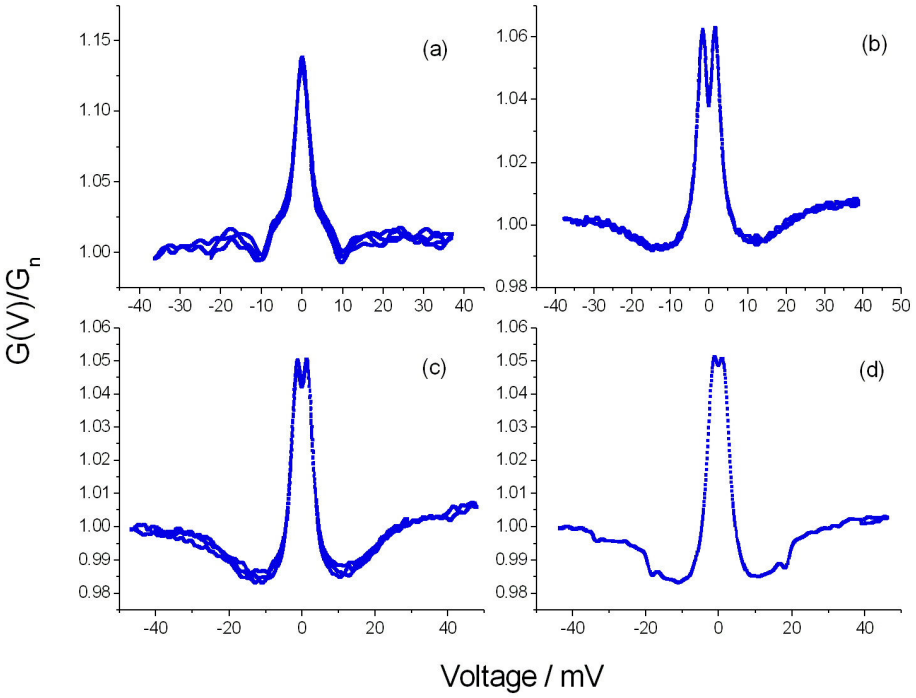

Figure 5.4: Differential conductance curves as a function of voltage for four point contacts of Nb to Co at 4.2K. The resistance values of the contacts are (a) 2 ohms (b) 10 ohms (c) 13 ohms (d) 15 ohms.

zero *Z* were shown in figure 3.5, a suppression of zero bias conductance that results in a two peak structure, with peaks at ±Δ. The behaviour in the low bias region can be considered as purely Andreev-like and is well described by the modified BTK model of Mazin *et al.*. Outside this region, many features can no longer be attributed to Andreev reflection, and must be considering separately.

In figure 5.4 large dip features can be seen from ±10-20mV, varying from a sharp dip at 10mV in the low resistance case to a broad feature spanning 10mV in the higher resistance cases. At first sight it might seem sensible to attribute these features to the proximity effect, as seen in Cu. However, the dips are broadened and appear at higher bias voltages than would be expected for the proximity effect, where the dips typically occur near the superconducting gap Δ of the tip. Additionally, due to the strong pair-breaking nature of ferromagnetic materials such as Co, it is unlikely that a

proximity superconducting layer could form at the surface of the metal. Previous authors have attributed these large dip effects to a critical current effect in the superconductor[86]. As the current flowing through the contact reaches a certain value I_c the voltage across the contact begins to rise rapidly, resulting in a sharp dip in the differential conductance $G(V)$. As the current increases past this region of rapid change, the voltage increases at a slower rate, and the value of $G(V)$ stabilises at the normal state value. This is illustrated in figure 5.5. The mechanism behind this effect in a type-II superconductor such as Nb is vortex motion, induced by the Lorentz force. The Nb tip is in a state of vortex flux penetration, due to the self (Oersted) field of the applied current. These vortices will be pinned due to defects and impurities within the superconductor. Once the Lorentz force due to the applied current and the Oersted field becomes sufficiently large to overcome the vortex pinning force, vortex motion will occur. This motion results in dissipation of the current flow, and a rapid onset of resistance is observed.

This critical current effect could explain the dips observed in the Nb-Co spectra, however the features are wider than those reported in reference [86], a potential explanation for which is discussed below. The current density for these dips can be estimated by calculating the contact radius using the Sharvin formula for the resistance of a ballistic point contact (section 3.1). Taking the example of figure 5.5 (4×10^8A/cm^2), the critical current density agrees quite well with the estimates of Sheet *et al.*, who estimated the critical current density in their Au/Ta point contact as 3.6×10^8A/cm^2. The superconducting behaviour of Nb can be expected to vary from that of Ta, and hence this value should only be used as an order-of-magnitude comparison.

Previous authors have discussed the effect of the finite lifetime of quasi-particles in the superconductor/metal system as a possible explanation of the broadening of these features at higher bias voltages[87]. They considered that there may be inelastic scattering due to degradation of the surface layer near the superconductor to normal metal interface, and that this would result in a shortening of quasi-particle lifetimes near the surface. This manifests itself as a broadening of the dips observed in $G(V)/G_n$ characteristics. This could therefore account for the effects seen in figure

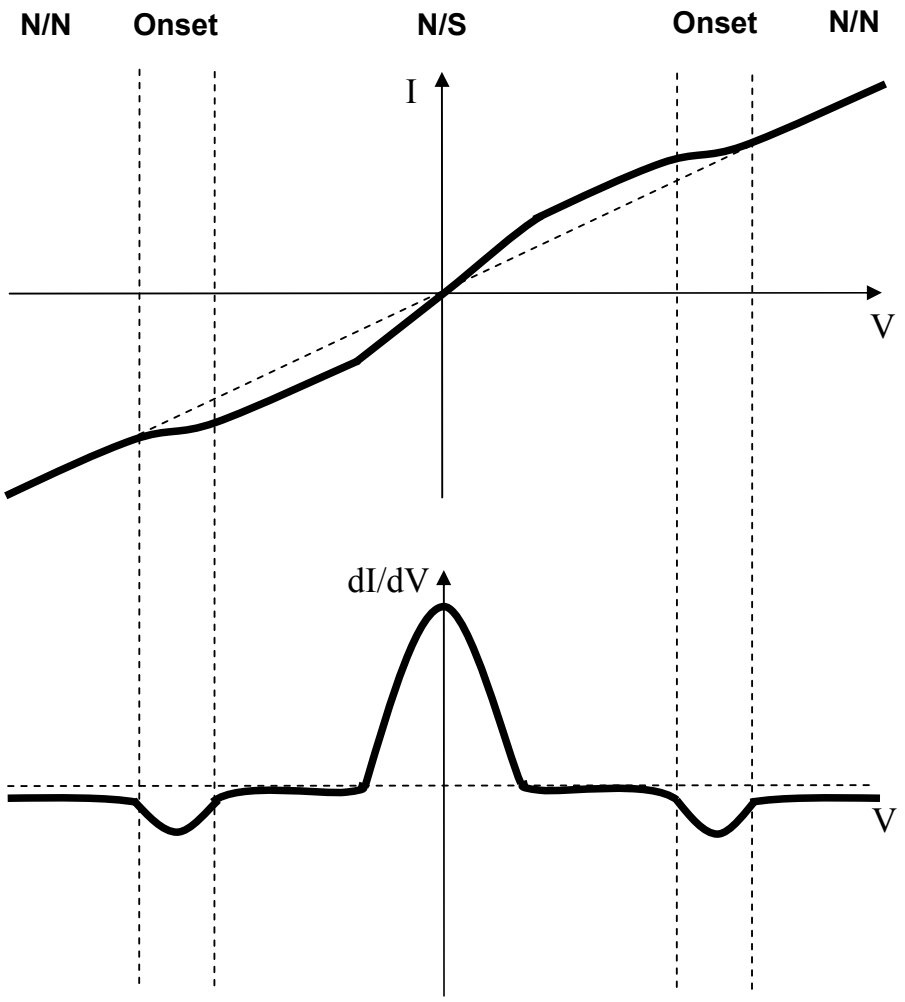

Figure 5.5: Schematic I-V and dI/dV-V curves showing the onset of normal state behaviour in the superconductor-side of the junction. As the current approaches the region marked 'Onset', a voltage drop starts to occur across the superconductor, resulting in increased resistance and a dip in the differential conductance.

5.4, where the dips have become much wider (~10mV). Indeed, this effect might be expected to become more pronounced for larger resistance contacts, given the potential for increased scattering of the conduction electrons and associated quasi-particles.

In order to obtain the experimental parameters, in particular the contact spin polarisation P_C, least squares fitting of the Mazin *et al.* modified BTK model was

made to the experimental data, of which typical curves are shown in figure 5.4. The resultant fit for figure 5.4 (a) is shown in figure 5.6, superimposed on the experimental curve. Again, clear agreement can be seen between the model and experiment, provided one only considers low bias voltages (>10mV). Outside this region the fit becomes poor, but we note that this is to be expected, because as discussed earlier only the low bias data is attributable to Andreev reflection, providing a good fit to the modified BTK theory. Additional features are discussed above in a qualitative fashion, but require further theoretical treatment beyond the scope of this thesis. The three extracted free parameters (Δ, Z and P) are 1.346meV, $4x10^{-6}$ and 0.441 respectively. The parameter Z is again found to be essentially zero, indicating that very little interfacial scattering is present in the experiment. Indeed this can be seen from the curve as the dip at zero bias, characteristic of high Z, is not present. Δ extracted from this fitting deviates slightly from that of bulk Nb (1.5meV), this might be expected as the Nb tip has rounded conical shape geometry and has dimensions of less than 1μm, therefore the tip is unlikely to behave as bulk Nb. The wire used to fabricate the Nb tips used here is cold-worked and is likely to contain a large number of defects, and in addition strong plastic deformation of the tip when contact is made can also change the properties of the superconductor. There is found to be little dependence of P_C on the interfacial scattering parameter Z on analysis of the remaining curves, and therefore we quote the spin polarisation P_C of this Co film as 44±2%, close to the values obtained by previous authors, quoted earlier as 42±2% (Soulen *et al.*)[62] and 45±2% (Strijkers *et al.*)[65].

5.3: PCAR in Fe Films

Iron films have been studied extensively using PCAR techniques in the past[62,65]. Here PCAR measurements of Fe films deposited using two techniques (Molecular Beam Epitaxy (MBE) and DC Sputtering) are presented, allowing a direct comparison of the effects of sample crystallography on these point contact measurements. Soulen Jr *et al.* reported measurements of single-crystal Fe thin films and also measurements in which the junction geometry was reversed, using a Fe tip to contact to a Ta foil, in which they found that the extracted P_C value varied slightly

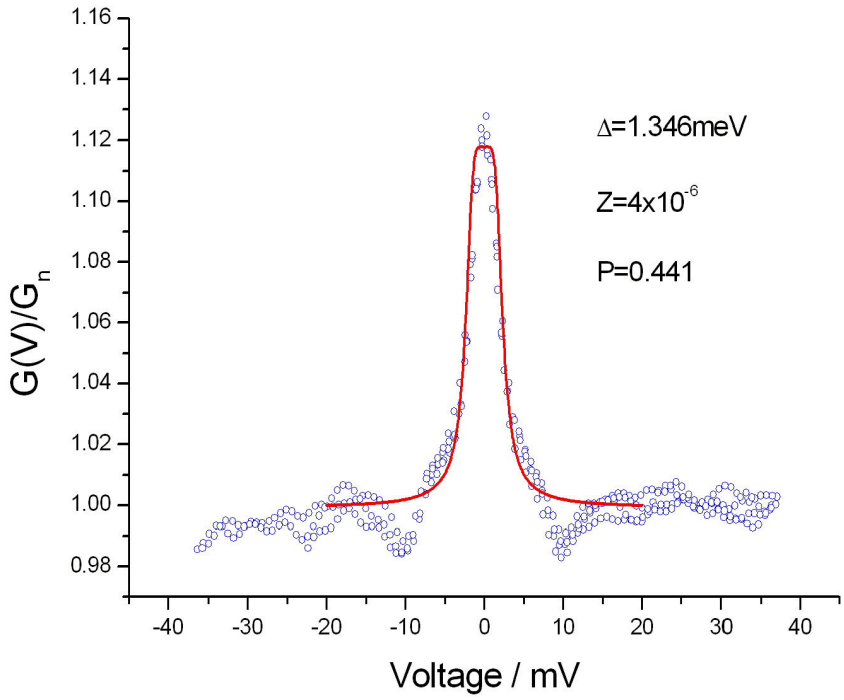

Figure 5.5: Fitted data (red line) superimposed on experimental curve (blue circles) from figure 5.4 (a) for a Nb to Co point contact. Free parameters extracted from the fitting (Δ, Z and P) are indicated on the plot.

between the two geometries[62]. Strijkers *et al.* reported measurements on Fe films produced by magnetron sputtering, in which they found P_C to again vary by several percent from previously reported values[65]. There would appear to be a dependence of PCAR on the particular sample studied, and it is this point that we intend to examine in more detail. The PCAR behaviour of Fe is particularly important for the results that follow, as it has been found that the spin polarisation of Laves phase RFe_2 compounds closely resembles that of Fe.

PCAR measurements were carried out using a mechanical point contact technique (described in chapter 4), using a mechanically polished Nb tip pressed into an Fe film. The 800nm thick Fe film was deposited using DC magnetron sputtering at a power of 100W with a base pressure of 1.6×10^{-6}mbar, using an Ar gas flow rate of 2 sccm. Example PCAR curves resulting from making contacts at varying contact

resistances corresponding to varying pressure of the tip on the surface are shown in figure 5.7, taken at a temperature of 5K. In all the curves obtained from contacts to this sputter-deposited Fe film a reduction in zero bias conductance was found, rising to a peak at approximately ±6mV, before falling back to the normal state value. In the low resistance case a shallow trough is observed from ±10-30mV, however in the higher resistance case relatively sharp dips are observed at approximately ±20mV. The behaviour at low bias (<10mV) appears to be consistent with the modified BTK model, and is suggestive of either P_C larger than 50%, a large value of the interfacial scattering parameter Z, or a combination of both variables. As in section 5.1.2, it is likely that the dips at high bias can be attributed to switching of the Nb tip from a superconducting to normal state, at a current value corresponding to the critical current of the tip. The broadening of these features at high junction resistances can potentially be attributed to increased scattering at the interface due to the high resistance, resulting in a reduction of the lifetime of quasi-particles at the interface and an associated smearing of the features. This effect was also discussed in section 5.1.2.

For the purposes of comparison, a 100nm film of Fe was deposited via MBE onto a sapphire substrate with a 50Å Nb layer and a 20Å Fe seed layer. Typical PCAR curves showing the differential conductance of the Nb tip to Fe film contact at a temperature of 4.2K are shown in figure 5.8. A clear enhancement of conductance at zero bias is visible, corresponding to a spin polarisation of less than 50%. The two peaks visible at approximately ±2mV in figures (a)-(c) are suggestive of a large degree of interfacial scattering. In all differential conductance curves obtained for this sample, broad dip features are observed at high bias values, from ~±10-30mV. Fitting of two example data curves (from figures 5.7 and 5.8) to the modified BTK model of Mazin *et al.*[64] is shown in figure 5.9, using three free parameters Δ, Z and P. The model provides a good fit to the data obtained from the MBE-grown film; the superconducting gap parameter Δ is extracted as 1.48meV, very close to the bulk value for Nb from BCS theory. The spin polarisation P_C is found to be 43%, almost exactly the value expected from the work of previous authors (Strijkers *et al.*[65], Soulen Jr. *et al.*[62]). From fitting of the remaining curves, it P_C is found to vary between 41% and 46%, with varying Z parameters. There is no clear dependence on Z, and we take a mean value for $P_C = 43 \pm 3\%$.

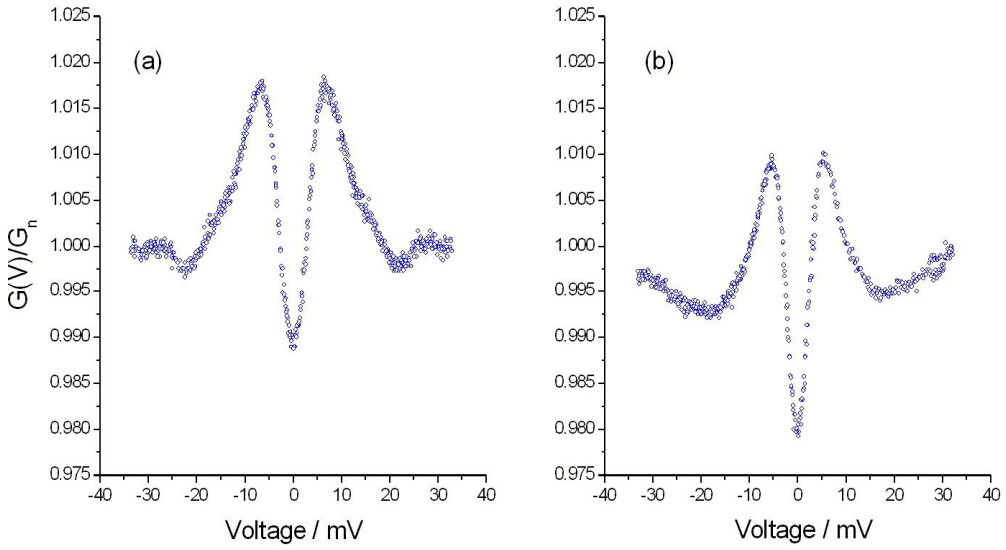

Figure 5.7: Typical differential conductance plots for contacts of Nb to sputter-deposited Fe at a temperature of 5K. Contact resistances are (a) 32 ohms (b) 20 ohms.

The model appears to give a very poor fit to the data obtained from the sputter-grown film. The reason for this is not immediately clear, however it would appear that the least squares fitting procedure used is unable to accurately fit data in which the normalised zero bias conductance is close to 1. If we assume that Z is low, which may be valid considering previous data in which high resistance curves have revealed very little interfacial scattering upon fitting, P_C may be estimated as approximately 51%.

Due to the value of spin polarisation in the sputter-deposited film being a very rough estimate, it is difficult to say anything conclusive about the relation between sample crystallography and sample spin polarisation in these Fe films. It would however appear that the spin polarisation in the MBE-grown film more closely resembles that observed by previous authors, close to 43%. The spin polarisation observed in the sputter-deposited film is potentially higher, however it is also possible that the film quality is poorer, resulting in increased interfacial scattering. Because we have used the zero-bias conductance as an estimate of the spin polarisation, if Z is significantly high this will result in our estimate being rather poor. This could allow the spin polarisation to be close to 43%, indicating very little effect of sample preparation on the spin-dependent properties of the film, with P_C being very similar in

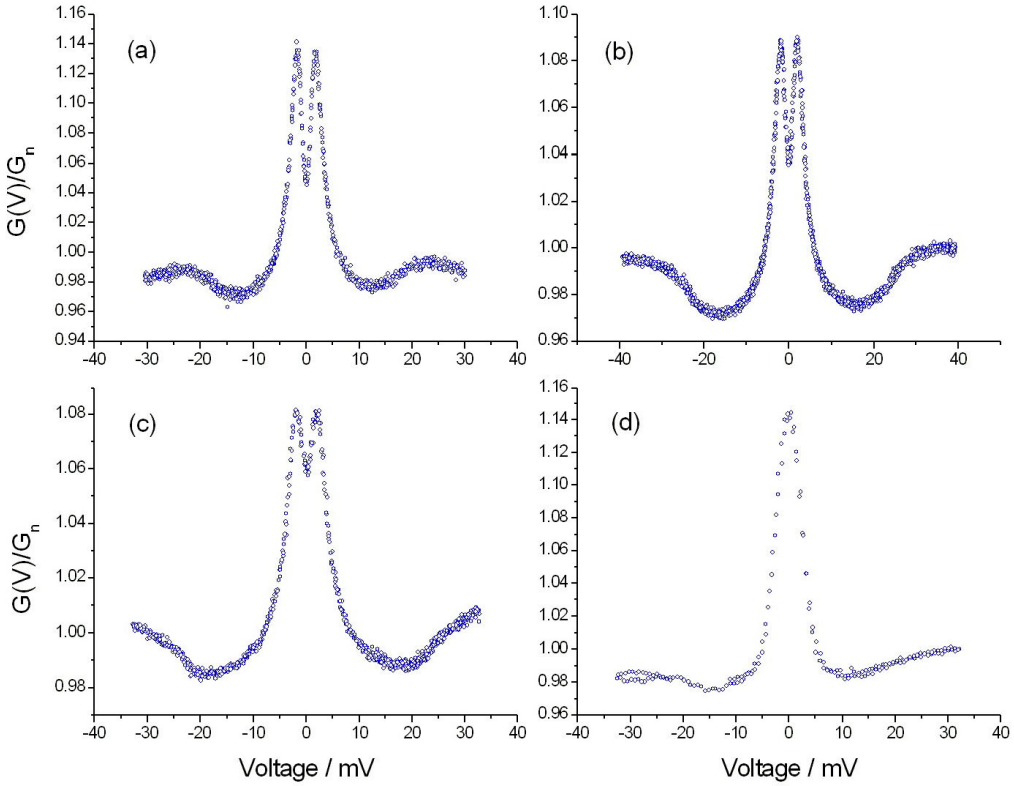

Figure 5.8: Differential conductance curves for contacts of Nb to a 100nm MBE-deposited Fe film. Total contact resistances are (a) 7 ohms (b) 13 ohms (c) 17 ohms (d) 22 ohms.

both the MBE and sputter deposited films.

Typically the spreading resistance R_S, which is the additional resistance in the measurement due to the resistance of the film between the contacts and the tip, is assumed to be small in the measurements presented here. It is therefore neglected from the analysis. But how large is R_S, and could it indeed be an important factor? Woods *et al.* measured the spreading resistance in two high resistivity films, LaSrMnO (LSMO) with a resistivity of 500$\mu\Omega$cm and CrO_2 with a resistivity of 20$\mu\Omega$cm, finding spreading resistances of 10Ω and 0.75Ω respectively. By comparison, we might expect the spreading resistance to be typically less than 0.1Ω in the films measured here, where the resistivity is of the order of 5-6$\mu\Omega$cm at 4.2K. To test this hypothesis, an estimate of the spreading resistance in a sputter-grown Fe film was made, by pressing

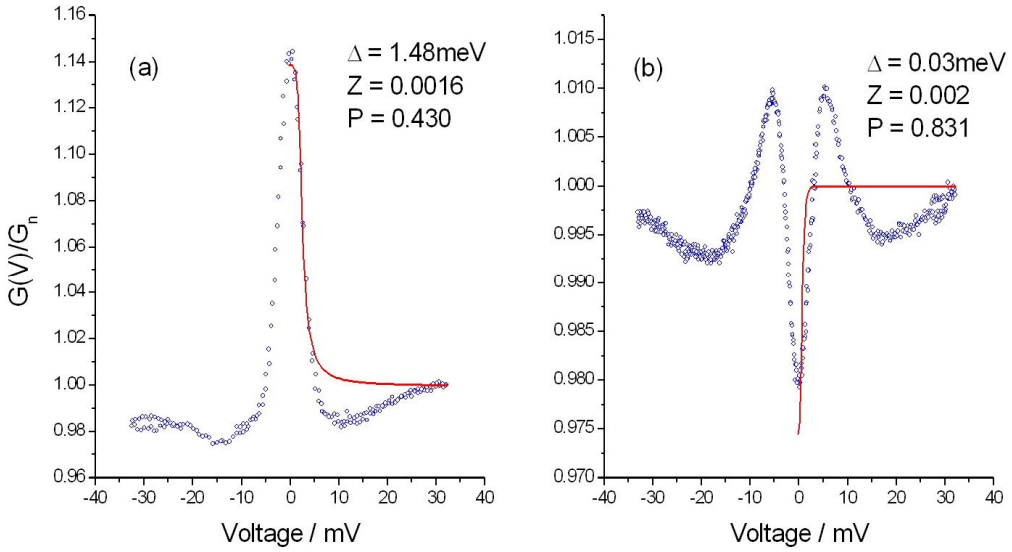

Figure 5.9: Examples of fitting of experimental data for (a) MBE-deposited and (b) sputter-deposited Fe films, to the modified BTK model of Mazin et al. Extracted values for the three free parameters Δ, Z and P are indicated in the figure.

the tip fully into the surface, until the resistance change with additional compression became small. An I-V measurement made in this configuration gave a resistance value of 0.06Ω. This can be taken as an upper bound for the actual spreading resistance of the film – we assume that all of the resistance due to the tip contacting to the film has been removed, but this may not fully be the case. It would appear that assuming that R_S is negligible is a valid approximation.

Chapter 6: Point Contact Andreev Reflection in Transition Metal Bi-layers

In this chapter PCAR measurements of a number of bi-layer and multilayer films are presented. Co/Y bi-layers are investigated as a model system to explore the effect of an Y cap on the measurement of the spin polarisation of an under-layer of ferromagnetic material. This is of particular applicability to the measurements presented in chapter 7, where Molecular Beam Epitaxy (MBE) grown Laves phase RFe_2 films are explored using PCAR. These films are typically capped with 5-10nm of Y to prevent oxidisation, and therefore consideration must be made of the effect this cap will have on the measurement. As an extension to this work, Co/Cu bi-layers with increasing thickness of Cu are examined, in order to further explore spin diffusion in a non-magnetic spacer layer. Through analysis of these bi-layers, the spin diffusion length in these Cu films is estimated.

6.1: PCAR in Co/Y Bi-layers

The spin polarisation of Co was determined in section 5.1.2, and found to be ~44%, close to values obtained by previous authors using PCAR spectroscopy. With this observation confirmed, the question can be posed: what is the effect of layering Co with a thin non-magnetic layer, such as Y? Y is not ferromagnetic, and should possess no macroscopic spin polarisation – occupation of the spin sub-bands at the Fermi energy should be equal. It is therefore interesting to consider whether it is possible to still detect the magnetic, spin polarised nature of Co through a thin layer of Y metal, and to what extent we can layer Y atop Co before a significant effect on the detected spin polarisation will be measured. It may be expected that this will depend on two main parameters. Firstly, the mean free path of conduction electrons in Y, determining the maximum ballistic penetration depth of the electrons and hence the approximate amount of material the injected electrons will sample. Secondly the spin diffusion length, which is a measure of the distance over which electrons can retain spin information before this is lost to spin-flip processes. Potentially, if the spin diffusion length is large enough, electrons with retained spin information from the Co underlayer will be detected in a PCAR measurement. This will prove especially important in section 5.2, where rare earth-transition metal (RFe_2) compounds are measured via PCAR – these samples are typically capped with a 10nm layer of Y metal to prevent oxidation of the film. It is therefore important to consider to what degree this can be expected to affect the measured spin polarisation in these materials.

Two bi-layer samples were fabricated using sputter deposition from Co and Y targets at a working pressure of 2.9×10^{-3}mbar, under an Ar gas flow rate of 2sccm. Final measured thicknesses (via SEM) were 300nm Co with a capping layer of 10nm and 100nm of Y, respectively. An example differential conductance curve between a Nb tip and the 300nm Co/10nm Y sample surface is shown in figure 6.1 (blue circles), along with the corresponding fitting of the modified BTK model of Mazin *et al.* (red line). The three extracted free parameter values are Δ = 1.02meV, Z = 0.0006 and P = 0.443. The general shape of the curve is very similar to that seen in figure 5.5 for a plain Co film. The superconducting gap parameter is rather low, however this can be attributed to the variation in the superconducting properties of the tip from the bulk,

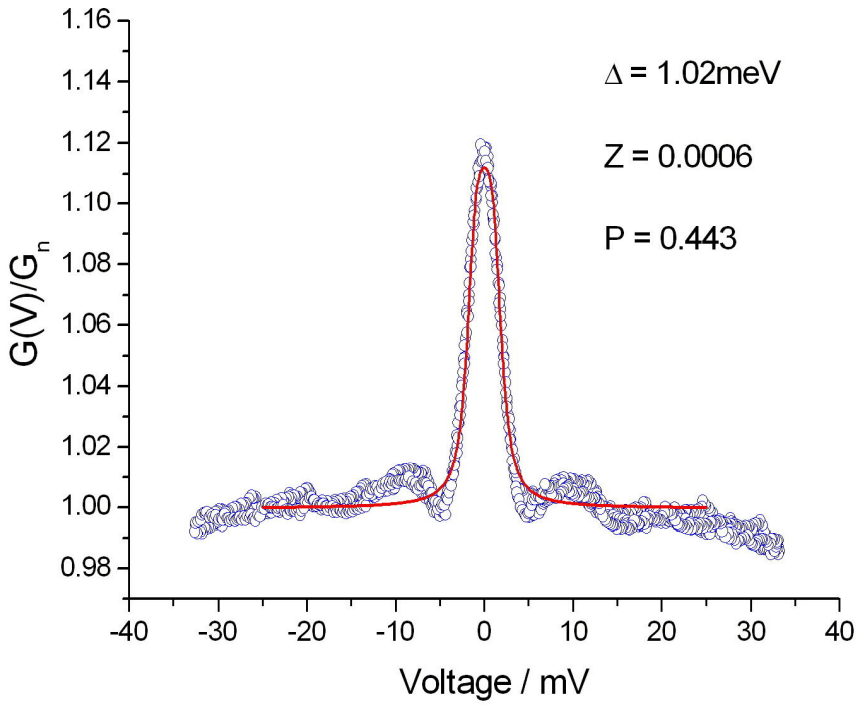

Figure 6.1: Differential conductance curve for a Nb contact to a Co 300nm / Y 10nm bi-layer. Experimental data (blue circles) and modified BTK model fit (red line) are shown, including the three free parameters extracted from the fitting (Δ, Z, P).

due to plastic deformation and a high density of dislocations and defects. Also, the cold-worked Nb wire used to form the tip is expected to have a larger number of defects, contributing to this reduction in the observed gap value[88]. There is found to be little dependence of the extracted value for the spin polarisation on the *Z* parameter upon analysis of the remaining curves, giving $P_C = 44 \pm 3\%$ which agrees well with the value determined for Co in the preceding section.

Example differential conductance curves for contacts of a Nb tip to a Co 300nm / Y 100nm bi-layer are shown in figure 6.2. In total 10 conductance curves were produced, by varying the pressure of the tip on the sample surface to produce a range of contact resistances. The experimental data was fitted to the modified BTK model of Mazin *et. al*[64], the results of which are overlaid on the example curves. The three extracted free parameters are indicated in the figure alongside the curves. The

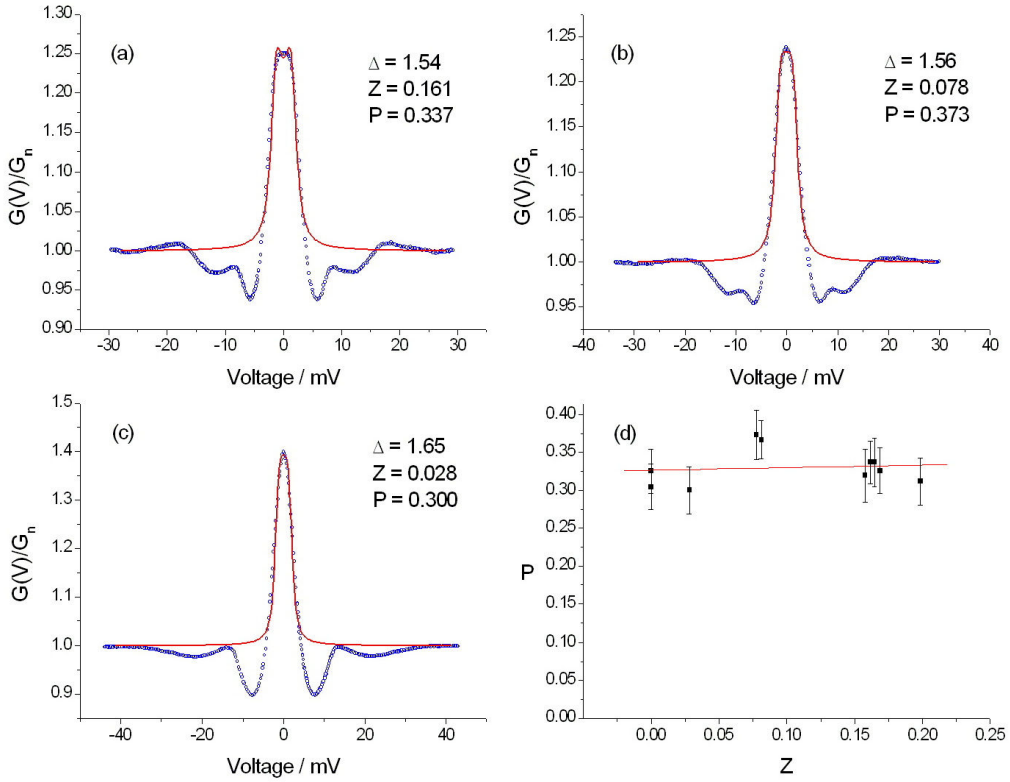

Figure 6.2: (a) – (c): Example differential conductance curves for contacts of a Nb tip to a Co 300nm / Y 100nm bi-layer film, at contact resistances of 35, 44 and 65 ohms respectively. Experimental data (blue circles) and fitting to the modified BTK model (red line) are shown. Panel (d) shows a plot of the extracted P and Z parameters from the fitting, with a linear fit (red line).

superconducting gap parameter Δ was found to vary very little between contacts, from ~1.5-1.7meV. There is no clear dependence of this parameter on either *P* or *Z*. The observed values above the bulk gap for Nb (1.5meV) may be due to thermal broadening; if the measured temperature is lower than the local temperature at the tip due to contact heating effects, then the extracted gap parameter will be found to be higher than the bulk value.

The extracted *P* and *Z* parameters for the 10 measured curves are plotted in figure 6.2 (d). Many previous authors have used a common method of plotting *P* against *Z* and extrapolating to *Z*=0, and taking this value to be the intrinsic spin polarisation of the material, with zero interfacial scattering present[77,89,90]. Applying

this method here we find little dependence of P on Z, and extrapolating to Z=0 allows us to extract a value for the intrinsic P_C = 33±3%. This value is significantly reduced from that extracted above for a bi-layer with 10% of the Y thickness here. This suggests that by layering sufficient Y atop the Co under-layer we have suppressed the spin polarisation of the electrons in the material, through their transit in the un-polarised Y layer. Spin flip scattering processes are likely to be the dominant mechanism here, causing electrons in the material to lose their majority spin population. We can conclude that at a thickness of 10nm an Y cap will have little effect on spin polarisation detection by PCAR of an under-layer, however when the cap is increased to a sufficient thickness then the spin information carried by the electrons is lost to some degree.

6.2: PCAR in Co/Cu Bi-layers

In the previous section, PCAR measurements were made of Co/Y bi-layers, primarily to determine the effect of a relatively thin cap of a non-magnetic material on the spin polarisation measured. One of the questions posed was that of the maximum distance over which spin information can be preserved in the non-magnetic material, before spin-flip processes cause it to be lost. In this section, PCAR measurements of Co/Cu bi-layers are presented. The thickness of the Co under-layer was kept constant at 300nm, while the Cu layer was allowed to vary to 120nm, 300nm, 600nm and 1000nm. From spin diffusion length measurements carried out using a different method on a similar system, we can expect the spin polarisation of the Co to be detectable through a thickness of up to 1000nm of Cu, dependent on the purity of the Cu used[91,92]. The aim of the PCAR measurements presented here is firstly to determine whether it is possible to measure spin propagation through Cu using this technique, and secondly if this is possible, to arrive at an estimate of the spin diffusion length in this system.

The Co/Cu bi-layers used in the measurements presented here were deposited by magnetron sputtering onto a glass substrate. Co was deposited at 60W for 5800s to obtain a 300nm thick film, followed by Cu deposited at 100W for a variable time to

produce the layer thicknesses indicated in the preceding paragraph. Deposition was carried out after pumping to an initial chamber pressure of 9×10^{-6}mbar, under an Ar gas flow of 2sccm. The film thickness was confirmed via SEM, and an example image is shown in figure 6.3. Contrast between the two metals is difficult to achieve as their secondary electron emission is similar under electron irradiation, however a relatively clear interface is visible between the two layers.

Example differential conductance curves for contacts of Nb tips to Co 300nm/Cu 120nm and Co 300nm/Cu 300nm bi-layers are shown in figure 6.4. Approximately 20 measurements were made for each sample, by varying the tip pressure on the surface to create different contact resistances. Out of these, those of very high resistance (>50Ω) were not analysed due to behaviour inconsistent with point contact Andreev reflection. Fitting of the data was made to the modified BTK model of Mazin *et al.*[64], described in detail in chapter 3, and the resulting curves are presented in figure 6.4 (red lines) alongside the data. The three free parameters extracted from the fitting procedure (Δ, Z, P) are inset in the figure. The superconducting gap Δ was found to typically be slightly larger than the bulk gap value for Nb of 1.5meV. The mechanism behind this is unclear – however, if the experimentally measured temperature were inaccurate, the curve would be broader than expected, thus moving the coherence peaks to higher bias voltages. This would result in a value for Δ that is larger than the bulk value. We therefore suggest that the local temperature at the sample surface may be higher than the measured temperature, due to heating at the contact between the Nb tip and the surface. Contact heating has an additional effect on the curves, they are no longer entirely flat at high bias voltages, with a quadratic decrease in conductance arising from these heating effects ($P \alpha V^2$). This effect becomes more prominent at high resistances, as the contact area becomes smaller and the current density increases, resulting in increased heating effects.

The degree of interfacial scattering present, characterised by the Z parameter, is dependent on the curve being considered, and appears to be inversely proportional to the total contact resistance. The Z parameter varies between 0.431 and 2×10^{-4}, and also seems to be inversely proportional to P. As mentioned in the preceeding section, previous authors have used a method of plotting P against Z in order to

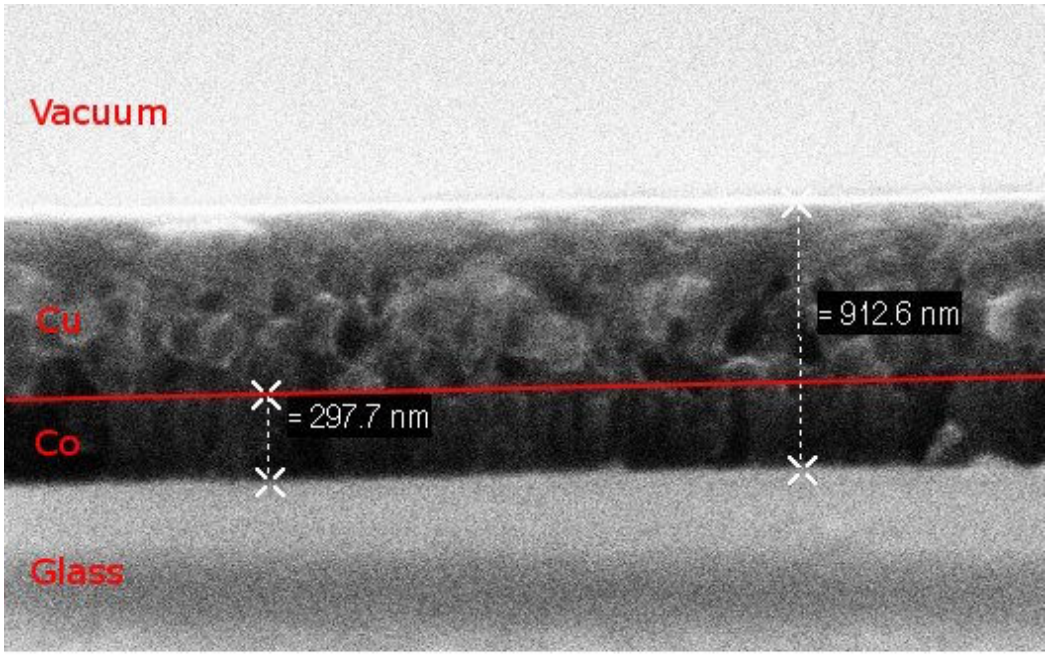

Figure 6.3: Scanning electron microscope (SEM) image using 15keV electrons at 17,000x magnification, showing the cross-section of a Co/Cu bi-layer on a glass substrate. Red line indicates the approximate interface between the two metals.

extract the intrinsic spin polarisation of the material. Within the BTK model there is no physical reason for P to depend on the interfacial scattering parameter Z, as P is an intrinsic property of the material in question. However, it is worth noting that in order to normalise experimental PCAR spectra, the normal state resistance must be used. Moreover, from the work of BTK it can be seen that the normal state resistance R_N does indeed have a $(1+Z^2)$ dependence[63]. Therefore if the contact has a high Z value then the normalised peak will be abnormally large, due to the lowered normal state conductance. Thus a dependence of P on Z can be expected. Woods *et al.* observed a strong Z dependence of P_C in PCAR spectra of Sn to CrO_2[79], even despite efforts to control all parameters in their fitting process. They concluded that in general, if $Z<0.5$, then the data may be considered ballistic and fitting a P against Z curve is valid.

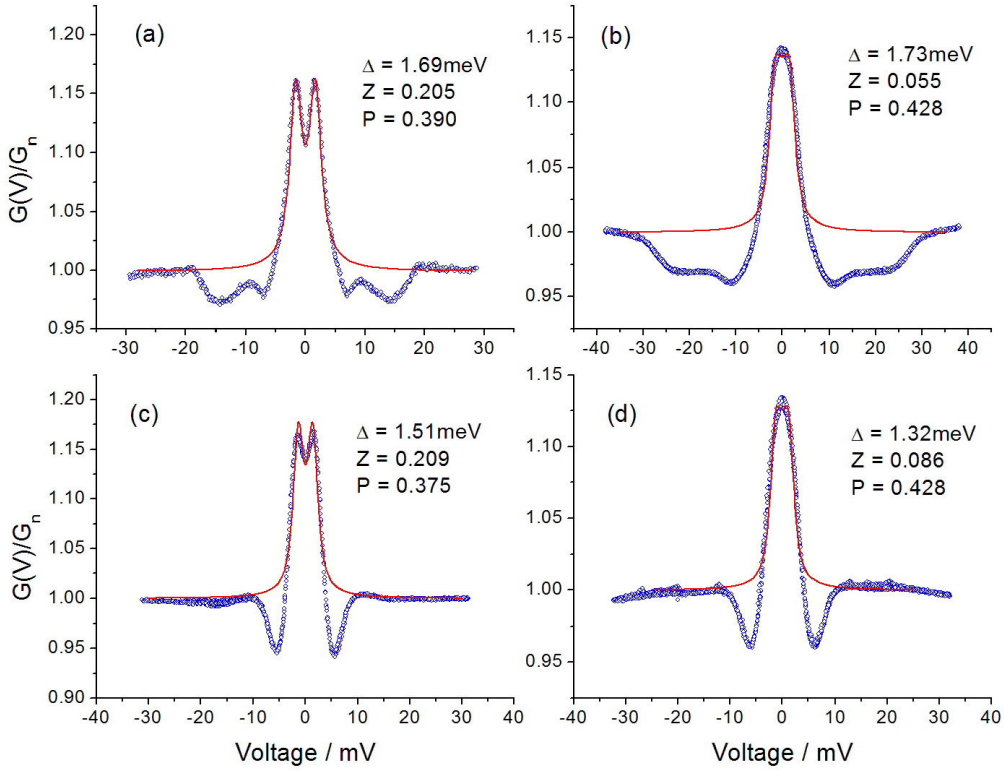

Figure 6.4: Example differential conductance curves for Nb contacted to a Co 300nm / Cu 120nm bi-layer ((a) and (b)) and a Co 300nm / Cu 300nm bi-layer ((c) and (d)). Measurements were taken at a temperature of 4.5K. Contact normal state resistances: (a) 11Ω (b) 29Ω (c) 22Ω (d) 27Ω. Experimental data (blue circles) and fitting to the modified BTK model (red line) are shown.

We have employed this method of plotting P against Z and extrapolating to Z=0 to extract the intrinsic contact spin polarisation, which as discussed above, is not without merit. Both linear and quadratic fits have been used previously, and since there is no physical reason to suppose that either is an accurate representation of P(Z), we apply both methods here by way of comparison. In addition, Kant *et al.* have suggested an exponential dependence of P on Z^2, $P \approx P_0 \exp(-2\alpha\psi Z^2)$, where α is the spin-flip scattering probability and ψ is the ratio of the forward and backward scattering probabilities[90]. The origin of this theory lies in the assumption of multiple scattering at the interface affecting the spin polarisation of the material, thus this theory is essentially only valid for diffusive contacts. The authors found that the product $\alpha\psi$ was typically close to unity for their ballistic contacts, as might be

expected. Due to the low Z value of our contacts (Z<0.5) we have not used this exponential fitting, using instead the linear and quadratic fits discussed above. A plot of *P* against *Z* values taken from fitting of the Nb to Co 300nm/Cu 120nm PCAR spectra is shown in figure 6.5(a). Extrapolation to Z = 0 gives P_C=43±1% from a quadratic fit to the data, the linear fit however is very poor. We suggest that a quadratic fit is more appropriate, particularly considering that the dependence of G_N on *Z* is quadratic. These P against Z fitting techniques are still in common usage[93,94].

A plot of extracted P vs Z values for the Co 300nm / Cu 300nm data is shown in figure 6.5(b). A quadratic fit (red line) was made to the data, allowing extrapolation of P_C = 43±2%, the increased spread of the data being reflected in the increased error. It would appear that, within the uncertainty of the experiment itself, there is no measurable effect of increasing the Cu cap from 120nm to 300nm. Indeed, PCAR measurements of both of these systems closely resemble those reported for Co in chapter 5, where P_C was found to be 44±2%. It would seem clear that spin-polarised electrons are able to propagate through a Cu layer of at least 300nm thickness with virtually no loss of polarisation. This is not entirely unexpected, as previous authors have reported spin diffusion lengths of up to 1μm in Cu films[91]. Smaller spin diffusion length values have been reported elsewhere[92], suggesting that perhaps this length-scale is strongly dependent on sample preparation, crystalline structure and elemental purity. The Cu films used here are expected to be amorphous, due to being deposited at room temperature. The purity of the Cu target used for deposition is 99.95% which is relatively high, although some impurities may be introduced into the film due to atoms present in the chamber, as the system was only pumped to 9×10^{-6} mbar before deposition.

In order to further investigate the Co/Cu bi-layer system, and to attempt to determine the spin diffusion length in these samples, two further samples were prepared comprising Co 300nm/Cu 600nm and Co 300nm/Cu 1μm. The samples were prepared under the same conditions as previously, by sputter deposition from a base pressure of 9×10^{-6} mbar under an Ar gas flow rate of 2 sccm. Typical differential conductance curves for contacts of Nb tips to the film surfaces are shown in figure 6.6 (blue circles). Fitting of the data to the model of Mazin *et al.* is shown superimposed

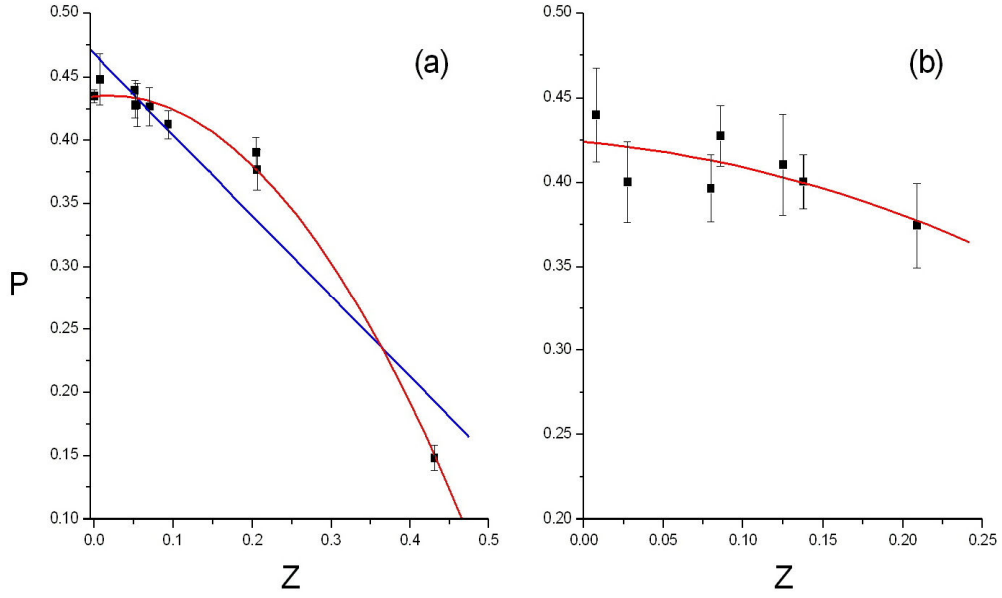

Figure 6.5: Plot of P and Z values extracted from the fitting of (a) Co 300nm/Cu 120nm and (b) Co 300nm / Cu 300nm PCAR data to a modified BTK model. Quadratic (red) and linear (blue) fits to the data are shown.

on the experimental data (red lines). Three free parameters extracted from the fitting are indicated in the figure.

For Co 300nm / Cu 600nm, the fit is typically very good for the central region, ignoring the additional dips which could be attributed to critical current or proximity effects. We expect only the central region to be well reproduced by the model, as it only considers spin polarised Andreev reflection at the interface. The superconducting gap Δ is typically found to be close to the bulk value of 1.5meV for the 10 junctions that were analysed. The interfacial scattering Z varies between 0 and 0.14, with an associated variation in P. A plot of P against Z for the 10 curves that were analysed is shown in figure 6.6 (c). As shown before, there is a roughly quadratic dependence of P on Z, and through fitting the data with a quadratic and extrapolating to Z=0 a value for the intrinsic spin polarisation $P_C\,(Z = 0) = 45\pm2\%$ can be extracted. This is again very similar to that of a pure Co film, suggesting that 600nm of Cu is still not sufficient to cause complete decay of spin information from the Co underlayer.

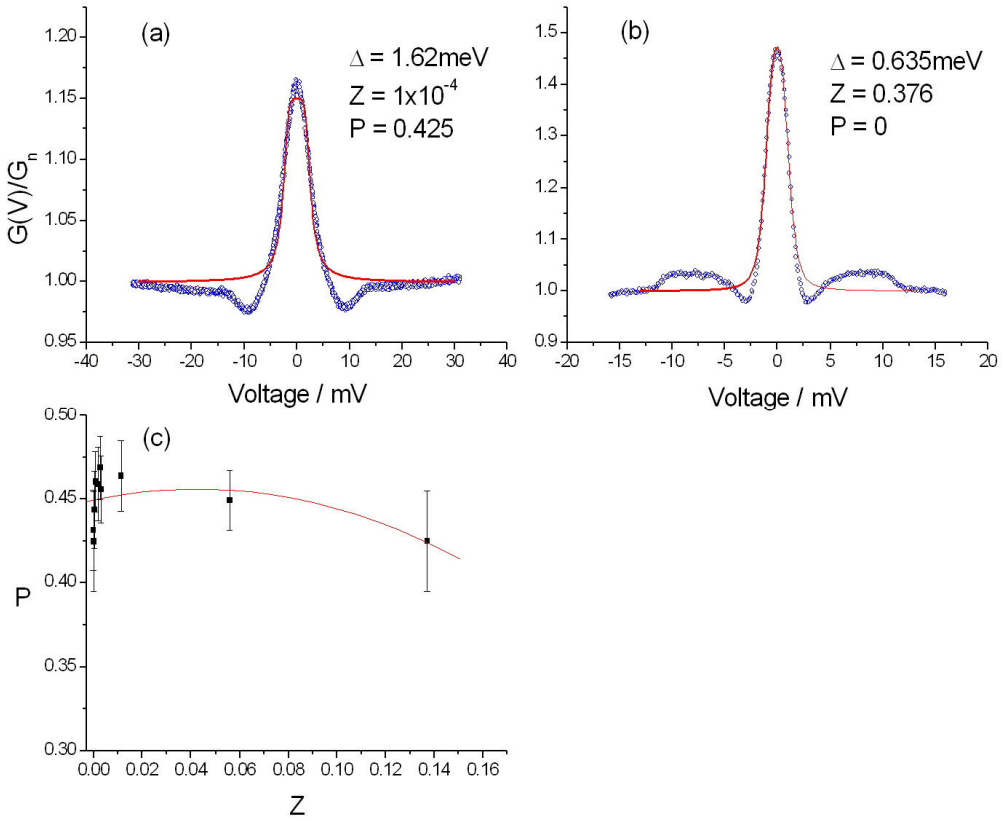

Figure 6.6: Example differential conductance curves for contacts of Nb tips to (a) Co 300nm / Cu 600nm and (b) Co 300nm / Cu 1000nm, showing experimental data (blue circles) and fitting to the model (red lines). (c) Plot of P and Z values extracted for the fitting procedure for 10 contacts to the Co 300nm / Cu 600nm film.

Turning to the Co 300nm / Cu 1 micron data, we find through fitting that P_C is very close to zero for all curves studied, however the Z parameter varies wildly. In order to investigate this behaviour further, we employ the method of Bugoslavsky *et al.*[88]. In the fitting procedure used here, the fitted curve converges on the experimental curve through successive iterations, until the increment of these iterations falls below a tolerance value. The resultant sum of squared deviations between the fitted and experimental values is described by

$$\chi^2(\Delta, Z, P) = \frac{1}{N}\sum_i [g_i - G(V_i; \Delta, Z, P)/G_n]^2, \qquad [6.1]$$

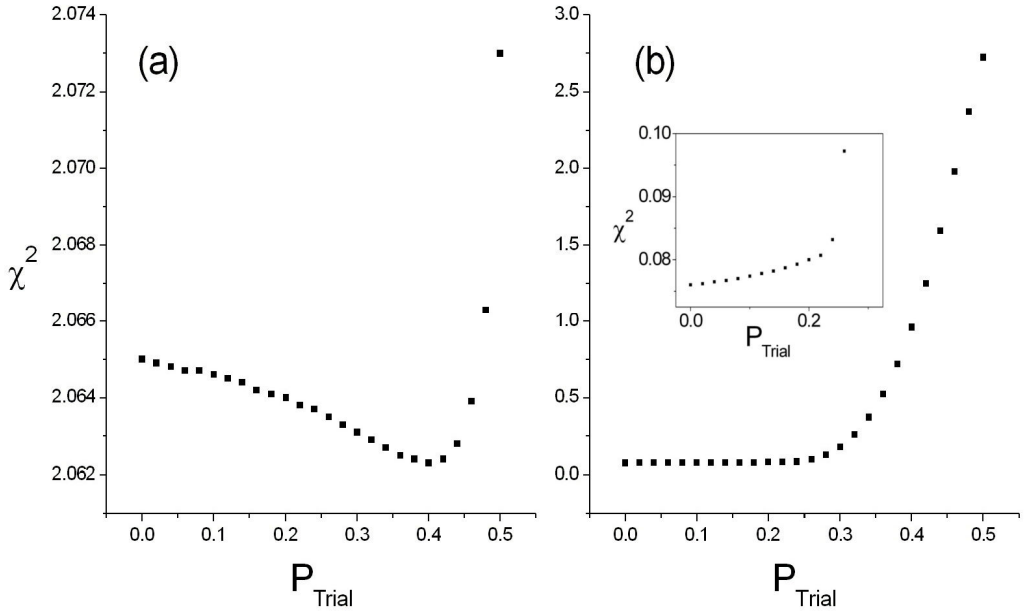

Figure 6.7: Plots of χ^2 as a function of trial values of P, for fitting of two experimental point contact curves (a) Co 300nm / Cu 600nm and (b) Co 300nm / Cu 1000nm. Magnification of the region for low values of P_{Trial} is shown as inset.

where the conductance data comprises N points (V_i , g_i) where g_i is normalised relative to the normal state conductance G_n and the fitted curve $G(V_i)/G_n$ is computed in the ballistic regime using the model of Mazin *et al.*[64]. By fixing the value of P as P_{Trial} and performing the fitting procedure over a range of values of P_{Trial}, a plot can be produced showing the variation of the minimum χ^2 value as P is varied.

Plots of minimum χ^2 against P_{Trial} are shown in figure 6.7 for an example conductance curves for the Cu 1 micron film, alongside Cu 600nm data for comparison. It can be seen from curve (a) that there is a clear minima in χ^2 at ~0.4, followed by a sharp increase as P_{Trial} tends towards 0.5. At this point Z is zero and cannot compensate the value of P any further, as Z cannot take negative values, therefore the quality of the fit drops rapidly. This clear minima suggests that the extracted value of P_C for the Co 300nm / Cu 600nm bi-layer is a unique solution, within tolerances of ±2-3%.

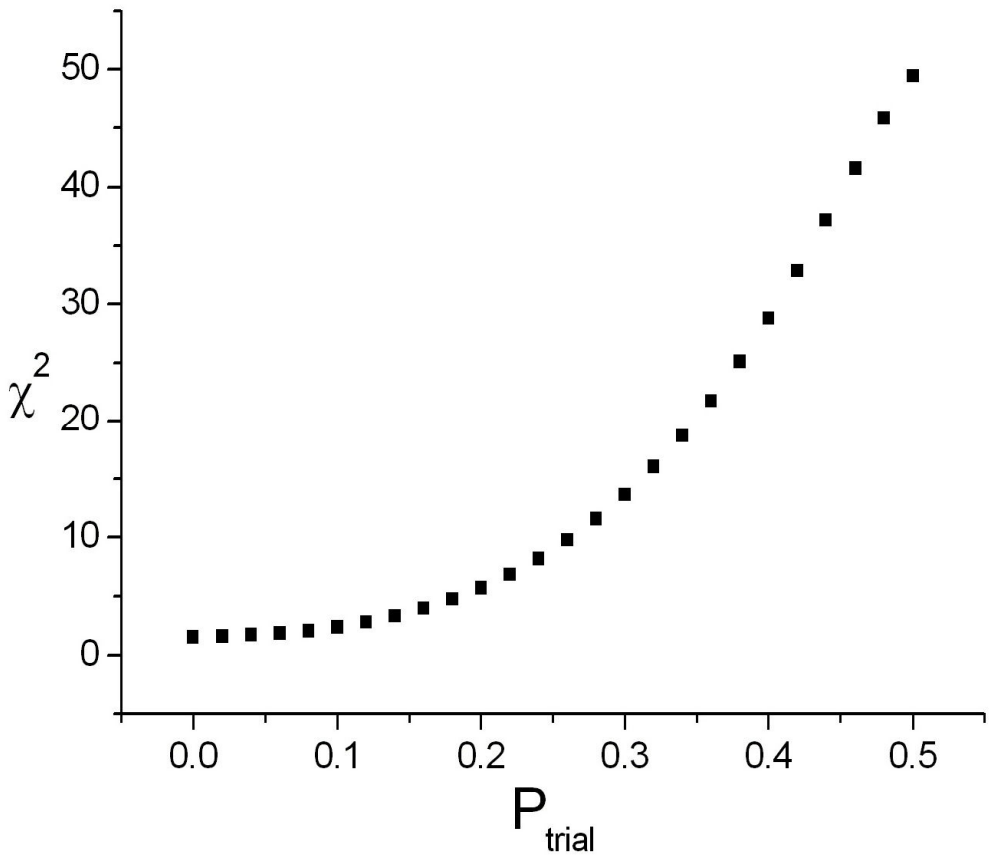

Figure 6.8: Plot of χ^2 as a function of trial values of P, for fitting of an experimental point contact curve for contact of a Nb tip to a pure Cu film.

For Co 300nm / Cu 1000nm we see very different behaviour, with an apparently flat χ^2 curve, diverging rapidly at $P_{Trial} \sim 0.3$. This would seem to suggest that the fitting parameters are completely degenerate and no unique solution for P_C can be obtained. However, on magnification of the region $P_{Trial} = 0$ to 0.3, an almost linear dependence is revealed, with the minimum value of χ^2 at $P_{Trial} = 0$. We can therefore deduce from this curve that the intrinsic value of P_C is close to zero, suggesting that the spin information from the Co underlayer has been completely lost. However due to the relatively flat nature of the χ^2 curve it is only possible to place an upper limit on P_C of ~ 10%. For comparison, a plot of χ^2 against P_{trial} is shown in figure 6.8 for the Cu point contact spectra that was presented in section 5.1. Very similar behaviour is seen to figure 6.7 (b), however χ^2 begins to diverge for lower values of P_{trial}, suggesting increased confidence in the extracted value of P_C.

Chapter 7: Point Contact Andreev Reflection in RFe_2 Laves phase compounds

Laves phase rare earth inter-metallic multilayers have been the subject of much study, particularly in the exotic exchange coupled exchange spring systems[8,9,10,11,95,96]. In order to further our understanding of the component materials of these multilayers, a study of the constituent Laves phase compounds is undertaken in this chapter. Molecular beam epitaxially (MBE) grown thin films of RFe_2 (R=Dy, Y, Er) compounds are characterised using a mechanical point contact Andreev reflection technique, in order to determine their degree of spin polarisation. As was discussed in section 2.1, the initial work of Slonczewski shows that the torque exerted on the magnetisation of a material is directly proportional to the degree to which the current is spin polarised[27]. An accurate understanding of the electron spin population distribution in these materials is crucial when one is considering potential applications for these materials. Features are observed in the experimental curves at high bias voltages that are inconsistent with a simple picture of Andreev reflection, and a discussion is made of the potential explanation for these features, using critical current and critical field based hypotheses. Application of an external magnetic field allows an estimate to be made of the local upper critical field H_{c3}, and measurements carried out at varying temperatures reveal the temperature dependence of the additional features mentioned above, allowing conclusions to be drawn as to their origin.

7.1: PCAR in a $DyFe_2$ Thin Film

A 400nm film of $DyFe_2$ was deposited via MBE onto a sapphire substrate with a 50Å Nb layer and a 20Å Fe seed layer, capped with 100Å Y, using a procedure detailed by Bentall *et al.*[83] and described in more detail in section 4.3. The Y cap prevents immediate oxidisation of the $DyFe_2$ layer beneath. Moreover, oxidisation in Y is self-terminating. Indeed, X-ray reflectivity data has shown that for a typical cap of 100Å of Y metal, 38Å is Y_2O_3, with the remaining 70Å non-oxidised Y[97]. An Y cap is non-ideal for point contact measurements, as the tip will be in contact with the capping layer. However, the cap is only 10nm thick, which is below the mean free path of Y at 4.2K, and therefore ballistic conduction electrons will still penetrate into the $DyFe_2$ layer beneath. Additionally Y is non-magnetic with zero spin polarisation, and therefore should have no effect on the PCAR signal. The effect of an Y capping layer on the extracted spin polarisation parameter is discussed in more detail in section 6.1.

Differential conductance curves for a Nb point contact to this $DyFe_2$ thin film are shown in figure 7.1. A clear Andreev reflection peak is visible at zero bias, but suppressed from a full doubling of conductance, with a peak maximum value of 1.14-1.17, dependent on the contact resistance. The characteristic dips seen in previous measurements of Cu and Co are visible between bias voltages of ±4-5mV, independent of contact resistance within the range investigated. As in the section above detailing measurements of Cu, these dips can be attributed to the creation of a proximity superconducting layer at the Nb/$DyFe_2$ interface. The dips are relatively broad, and this could be due to the finite lifetime of quasi-particles as was postulated earlier to explain the dips observed in Co, inelastic scattering in the surface layer shortens the lifetime of quasi-particles near the surface, and this is visible as a broadening of the characteristic dips in the differential conductance. Initially, however, it would appear to be unclear how a proximity layer can form in $DyFe_2$, which is ferromagnetic and therefore a strong pair-breaker, making it unlikely to support a thin superconducting layer at the surface of the film. The strong Fe-Fe exchange should prevent formation of Cooper pairs, making the pair state energetically unfavourable. However, it is important to note that there is a 10nm Y cap

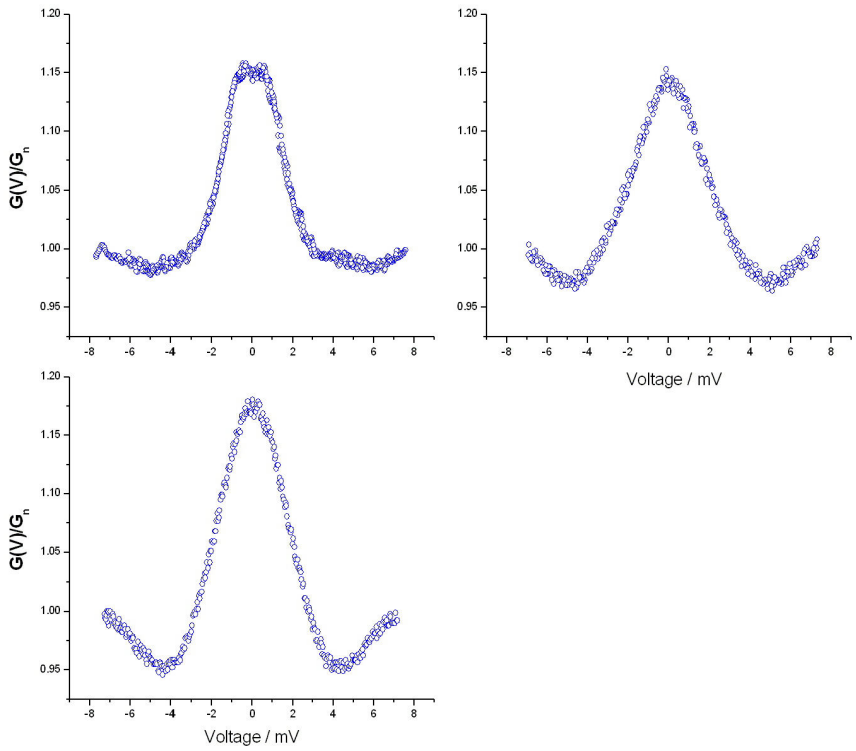

Figure 7.1: Differential conductance curves for Nb to a 400nm thin film of $DyFe_2$. Contact resistances are (a) 5 ohms (b) 14 ohms (c) 20 ohms.

present at the surface. Y is non-magnetic, and therefore it is possible in principle to set up a proximity layer in this material, similar to effects observed in Cu in section 5.1, and by earlier authors[65]. Critical current and critical field effects are an alternative explanation for these dips, as discussed in section 5.2 and later in this chapter.

Least squares fitting of the experimental data was performed to the modified BTK model of Mazin *et al.*, allowing three free parameters (Δ, Z, P). An example of the fitting of the data shown in figure 7.1 (a) can be seen in figure 7.2. The fitting procedure replicates the shape of the Andreev peak accurately, showing clearly the small dip at zero bias. As shown in chapter 3, this is characteristic of a non-zero Z value, and indeed this is what we see in the extracted parameters, with $Z = 0.189$. From the fitting we can see that $P_C = 37.4\%$ for this particular contact. The individual extracted value of P_C should not vary between contacts, however after performing

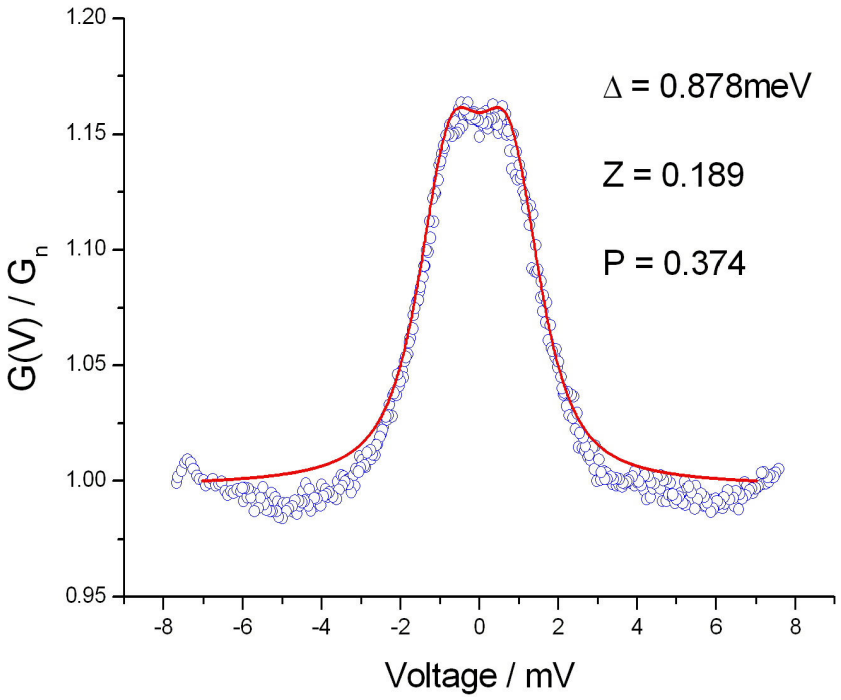

Figure 7.2: Differential conductance curves for a Nb point contact to a 400nm $DyFe_2$ film showing experimental data (blue circles) and a least squares fit to the modified BTK model (red line). Extracted fitting parameters are indicated on the curve (Δ, Z, P).

fitting of the remaining two curves it can be seen that the parameter P appears to have a dependence on Z. As established in chapter 6, this type of dependence is often seen in PCAR measurements[93,94], and is most likely due to the normal state resistance of the point contact containing a component due to the interfacial scattering, that is proportional to Z^2. This will shift the normal state conductance used in the normalisation downwards and result in a decrease in the measured value of P. In order to determine the intrinsic value of P_C, the P parameter is plotted against Z and an extrapolation made to Z=0 using a quadratic fit, as shown in figure 7.3 for $DyFe_2$. Extraction of $P_C(Z=0)$ gives a value for the intrinsic spin polarisation of this $DyFe_2$ film of 42±1%.

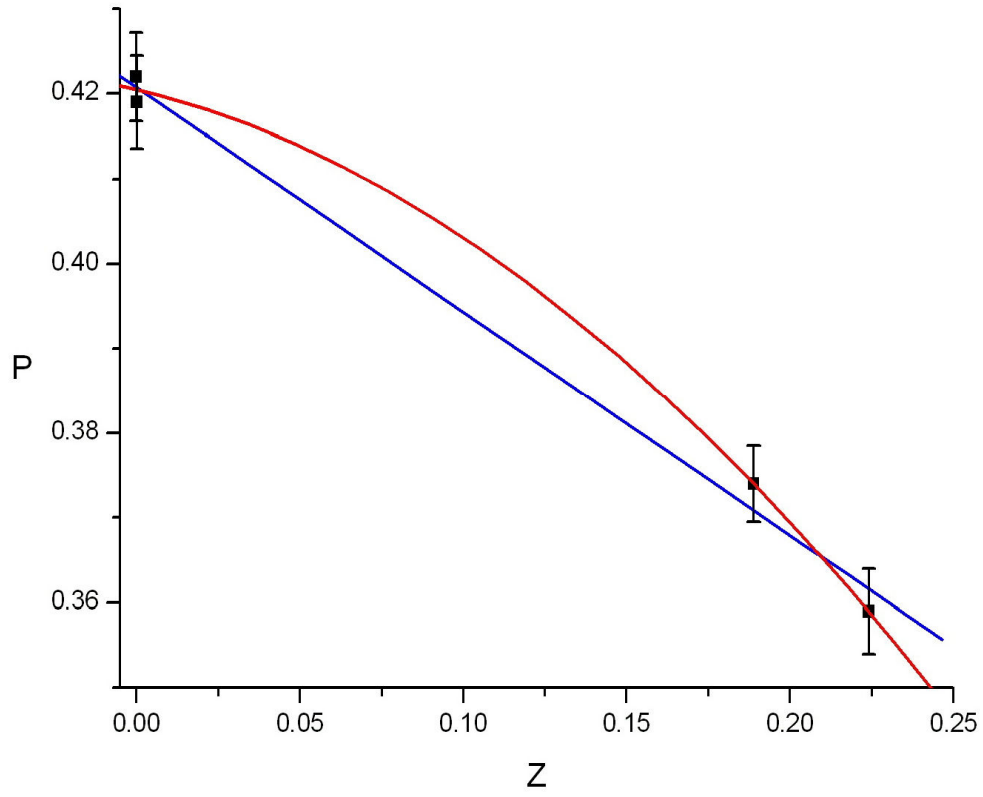

Figure 7.3: Plot of P against Z values taken from fitting of Nb to $DyFe_2$ PCAR spectra to the modified BTK model of Mazin et al. Linear (blue) and quadratic (red) fits to the data points are shown. Intrinsic $P_C(Z=0)$ values are 42.9% (linear) and 42.4% (quadratic).

It has been suggested by Woods *et al.* that if the value of the spreading resistance R_S is not known, as is the case here, then fixing the value of the superconducting gap Δ to either a known value or the bulk value from BCS theory may give a more accurate determination of the spin polarisation P_C[79]. However fixing the value of Δ to 1.5meV, the bulk value for Nb, results in quite a poor fit to the data, as the curve is artificially broadened to account for the increased value of Δ. However, despite this loss of parity, the fitting procedure produces P_C values that closely match the Z=0 extrapolated values quoted above, to within ±1%. This result increases confidence in the extracted value of P_C given above.

The value of P_C obtained for $DyFe_2$ (42±1%) is close to that of Fe, reported as 42-46% by earlier authors. This is at first sight surprising. $DyFe_2$ is an antiferromagnetically coupled system in which the 5d character of the Dy atom modifies the 3d ferromagnetism of the Fe[98]. This could well be expected to manifest as a deviation of the spin polarisation of $DyFe_2$ from that of pure Fe. However, surprisingly, here we observe the opposite. Detailed band structure information for $DyFe_2$ is not currently available, and therefore here we present a possible explanation for this behaviour based on the magnetic behaviour of the compound. Magnetism from the Dy sites in $DyFe_2$ is due to the 5d moments, driven primarily by the Fe sub-lattice via 3d-5d hybridization. The calculated 5d moment in $DyFe_2$ is $0.53\mu_B$, anti-parallel to the moment on the Fe site[98]. This is relatively small compared to the total calculated conduction electron magnetic moment of $DyFe_2$ ($3.08\mu_B$) from Brooks *et al.*, suggesting that the rare earth site plays a relatively small role in magnetic behaviour near the Fermi level. This provides an explanation for the P_C value reported here, because as set out in chapter 3, the spin polarisation of a material depends on the product Nv_F where N is the density of states at the Fermi energy. Anomalous Hall effect measurements performed on multilayers of similar compounds suggest that the Fe moments are dominant, further strengthening the conclusion that in these PCAR measurements we are primarily probing the Fe sub-lattice[16]. Clearly, further theoretical treatment of this system is necessary, primarily a first-principles calculation of the band structure of $DyFe_2$ close to the Fermi energy.

7.2: PCAR in an YFe_2 Thin Film

Continuing with the investigation of the RFe_2 Laves phase compounds, an 800nm thin film of YFe_2 was deposited on a sapphire substrate by MBE[83], using the method described in section 4.3. A 20Å seed layer of Fe deposited on a 50Å Nb buffer layer provides epitaxy for (110) growth. A 100Å capping layer of Y was again used to provide protection from oxidisation of the RFe_2 layer below. Differential conductance curves for Nb to YFe_2 point contacts at varying contact resistance are shown in figure 7.4, normalised to their normal state conductance G_n. Sharp dips are visible at relatively high bias voltages (10-15mV) for the larger contact resistances (smaller

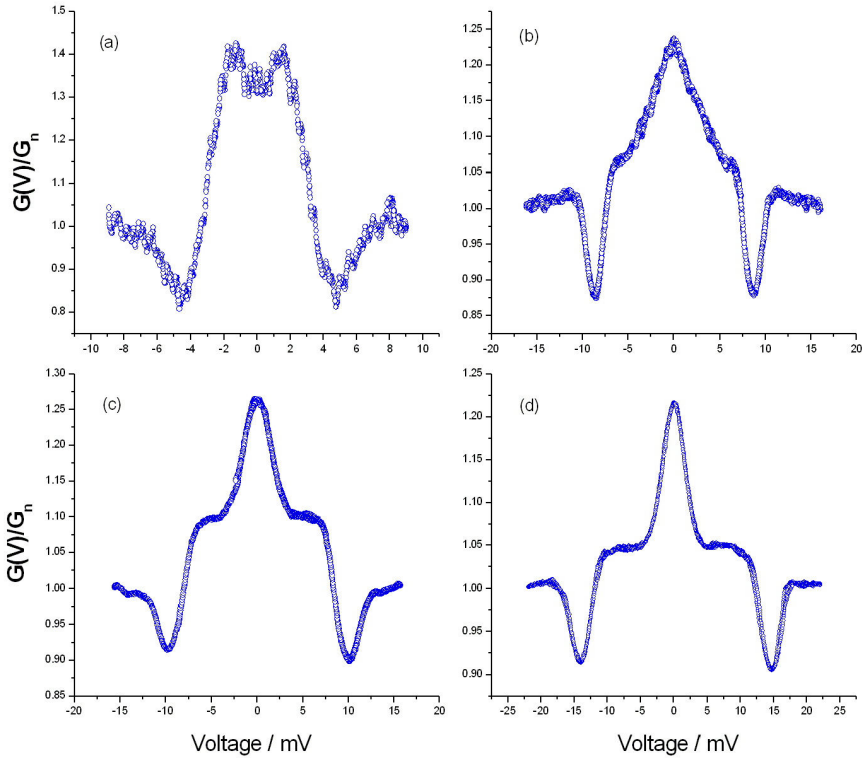

Figure 7.4: Differential conductance curves for Nb to YFe_2 point contacts (a) 9 ohms (b) 13 ohms (c) 18 ohms (d) 23 ohms.

contact diameters), outside the Andreev reflection region. The magnitude of these peaks is greater than any of the characteristic dips seen in previous PCAR spectra, and they are of similar magnitude to the main Andreev peak in size. We note that the voltage value at which the dips occur is dependent on the resistance of the contact, moving from 5mV for the 9 ohm contact up to 15mV for the 23 ohm contact. This suggests a current-based explanation for these features. On converting the voltage at which the dip reaches a minima to current, it can be seen that the current at which these features develop is constant at 0.60mA, within error.

A sudden increase in contact resistance at a particular current value is suggestive of breaking of superconductivity in the contact by penetration of flux into the tip from the Oersted field generated by the current passing through the contact. To examine this point, consider the Oersted field generated by a uniform current density flowing through a tip of radius r_0[99]. We find

$$B_\phi = 2\pi \times 10^{-5} Jr \qquad \text{for } r<r_0 \qquad [7.1a]$$

$$B_\phi = 2\pi \times 10^{-5} Jr_0^2 / r \qquad \text{for } r>r_0 \qquad [7.1b]$$

where B_φ is in Oe, J in A/cm^2 and r in μm. As Nb is a type-II superconductor, flux will begin to penetrate at H_{c1} = 1200 Oe[100]. Setting r = r_0 determined from the Wexler resistance formula as 16nm (Figure 7.4d) gives an estimate of a required current density of 1.1×10^9 Acm^{-2} to achieve a field equal to H_{c1}. This is somewhat higher than the current density of 4.6×10^8Acm^{-2} for the dips observed in figure 7.4d. However, we have made use of a relatively simple model, which assumes a simple circular contact radius and makes no consideration of the specific tip geometry; the bulk critical field for Nb may not be appropriate here. Also, we have taken the critical field at 0K, this value will be somewhat reduced at the experimental temperature of 4.2K. This transition will not necessarily be associated with a resistance increase in the superconductor, as vortices will be pinned at sites in the lattice. Only once the current reaches sufficient values to create a Lorentz force sufficiently high to move vortices will a voltage drop occur across the superconductor. This critical current mechanism was explored earlier in section 5.2 and is recounted here.

In the past, authors have attributed these large dip effects to a critical current effect in the superconductor[86]. At the current flowing through the contact reaches a certain value I_c the voltage across the contact begins to rise rapidly, resulting in a sharp dip in the differential conductance G(V). As the resistance of the superconducting element approaches the normal state, G(V) rises and stabilises at the normal state value G_n. This critical current effect might also be contributing to the dips observed in the YFe_2 spectra, as the peaks have a width of several mV. The current densities of for the YFe_2 dips agrees quite well with the estimates of Sheet *et al.*, who give the critical current density in their Au/Ta point contact as $3.6\text{x}10^8$A/cm^2 [86]. Given that the superconducting behaviour of Nb differs from that of Ta, this value should only be used as an order-of-magnitude comparison.

The dips are likely to become suppressed as the behaviour of the contact moves from diffusive to ballistic regimes, due to an increase in the relative contribution from the Sharvin resistance R_S. The switching of the Nb tip from superconducting to normal conduction results in an additional contribution to only the Maxwell resistance term R_M. As the resistance of the contact increases, this corresponds to a decreasing contact radius, and the ratio R_M/R_S also decreases. This causes the dip to be suppressed as the resistance change at the critical current is smaller relative to the main Andreev peak. This behaviour is evident in figure 7.4 from curves (a)-(c) as the contact resistance increases, the dip decreases from approximately $0.2G_n$ to $0.08G_n$.

Least squares fitting of the Nb/YFe_2 curves from figure 7.4 to the modified BTK model of Mazin *et al.* were carried out, and an example of the fitting procedure applied to figure 7.4(d) is shown in figure 7.5. Fitting has been restricted to low bias voltages, given that this is the region where Andreev reflection takes place. Behaviour outside this region has been discussed previously, and can be considered to contain features due to non-Andreev superconducting effects, such as critical field/current or proximity effects. As can be seen from the figure, the fitting provides a good fit to the data, accurately reproducing the Andreev reflection peak close to zero bias. A value of Δ = 1.34meV is extracted from the fitting, quite close to the bulk value for Nb. The reduction from the bulk value is most likely due to the restricted geometry of the tip. Also, the Nb wire used to produce the point contact tips may potentially contain a large number of defects, due to the mechanical processes used during manufacture[88]. Both of these effects may be expected to contribute to this observed reduction in the superconducting gap. As can be seen from figure 7.5, Z is very low, and was found to be consistently low for all of the contacts examined. Due to the low observed Z values, we take a numerical mean value of the extracted P values, arriving at an intrinsic value of P_C = 43±2%, slightly higher than that reported for $DyFe_2$ and similar to P_C for Fe quoted previously. This suggests that the Y has very little effect on the spin polarization of the compound. At first sight this is again surprising given the different structures of the cubic Laves YFe_2 and BCC elemental Fe. Again we present an argument based on the magnetic moments of the compounds, in the absence of detailed band structure calculations. In YFe_2 the 4d moment on the Y site is small ($0.44\mu_B$)[101], while the moment on the Fe site has been obtained from neutron scattering

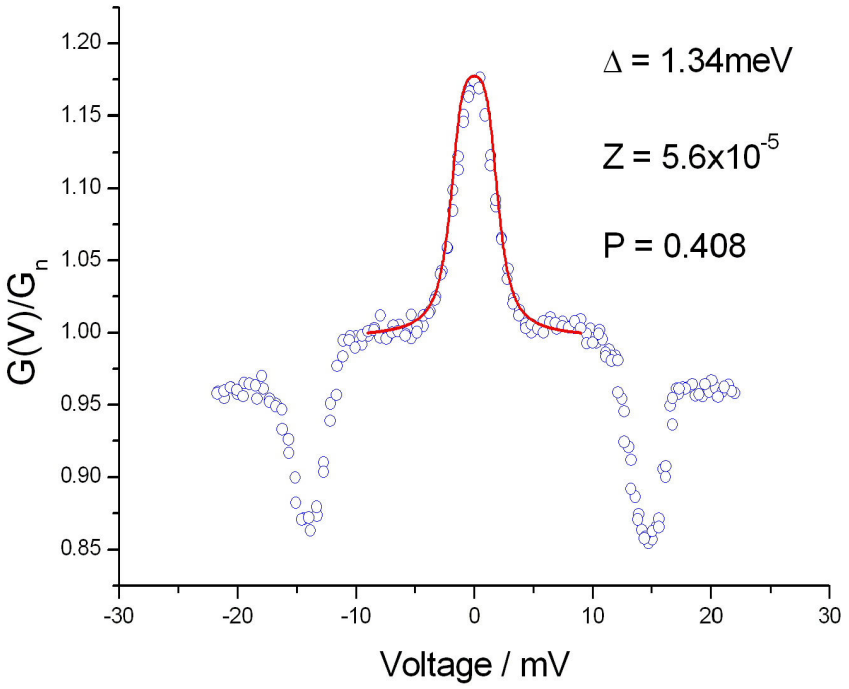

Figure 7.5: Least squares fitting of the modified BTK model of Mazin et al. (red line) to the experimental data of figure 5.8(d) (blue circles). Fitting is restricted to the region in which the behaviour can be considered primarily Andreev-like.

as $2.3\pm0.3\mu_B$[102], close to that of elemental Fe ($2.2\mu_B$). Band occupation at the Fermi surface for both bcc-Fe and YFe_2 is likely to be very similar. This presents a potential explanation for the spin polarisation of YFe_2 being close to that of Fe.

7.3: PCAR in YFe_2: Temperature and Magnetic Field Dependence

Measurements were also carried out on YFe_2 to determine (i) the effect of increasing the temperature of the contact towards the critical temperature of the superconducting tip and (ii) the effect of the application of an external magnetic field to the PCAR spectra. The critical temperature T_c for bulk niobium is 9.5K, and it is to be expected that the experimentally measured value for a Nb tip will be close to this

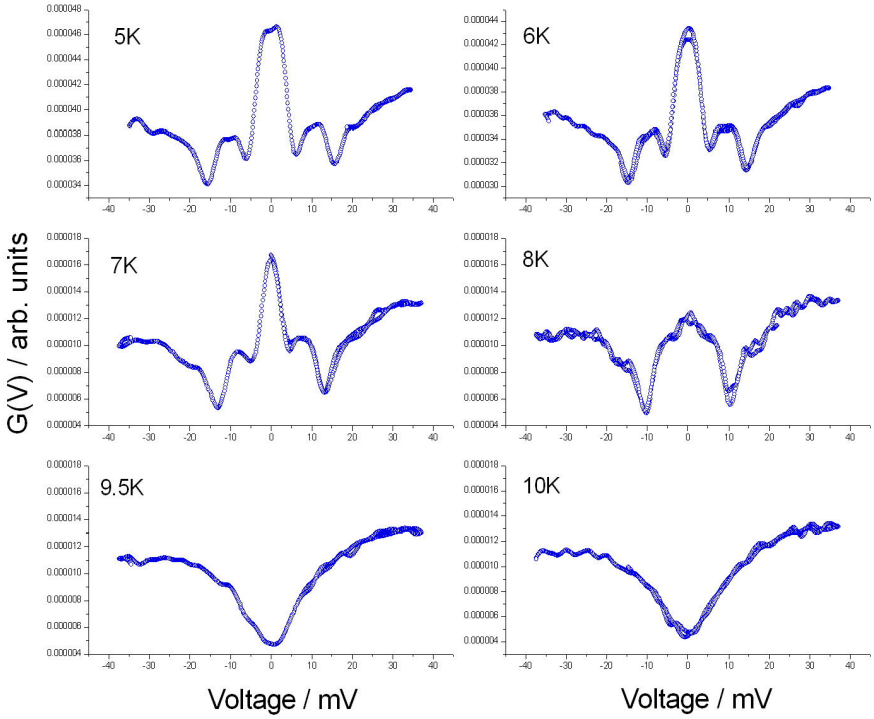

Figure 7.6: Differential conductance curves for Nb to YFe_2 at a range of temperatures, indicated within the figure. Andreev reflection is suppressed at higher temperatures and the effect vanishes at T ≈ 9.5K, the critical temperature of bulk Nb.

value, with a possible reduction due to the confined geometry of the Nb tip. Figure 7.6 shows PCAR spectra for Nb contacts to an 800nm YFe_2 thin film (deposition as described in section 7.2), taken at various sample temperatures, measured using a Cernox temperature sensor mounted directly beneath the Al_2O_3 substrate. Details of the experimental setup are given in chapter 4.

A clear Andreev reflection peak can be seen from 5-7K, with little suppression; at 8K the peak is quite heavily suppressed to a lower value as the tip begins to return to the normal state and ceases superconducting. At T ≈ 9.5K no features are visible, and the curve resembles a normal metal to metal point contact spectra. The high temperature data confirms that superconductivity has indeed ceased. In the 5K curve, two dips are visible at ±5mV and ±16mV. The first of these dips could be attributed to

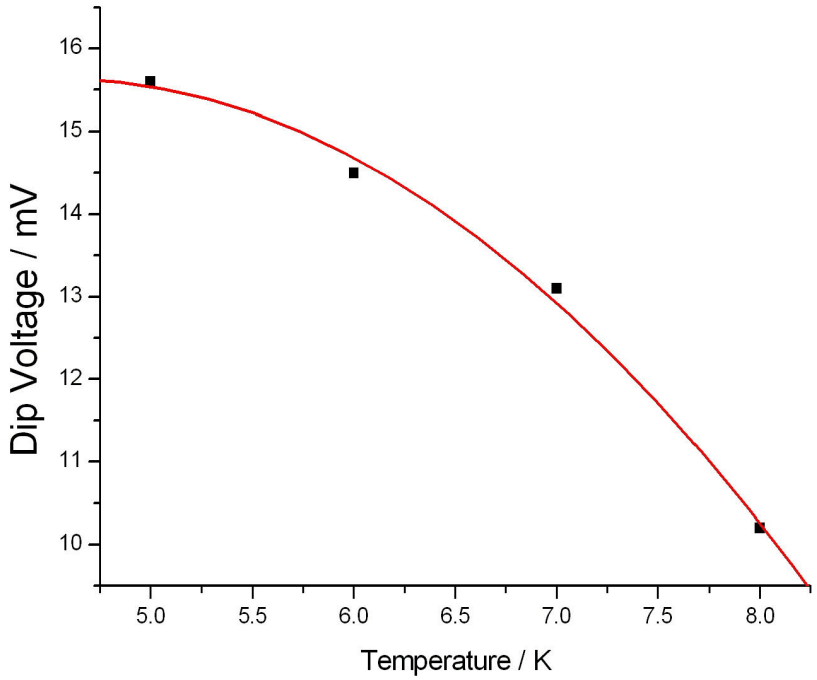

Figure 7.7: Dip voltage at which critical field effect is observed plotted against contact temperature. Red line shows a quadratic fit to the data.

the proximity effect, as discussed earlier. The second pair of dips moves to lower bias voltages as the temperature increases. Note that the resistance of the contact is kept constant, thus any change in these features is due solely to the change in temperature. As the temperature is increased, the critical field value will decrease, resulting in the dip value moving to lower bias voltages.

This relationship can be clearly seen in figure 7.7, where dip voltage is plotted against T, showing a quadratic dependence on T. If we attribute these dips to the critical current effect in the Nb tip, then we can expect the required current and corresponding self-field required to cause vortex motion in the superconductor to reduce with increasing temperature. Phenomenologically, the critical field H_{c1} behaves as

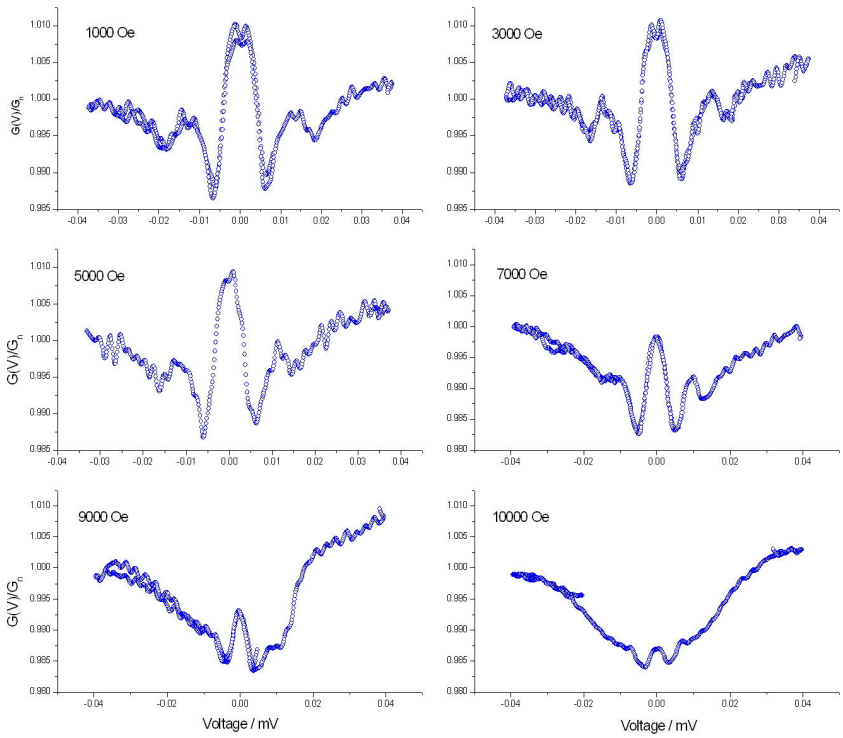

Figure 7.8: PCAR spectra for a 26 ohm Nb to YFe_2 point contact under varying applied magnetic field, as indicated in the figure.

$$H_{c1}(T) \approx H_{c1}(0)[1-(T/T_c)^2] \qquad [7.2]$$

under variation in temperature, where T_c is the critical temperature of the superconductor. From equation 7.1a, the self (Oersted) field due to the applied current through the contact is proportional to the current density, which in these measurements will depend solely on the dip voltage, as the resistance is kept constant (and therefore also the contact diameter). Therefore, the dip voltage is directly proportional to the induced Oersted field.

Differential conductance plots for a single Nb to YFe_2 contact with a normal state resistance of 26 ohms, under varying applied fields perpendicular to the sample plane between 0 and 1T, can be seen in figure 7.8. Suppression of Andreev reflection begins at 5kOe, suggesting the local onset of H_{c1}, the point at which reduction of the

superconducting efficiency of the tip begins due to the formation of vortices within the Nb tip. The degree of suppression increases as the field is ramped past this value, however the Andreev peak appears not to be fully suppressed even at 10kOe. For fields exceeding 20kOe, PCAR spectra (not shown) show complete suppression of the Andreev reflection behaviour, suggesting a value of H_{c3}, the critical field up to which the outer surface of the Nb tip can remain superconducting. This estimate of the maximum critical field for superconductivity to remain in the tip shows good agreement with similar measurements carried out by Miyoshi *et al.*, who found a local upper critical field of 20kOe in Nb/Cu point contacts[103].

7.4: PCAR in an $ErFe_2$ Thin Film

In section 7.1, the spin polarisation of $DyFe_2$ was determined through point contact Andreev reflection. Subsequently, the spin polarisation of YFe_2 was determined and the behaviour of the conductance under an applied magnetic field and at varying sample temperature was examined. We now return to the RFe_2 Laves phase intermetallic (where R is a heavy rare earth), examining the PCAR behaviour of a thin film of $ErFe_2$. In section 7.2 it was suggested that the closely coinciding values of spin polarisation in Fe films and in a $DyFe_2$ film indicates that the Fe sub-lattice is dominant within the intermetallic. If our conclusion that the rare earth site plays little role in the magnetism of the compound at the Fermi energy is correct, then similar behaviour should be seen in $ErFe_2$ as for $DyFe_2$, which would serve as confirmation of this hypothesis.

A 400nm film of $ErFe_2$ was prepared by MBE through deposition onto a 50Å Nb and 10Å Fe seed layer[83], using the procedure described in section 4.3. The sample was capped with 50Å of Y to prevent oxidisation of the film. Differential conductance spectra were obtained between a Nb tip and the sample surface at a range of contact resistances between 5-40Ω. Data obtained at resistances outside this range displayed features inconsistent with Andreev reflection and were not analysed. Figure 7.9 shows two example PCAR curves at a temperature of 5.1K, obtained at varying pressure of the contact to the surface, corresponding to contact resistances of (a) 19Ω and (b) 20Ω.

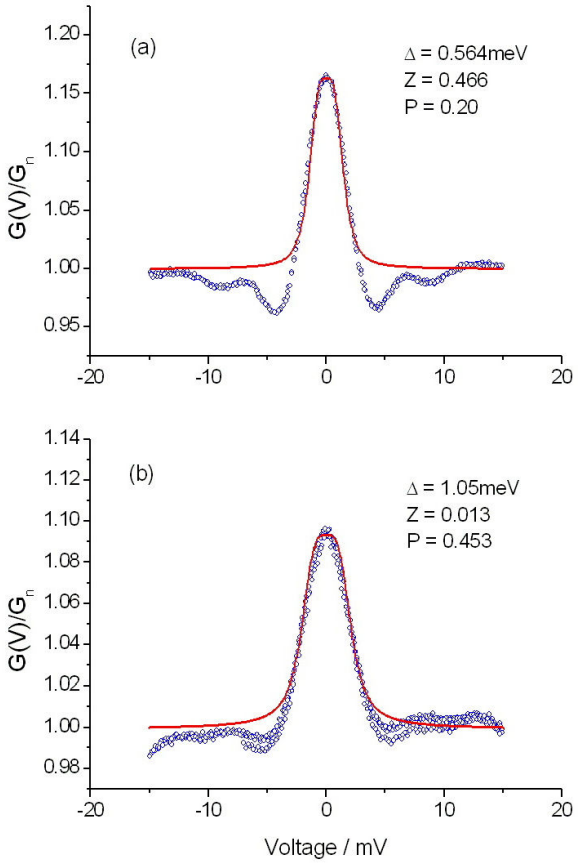

Figure 7.9: Typical differential conductance curves obtained from point contacts of Nb to a 400nm $ErFe_2$ film at a temperature of 5.1K. Fitting of the experimental data to the model of Mazin et al. (red line) is shown superimposed on the experimental data (blue circles). Extracted free parameters from the fitting are indicated in the curve.

Least squares fitting of the experimental data to the model of Mazin *et al.*[64] are shown superimposed on the experimental data in the figure, with the corresponding extracted free parameters Δ, Z and P. In some cases, as the contact is adjusted, the curve resembles very closely the Mazin *et al.* model for all voltages, for example figure 7.9 (b). In other cases, however, dips emerge at bias voltages of ~5mV and greater.

Potential explanations for these features have been discussed previously, perhaps the most likely explanation is the onset of normal conduction in the otherwise superconducting tip due to the current in the tip reaching the critical current I_c[86]. However, this does not explain why in some cases we observe two dips at two discrete

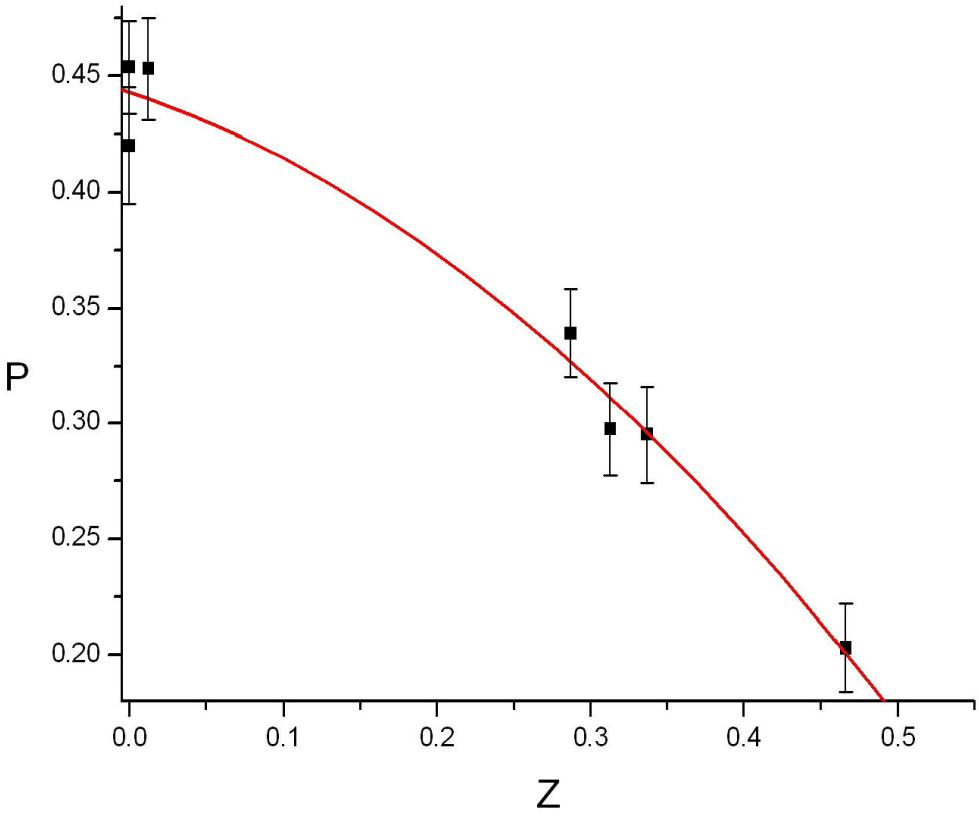

Figure 7.10: Plot of the extracted P and Z parameters for 7 $ErFe_2$ curves analysed using the Mazin et al. model, showing a strong Z dependence of P. A quadratic fit to the data is shown in red.

voltage values. A potential reason for this is that one dip can be attributed to the proximity effect, the leaking of Cooper pairs into the non-magnetic Y capping layer. This would be the dip occurring at the lowest energy, near to the bulk superconducting gap of the Nb tip. The second dip at higher voltage could then be attributed to the critical current. However, it is difficult to distinguish between the two mechanisms. Additionally, the measured curve may in fact be a superposition of two conductance curves, from two individual contacts on the tip, resulting in multiple dips being observed due to the same mechanism[104]. While it is non-trivial to determine the origin of these dips, it should be noted that they can be expected to have little effect on the measured spin polarisation – they should not affect the normalisation of the curve by a significant amount.

As can be seen from figure 7.9, there is a strong dependence of the spin polarisation parameter P on the degree of interfacial scattering Z. The extracted parameters for 7 individual curves fitted with the Mazin *et al.* PCAR model are plotted in figure 7.10. As discussed earlier, a Z^2 dependence of P is expected, and a quadratic fit to the data is shown in red. We extract an intrinsic value for P_C by extrapolation of the curve to Z=0, arriving at P_C (Z=0) = 44±2%. Again, this value is very close to 43% obtained for pure Fe (see section 5.3) and also to 42% for $DyFe_2$ (section 7.1).

The extracted spin polarisation for $ErFe_2$ would appear to support the conclusions made earlier for $DyFe_2$, indicating that the rare earth moments in the Laves phase intermetallic play little role in the magnetism at the Fermi surface, and hence in the contact spin polarisation. The 4*f* moments, primarily responsible for the magnetic behaviour of the rare earth, are located 7.5eV below E_F, and hence play little role in determining the spin populations of electrons at the Fermi level[105]. The other component of the rare earth moment, the 5*d* electrons, are primarily driven through exchange coupling with the Fe 3*d* moments, in which the Fe sub-lattice is dominant[98]. It is therefore not surprising that in PCAR, where we probe the spin behaviour at the Fermi surface, we detect primarily the Fe sub-lattice. Similar conclusions were drawn from recent anomalous Hall effect (AHE) measurements of $ErFe_2$ / YFe_2 multilayers, where it was found that the AHE is driven by the Fe sub-lattice, with the Er moments playing little or no role[16].

Chapter 8: Spin Transfer Effects in RFe_2 Multilayers

Exchange spring systems have been widely studied, for potential applications as enhanced permanent magnets, and for future data storage applications. Particularly relevant to the measurements presented here, R-TM exchange spring systems have been studied in detail, through magnetoresistance[11], magnetometry[12,13,14] and anomalous Hall effect measurements[16]. $ErFe_2$ / YFe_2 multilayers have been found to exhibit exotic magnetic behaviour, displaying not only exchange spring behaviour but also unusual spin flop behaviour at high temperatures[15]. Magnetic anisotropy is perpendicular-to-the-plane in these MBE-grown multilayers, with the easy axis lying along the [110] growth direction at high temperatures due to strain induced in deposition[48].

Spin transfer effects in magnetic films have been studied extensively both experimentally[25,26,106] and theoretically[22,23]. Point contacts and constrictions are commonly used to create a large current density, enhancing the spin transfer torque exerted by an applied current. Chen *et. al* have studied the magnetic switching of an exchange-biased Co film, through application of a current of the order of mA through a Cu tip in contact with the film surface[107]. They attributed switching effects to the reversal of a single domain beneath the tip through spin transfer from the applied current. We apply a similar method here, in order to investigate the spin-polarised current switching behaviour of exchange spring multilayer systems. We present differential resistance measurements made for Ag point contacts to an [50Å $ErFe_2$ / 100Å YFe_2]×27 superlattice in section 8.1. In section 8.2, point contact measurements of a 40Å $DyFe_2$ / 160Å YFe_2 / 40Å $DyFe_2$ trilayer are presented and discussed.

8.1: Current-Induced Magnetic Switching in an $ErFe_2/YFe_2$ Multilayer

A [50Å $ErFe_2$ / 100Å YFe_2]×27 multilayer sample was deposited by molecular beam epitaxy[83] (MBE), using a procedure described in detail in section 4.3. A 100Å Nb buffer and 20Å Fe seed layer were deposited onto an epi-prepared $(11\bar{2}0)$ sapphire substrate. The RFe_2 material was grown in (110) orientation by co-deposition of elemental fluxes at a substrate temperature of 400˚C. The sample was capped with a 100Å Y layer to prevent oxidisation of the rare earth material. Magnetometry data obtained using a vibrating sample magnetometer (VSM) is shown in figure 8.1, at a temperature of 10K. A Cu tip, fabricated by mechanical polishing using increasing fine degrees of sandpaper, was brought in contact with the multilayer film surface, at a temperate of 4.2K. Differential resistance curves measured across this junction for an applied current of ±10mA are shown in figure 8.2, under an applied out-of-plane field along the [110] growth direction of 7.8T to 9.5T. Under low fields (not shown), the resistance curve displays normal ohmic behaviour, with a small decrease in resistance as the current is increased, due to the partially tunnel junction-like nature of the contact. Oxide layers on the tip and sample surface result in current-dependent resistivity at the point contact.

As the field is increased to the coercive field of the multilayer (~7.8T, see figure 8.1), a reversible, non-hysteretic step appears in dV/dI of 0.15Ω at a current of +3.5mA. A similar step continues to appear as the field is increased, vanishing as the applied field is ramped beyond the coercive step, and the multilayer is saturated in the out-of-plane easy axis direction. As the field is swept back towards zero and the exchange spring unwinds, no resistance step is observed. We suggest that the applied current causes the switching of a nanodomain underneath the tip, due to pressure on local domain walls induced by the applied, spin polarised current. Domain wall magnetoresistance (DMR) will arise, due to spin-dependent scattering in the domain wall separating the created nanodomain from the bulk layer. The observed resistance step occurs only for one applied current polarity, suggesting that only when spin-polarised electrons flow parallel to the applied field and from the bulk of the sample to the upper, YFe_2 layer will switching occur. This is as expected, as for spin momentum

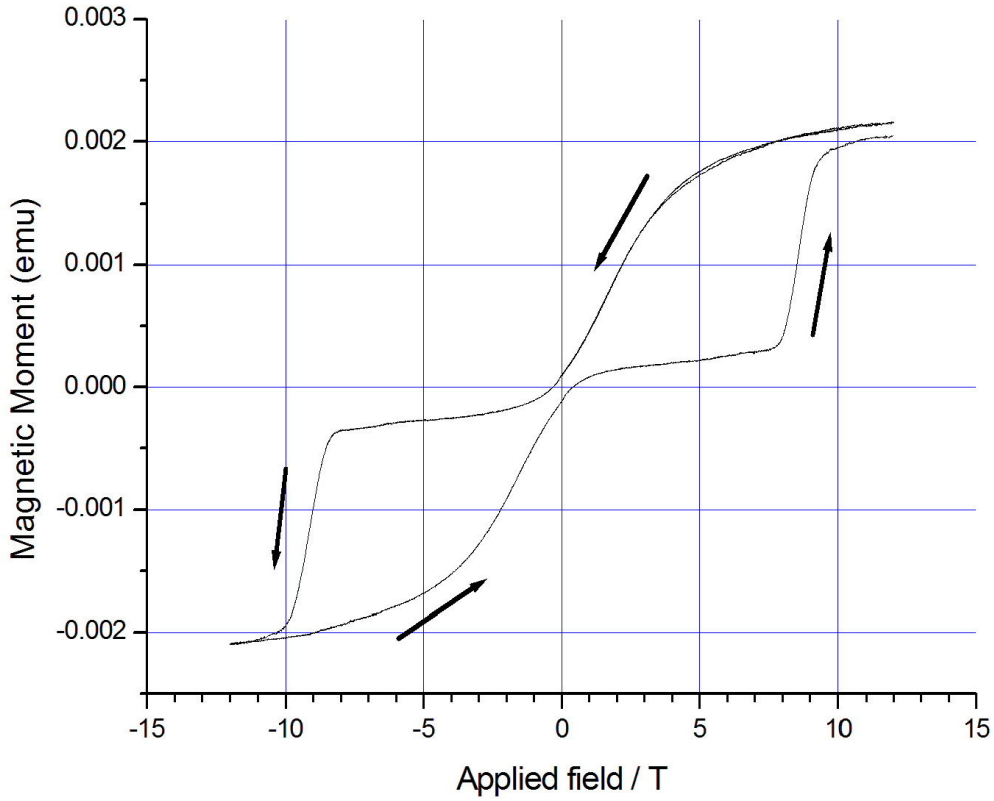

Figure 8.1: Vibrating sample magnetometer data for an [$ErFe_2$ 50Å| YFe_2 100Å]x27 multilayer, taken at a temperature of 10K, showing switching of the hard $ErFe_2$ layers at an applied field of ~8T, concomitant with the creation of an exchange spring in the YFe_2 layers, which unwinds reversibly on reversal of the field sweep.

transfer to occur the electron population must be spin polarised, meaning the directionality of electron flow must be from the sample into the tip, in order to switch the top YFe_2 layer. The proposed mechanism for this magnetoresistance is shown schematically in figure 8.3.

While the multilayer is in the coercive transition, the hard $ErFe_2$ layer has begun to switch, and the Er moments begin to align with the field. Concomitantly, the Fe moments in both layers, which align anti-parallel to the strongly anisotropic Er moment, rotate. We suggest that in this state of transition the Fe moments located furthest from the hard $ErFe_2$ layer, ie. those directly beneath the tip at the film surface,

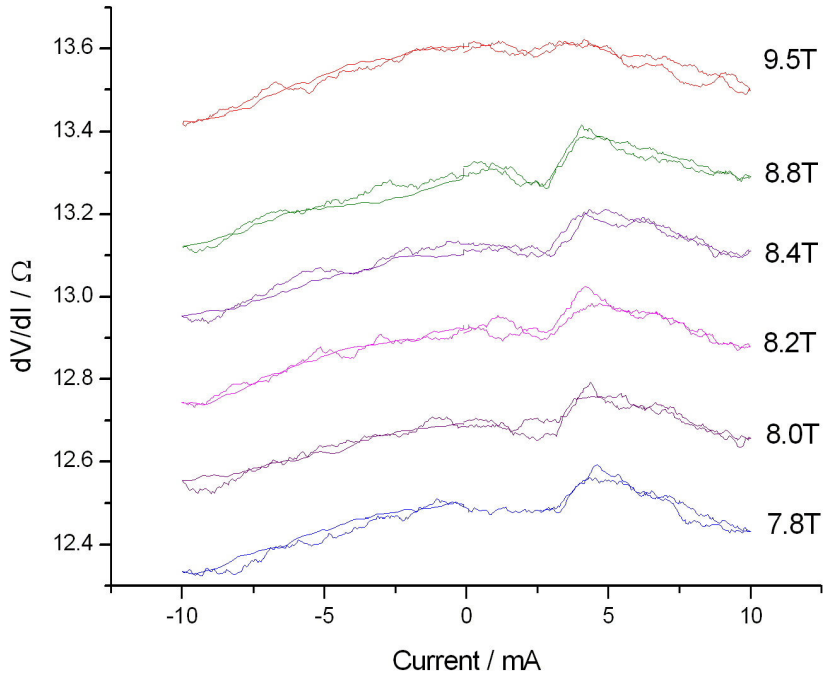

Figure 8.2: Differential resistance curves for a point contact of an Ag tip to an [$ErFe_2$ 50Å| YFe_2 100Å]x27 multilayer at applied out-of-plane magnetic fields of 7.8T to 9T. A clear, reversible step in resistance can be seen at ~3.5 mA. Curves are shifted vertically for clarity; a constant contact resistance of 12.5Ω at zero current was used.

can be relatively easily re-aligned by an applied spin-polarised current, through domain wall pressure as suggested above. Therefore, a nanodomain is created at the contact in the YFe_2 layer, resulting in an observed DMR at and above the current value required for creation of this state (+3.5mA). Due to the strong exchange coupling and the highly reversible nature of the exchange spring in the soft YFe_2 layer, once the current drops below this threshold the nanodomain is realigned anti-parallel to the Er moments and the minimum resistance state is recovered.

The evolution of the onset current and the current at which the system is fully saturated in the high resistance state as a function of applied field is plotted in figure 8.4, shown as black dots and red circles, respectively. Linear fits to the data are also shown, from these it is possible to extract parameters for the evolution of the critical

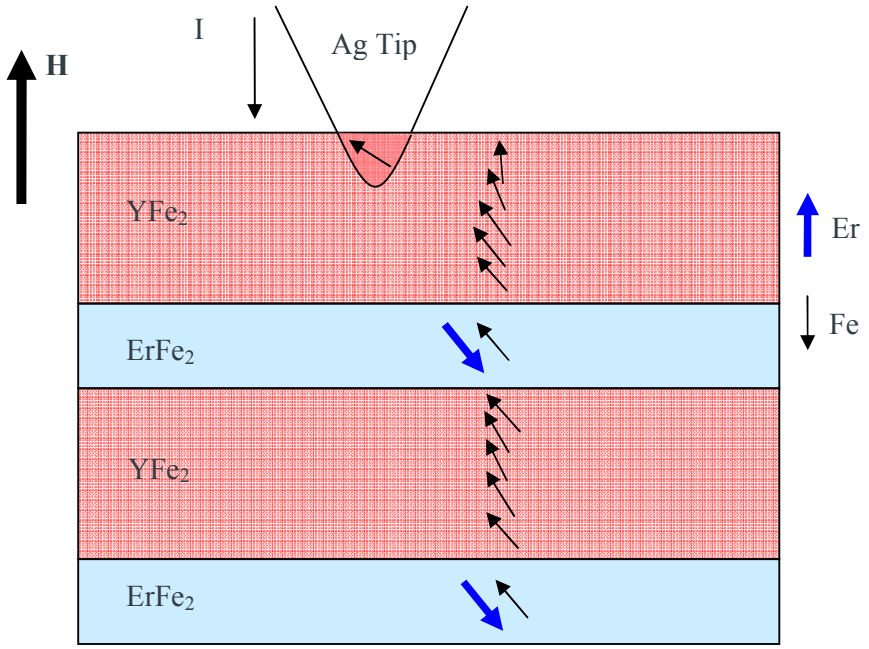

Figure 8.3: Schematic representation of the magnetic state of the [$ErFe_2$ 50Å / YFe_2 100Å]x27 multilayer at the coercive transition at high applied fields. The $ErFe_2$ layer has begun to re-align with the field, and an exchange spring is setting up in YFe_2 layer. A nanodomain in the YFe_2 layer is excited by the applied, high density current.

current as a function of field as 0.38 ± 0.11 mA/T and 0.49 ± 0.12 mA/T, for the onset and saturation current respectively. These values suggest an overall parameter for the step of 0.45 ± 0.11 mA/T. A linear dependence of critical current on field has been seen previously[107,108], and this value compares favourably to that for an exchange-biased Co film measured by Chen *et al.*, who found a value of 0.3mA/T for their system, measured using a similar arrangement with a Cu point contact. The critical current density associated with the steps observed here can be calculated using the contact diameter *a* determined from the contact resistance using the Wexler formula, as presented in section 3.1 (equation 3.7). The measurements here were made at a constant zero current contact resistance of 12.5Ω, using this value, the resistivity of an $ErFe_2/YFe_2$ multilayer at 4K (~$23\times10^{-6}\Omega$cm)[109] and the mean free path (11nm), the contact diameter can be estimated as 13nm. We therefore obtain a critical current density of 6.6×10^{8}Acm^{-2}, inserting the critical current as 3.5mA. This is roughly the same magnitude as that required by Myers *et al.*[25] to switch Co/Cu/Co tri-layers, and is

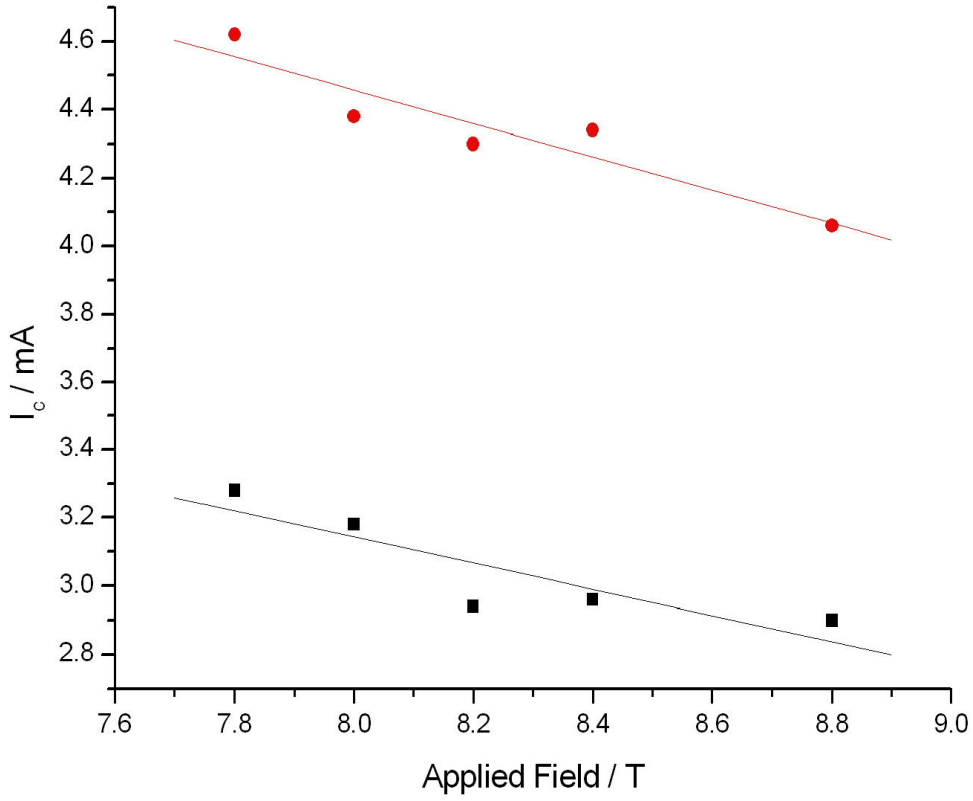

Figure 8.4: Plot of the critical currents I_c for the onset (black squares) and full saturation (red circles) of the multilayer into the high resistance state as a function of applied magnetic field.

lower than that required by Chen *et al.*[107] to switch a single exchange-biased layer of Co.

8.2: Spin Wave Excitations in a $DyFe_2$ / YFe_2 / $DyFe_2$ Tri-layer

The current-driven excitation of spin waves has been observed in a number of experimental systems, including Co/Cu multilayers[24,107] and Co/Cu/Co tri-layers[25] and patterned nano-pillars[26]. The behaviour of spin wave excitations under an applied

current was explored theoretically by Slonczewski in 1999[27]. More recently, spin wave excitation by mechanical point contact to a single layer of Co has been explored[108], showing the emergence of differential resistance peaks associated with spin wave excitation due to the precession of local magnetic moments at the contact under a high density spin-polarised current. We extend this method to a tri-layer of Laves phase $DyFe_2$ / YFe_2 / $DyFe_2$, using a mechanical point contact with a Ag tip to the sample surface to inject a high current density into the material.

A tri-layer comprising 40Å $DyFe_2$ / 160Å YFe_2 / 40Å $DyFe_2$ was deposited epitaxially using the MBE technique described in section 4.3, onto a sapphire substrate with a 50Å Nb and 10Å Fe seed layer[83]. The sample was capped with 30Å of Y to prevent oxidisation of the film. A mechanical point contact was made to the sample surface using an Ag tip at 4.2K, an external in-plane magnetic field was applied varying between ±10T. Differential resistance curves as a function of applied current between ±6mA are shown in figure 8.5. Despite the large background quadratic decrease in resistance, attributable to partially tunnelling-like behaviour due to the high resistance of the contact, a clear peak in dV/dI can be seen at -3.2mA. This peak is field-independent, suggestive perhaps of an explanation based on the large internal exchange field of the Fe sub-lattice, with the externally applied field contributing little to the spin precession of excited moments.

The peak in differential resistance observed consistently in the experimental curves occurs for one polarity of the applied current only. This asymmetry is in itself suggestive of spin wave excitation; for only one polarity of the current will the torque on the free layer (YFe_2) be such that the damping term in the Landau-Lifshitz-Gilbert (LLG) equation be suppressed, allowing magnetic moments to precess. The LLG equation modified to include spin transfer terms can be written[23]

$$\dot{\mathbf{S}}_2 = \hat{\mathbf{s}}_2 \times [\gamma H_{eff} \hat{\mathbf{s}}_1 \cdot \mathbf{S}_2 - \alpha \dot{\mathbf{S}}_2 + \frac{I g}{e} \hat{\mathbf{s}}_1 \times \hat{\mathbf{s}}_2] \qquad [8.2]$$

for the motion of the free layer magnet moment $\mathbf{S}_2$ under electrons incident from layer $\mathbf{s}_1$, where $\dot{\mathbf{S}}_2$ denotes the time derivative and $\hat{\mathbf{s}}_{1,2}$ are unit vectors along the direction of the magnetic moments of the layers. The first term is a steady precession, dependent

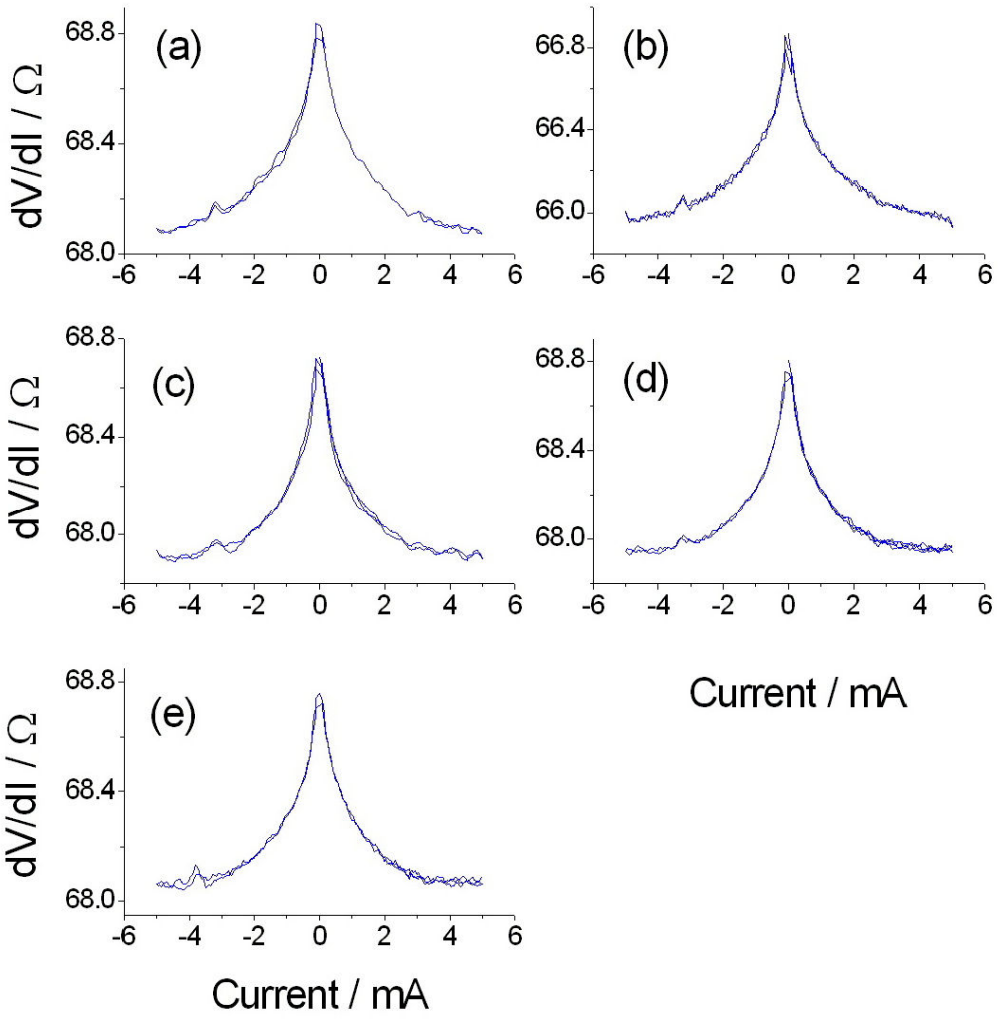

Figure 8.5: Example differential resistance curves as a function of applied current for a point contact of Ag to a 40Å $DyFe_2$ / 160Å YFe_2 / 40Å $DyFe_2$ tri-layer, under applied fields of (a) -10T (b) -5T (c) 0T (d) 5T (e) 10T.

on the effective field in the sample H_{eff} and the gyromagnetic ratio γ. This is damped by the second term, characterised by the Gilbert damping parameter α. If the third component, due to spin transfer from electrons incident from $\mathbf{S}_1$, is positive, then the Gilbert damping will be reduced, and precession in a spin wave configuration is favourable. This will occur when I in this expression is positive, which corresponds to electrons flowing from the tip through layer 1 ($DyFe_2$) into layer 2 (YFe_2). Carrying out a similar calculation for the critical current density for the onset of spin waves as was carried out in the previous section, the critical current of 3.2mA corresponds to an

estimated critical current density of 4.8×10^9 Acm^{-2} using the estimated contact size of 4.6nm from the Wexler formula. This agrees well with the magnitude of current density previous authors have required to excite spin waves in tri-layers (Myers *et al.*[25], Tsoi *et al.*[24]) and mono-layers (Ji *et al.*[108]).

We now consider potential physical mechanisms behind the observed features, which are suggestive of the excitation of spin waves. Consider a simple expression for the resonant frequencies of spin wave excitations[110]

$$\omega_0 = \gamma(B_0 - 4\pi M) + \frac{Dk^2}{\hbar}, \qquad [8.1]$$

where γ is the gyromagnetic ratio, B_0 the applied field and M the magnetisation of the film. D is the spin wave exchange constant, which will be constant for any given material, and $k = n\pi/L$ is the wavevector of the excited spin wave for a mode of n half-wavelengths in a film of thickness L. The first term is the ferromagnetic resonance frequency, and the second term is the contribution due to the ferromagnetic exchange (in the low k approximation). Previous authors have seen a strong field dependence of the current required to excite spin waves and the associated frequency[106], and have correlated this with the resonant frequency above with great success, neglecting the exchange term by considering only zero-wavenumber excitations. We propose that, in this constrained exchange spring system, the characteristic length scale of the exchange spring itself may be the dominant contribution, and give rise to the spin wave signatures detected in this experiment. We take the effective thickness L to be the thickness of the YFe_2 layer (160Å), using the interfaces with the adjacent $DyFe_2$ layers as boundaries to the spin wave excitation. We consider the n = 1 wave configuration, which will give the minimum excitation frequency, inserting an approximate value for $D \approx 300$meVÅ^2 for Fe from neutron scattering[111], making the assumption that the strong Fe-Fe exchange dominates. Using these values, we estimate $\omega_0 \approx 110$GHz for the contribution from exchange-driven spin waves with n=1.

In conclusion, peaks have been observed in the dI/dV spectrum of a point contact from a Ag tip to the surface of a $DyFe_2/YFe_2/DyFe_2$ tri-layer. Following the work of previous authors, these have been attributed to spin wave excitation in the tri-

layer. Unlike previous studies, the critical current required to excite the system is field independent. We propose that the applied current excites a non-zero wavenumber spin wave in the soft YFe_2 layer, constrained by the geometry of the exchange spring. Clearly more study of this system is needed to fully explain the origin of these features.

Chapter 9: Summary

The work presented in this thesis has been the study of the spin transport properties of rare earth – transition metal (R-TM) thin films and multilayers, using point contact techniques. Two superconducting magnet inserts were designed and constructed for performing point contact measurements on film samples, using a mechanical contact between a fine pointed metal wire and the sample surface. An electronics setup was devised for the measurement of differential conductance/resistance, using the point contact system. This utilised a Wheatstone bridge together with lock-in amplifier, for measurements sensitive to the order of 50mΩ. Point contact measurements were performed both in liquid helium, and in a variable temperature insert allowing variation in temperature and the application of a magnetic field up to 14T.

Point contact Andreev reflection measurements on transition metal (Cu, Co, Fe) films have been presented and discussed. On fitting the measured differential conductance data to a modified Blonder-Tinkham-Klapwijk[63,64] (BTK) model, the transport spin polarisation of these films was determined. Cu was found to have zero spin polarisation P_C, in line with expectations from the band structure of the metal at the Fermi energy. The differential conductance curve between a superconducting Nb tip and the Cu film surface shows additional features at high bias voltages that cannot be explained through Andreev reflection alone. These have been attributed to the superconducting proximity effect at the Nb-Cu interface, resulting in the formation of a weakly superconducting layer in the Cu film, in the vicinity of the contact. These features have been accurately reproduced using a two superconducting gap model of Andreev reflection, reproducing the dip features observed.

Differential conductance curves for point contacts of Nb to a sputter deposited Co film have also been analysed using the modified BTK model, allowing determination of spin polarisation (44±2%). Similarly, point contact Andreev reflection measurements on molecular beam epitaxy (MBE) deposited Fe allowed determination of the transport spin polarisation as 43%. Both of these values agree

well with those determined previously by Soulen *et al.*[62] and Strijkers *et al.*[65]. In all of the curves presented for these materials, additional features (dips) are observed at high bias voltages. Unlike those in Cu, these cannot be explained through the proximity effect, as this is likely to be highly suppressed in ferromagnetic materials. These features have been attributed to critical current values in the superconductor, resulting in resistance appearing in the superconductor itself, due to vortex motion induced by the Lorentz force.

The spin polarisation of bi-layer systems of Co/Y and Co/Cu has been investigated and discussed. For a thin layer of Y (10nm) on a thick Co underlayer, the non-magnetic Y has been found to have little effect on the measured spin polarisation, which was found to be 44±2%, very close to that measured for a pure Co film. But upon increasing the thickness of the Y capping layer to 100nm, the measured spin polarisation was eventually suppressed, to 33±3%. This observation supports the decision to use a 10nm capping layer of Y to protect R-TM samples, given that this model Co/Y system shows that the Y layer will not significantly affect the measured spin polarisation. This behaviour is as expected, and supports the assumption that the spin diffusion length in Y is larger than 10nm.

Bi-layers of Co/Cu have also been used as a model system to investigate spin propagation through a non-magnetic spacer layer, and measure the characteristic spin diffusion length in this layer. Co/Cu was chosen as this a well studied system against which the results of this study can be compared. For bi-layers with a thick Co underlayer (300nm) and Cu capping layers up to 600nm in thickness, the measured spin polarisation has been found to be very close to that of Co, in the region of 41-47%. This suggests that spin information from the ferromagnetic underlayer is able to propagate through around 600nm of non-magnetic Cu with no measurable loss of polarisation. However, for a micron thick layer of Cu we find behaviour close to zero spin polarisation, even though this measurement is less accurate due to the increased degeneracy between P_C and the interfacial scattering Z for weakly spin polarised materials, in the modified BTK theory. This finding of a spin diffusion length in excess of 600nm is consistent with the findings of previous authors. Jedema *et al.* found a spin diffusion length of 1 micron in F/Cu/F (F is a ferromagnetic metal) tri-layers at 4.2K[91], while lower values have been reported elsewhere[92]. This length-scale

is likely to be strongly dependent on sample preparation, crystalline structure and elemental purity.

The spin polarisation of two heavy R-Fe_2 Laves phase intermetallic compounds ($DyFe_2$, $ErFe_2$) and the yttrium based YFe_2 has been measured using the mechanical PCAR technique. These materials have been found to have spin polarisations close to that of Fe at 43%; $DyFe_2$, YFe_2 and $ErFe_2$ have been found to have P_C of 42±1%, 43±2% and 44±2%, respectively. This observation suggests the rare earth moments in the Laves phase intermetallic play little role in the magnetism present at the Fermi surface, and hence in the contact spin polarisation. This conclusion is supported by recent measurements of the anomalous Hall effect in an $ErFe_2/YFe_2$, where the Hall voltage was found to depend entirely on the Fe sub-lattice in the compound[16].

In the measurement of PCAR in RFe_2 materials, additional features have also been observed at high bias voltages that are similar to those that were seen in measurements on pure transition metal films. These features (dips) have again been attributed to the proximity effect and critical current threshold in the region of the contact. The behaviour of these dips has also been explored at a range of temperatures below the superconducting transition temperature of Nb (9.5K). The critical current required for these dips to occur has been found to obey a quadratic behaviour with temperature, suggesting a correlation with the critical field H_{c1} of the superconductor.

The main advantage of this mechanical PCAR technique is that it may be applied to a wide range of materials, provided a contact can be made to the surface using a superconducting tip. The results are described well by a relatively simple theory, which nonetheless incorporates all the essential physics. Previous workers have introduced additional parameters in order to improve the agreement between theory and experiment, notably the spreading resistance[79] and a broadening parameter[88]. Introducing additional parameters can be detrimental to the accuracy of the experiment, and result in increased degeneracy of potential fitted curves. We have found good agreement between experiment and theory, and find that the simple modified BTK theory of Mazin *et al.* allows comparison of transition metal and rare earth based compounds with a reasonable degree of accuracy.

The PCAR technique can also be used in reverse to probe the behaviour of novel superconducting materials, using a non-magnetic tip such as Cu. The technique has recently been successfully applied to study the new Fe-based class of high temperature superconductors[112,113]. Compared to the traditionally popular techniques for measuring spin polarisation using superconducting tunnel junctions[114] and photoemission experiments[115], PCAR has become increasingly popular in recent years. Photoemission spectroscopy is the most direct method of measuring *P*, but is limited in energy resolution to ~1meV. The tunnel junction method, while a powerful technique, requires careful sample deposition and preparation, as any break in the tunnelling oxide layer will render the experiment void. Also, the requirement of a uniform oxide layer restricts the number of materials to which the technique can be applied.

More recently, a new technique has been pioneered for measurement of the spin polarisation of materials, through time-resolved demagnetisation measurements[116]. Utilising a pump-probe optical technique, interactions between electrons, spin states and the lattice can be explored on the picosecond scale. Through theoretical analysis, this technique allows the degree of spin polarisation in the material to be determined. This technique may find widespread acceptance in the coming years, particularly as it requires minimal sample preparation, similar to PCAR.

Finally, preliminary results have been presented showing evidence of spin transfer torque-related phenomena in R-TM tri-layers and multilayers. Differential resistance measurements of a point contact of Ag to an [50Å $ErFe_2$ / 100Å YFe_2]x27 multilayer, in magnetic fields at the coercive transition of the hard $ErFe_2$ layer, show a step increase in resistance at a finite positive applied current. This has been explained through the creation of a nano-domain directly beneath the contact, by spin transfer-induced magnetisation switching through interaction with the spin-polarised electron current. The step is attributed to domain wall magnetoresistance, with anisotropic magnetoresistance excluded due to the step being observed for only one current direction. The critical current required for the creation of this domain is found to reduce linearly with field, at a rate of 0.45mA/T.

Similar measurements performed on a $DyFe_2/YFe_2/DyFe_2$ tri-layer have demonstrated a peak in differential resistance at negative bias current, which has been interpreted as a signature of spin wave excitation in the tri-layer. The current required to excite the spin wave has been found to be largely independent of the applied field. This suggests that the mode of excitation may be largely dependent on the constraints provided by the exchange spring. It is suggested that the applied current excites a non-zero wavenumber spin wave in the exchange spring in the YFe_2 layer, but more study is required to confirm the origin of these features.

It is clear from the results presented here that exchange spring systems show promise for spintronics applications. Layered hard/soft RFe_2/YFe_2 systems display evidence of switching behaviour and the generation of spin waves under the application of a spin polarised current, the dominant contribution to which is that of the Fe sub-lattice. It has been demonstrated that RFe_2 multilayers can provide model systems on which to study spin torque behaviour, for potential data storage and random access memory applications.

References

[1] P. Grünberg, R. Schreiber, Y. Pang, M.B. Brodsky and H. Sowers, *Phys. Rev. Lett.* **57**, 2442 (1986)

[2] C. F. Majkrzak, J.W. Cable, J. Kwo, M. Hong, D.B. McWhan, Y. Yafet, J.V. Waszcak and C. Vettier, *Phys. Rev. Lett.* **56**, 2700 (1986)

[3] M.B. Salamon, S. Sinha, J.J. Rhyne, J.E. Cunningham, R.W. Erwin, J. Borchers and C.P. Flynn, *Phys. Rev. Lett.* **56**, 259 (1986)

[4] G. Binasch, P. Grünberg, F. Saurenbach and W. Zinn, *Phys. Rev. B* **39**, 4828 (1989)

[5] M.N. Baibich, J.M. Broto, A. Fert, F. Nguyen Van Dau, F. Petroff, P. Etienne, G. Creuzet, A. Friederich and J. Chazelas, *Phys. Rev. Lett.* **61**, 2472 (1988)

[6] R. Skomski and J.M.D. Coey, *IEEE Trans. Magn.* **29**, 2860 (1993)

[7] R. Skomski and J.M.D. Coey, *Phys. Rev. B* **48**, 15812 (1993)

[8] D. Suess, T. Schrefl, R. Dittrich, M. Kirschner, F. Dorfbauer, G. Hrkac and J. Fidler, *J. Magn. Magn. Mater.* **290**, 551 (2005)

[9] R.H. Victoria and X. Shen, *IEEE Trans. Magn.* **41**, 537 (2005)

[10] D. Suess, T. Schrefl, S. Fahler, M. Kirschner, G. Hrkac, F. Dorfbauer and J. Fidler, *Appl. Phys. Lett.* **87**, 12504 (2005)

[11] S.N. Gordeev, J-M.L. Beaujour, G.J. Bowden, B.D. Rainford, P.A.J. de Groot, R.C.C. Ward, M.R. Wells and A.G.M. Jansen, *Phys. Rev. Lett.* **87**, 186808 (2001)

[12] J-M.L. Beaujour, S.N. Gordeev, G.J. Bowden, P.A.J. de Groot, B.D. Rainford, R.C.C. Ward and M.R. Wells, *Appl. Phys. Lett.* **78**, 964 (2001)

[13] M. Sawicki, G.J. Bowden, P.A.J. de Groot, B.D. Rainford, J-M.L. Beaujour, R.C.C. Ward and M.R. Wells, *Appl. Phys. Lett.* **77**, 573 (2000)

[14] M. Sawicki, G.J. Bowden, P.A.J. de Groot, B.D. Rainford, J-M.L. Beaujour, R.C.C. Ward and M.R. Wells, *Phys. Rev. B* **62**, 5817 (2000)

[15] K.N. Martin, K. Wang, G.J. Bowden, A.A. Zhukov, P.A.J. de Groot, J.P. Zimmermann, H. Fangohr and R.C.C. Ward, *Appl. Phys. Lett.* **89**, 132511 (2006)

[16] K.N. Martin, C. Morrison, G.J. Bowden and P.A.J. de Groot, *Phys. Rev. B* **78**, 172401 (2008)

[17] M. A. Ruderman, and C. Kittel, *Phys. Rev.* **96**, 99 (1954)

[18] T. Kasuya, *Prog. Theor. Phys.* **16**, 45 (1956)

[19] K. Yosida, *Phys. Rev.* **106**, 893 (1957)

[20] L. Berger, *J. Appl. Phys.* **3**, 2156 (1978)

[21] P.P. Freitas and L. Berger, *J. Appl. Phys* **57** 1266 (1985)

[22] L. Berger, *Phys. Rev. B* **54**, 9353 (1996)

[23] J.C. Slonczewski, *J. Magn. Magn. Mater.* **159**, L1 (1996)

[24] M. Tsoi, A.G.M. Jansen, J. Bass, W.C. Chiang, M. Seck, V. Tsoi and P. Wyder, *Phys. Rev. Lett* **80**, 4281 (1998)

[25] E.B. Myers, D.C. Ralph, J.A. Katine, R.N. Louie and R.A. Buhrman, *Science* **285**, 867 (1999)

[26] J.A. Katine, F.J. Albert, R.A. Buhrman, E.B. Myers, D.C. Ralph, *Phys. Rev. Lett.* **84** 3149 (2000)

[27] J.C. Slonczewski, *J. Magn. Magn. Mater.* **195**, L261 (1999)

[28] M. Sagawa, S. Hirosawa, H. Yamamoto, S. Fujimura and Y. Matsuura, *Jpn. J. Appl. Phys.* **26,** 785 (1987)

[29] E.E. Fullerton, J.S. Jiang, M. Grimsditch, C.H. Sowers and S.D. Bader, *Phys. Rev. B* **58**, 12193 (1998)

[30] E. F. Kneller and R. Hawig, *IEEE Trans. Magn.* **27**, 3588 (1991)

[31] M. Franchin, G. Bordignon, T. Fischbacher, G. Meier, J. Zimmermann, P.A.J. de Groot and H. Fangohr, *J. Appl. Phys.* **103**, 07A504 (2008)

[32] R. C. O'Handley, Modern Magnetic Materials, *Wiley Inter-Science*, 2000

[33] R. Stuart, and W. Marshall, *Phys. Rev.* **120**, 353 (1960).

[34] C. Zener, *Phys. Rev.* **81**, 440 (1951)

[35] C. Zener, Phys. Rev. **83**, 299 (1951)

[36] M. B. Stearns, *Phys. Rev.* **129**, 1136 (1963)

[37] M. B. Stearns, *Phys. Rev.* **147**, 439 (1966)

[38] M. B. Stearns, *Phys. Rev. B* **4**, 4069 (1971)

[39] M. B. Stearns, *Phys. Rev. B* **4**, 4081 (1971)

[40] M. B. Stearns, *Phys. Today* **31**, 34 (1978)

[41] I.A. Campbell, *J. Phys. F* **2**, L47 (1972)

[42] H. B. Callen, and E. Callen, *J. Phys. Chem. Solids* **27**, 1271 (1966)

[43] U. Atzmony and M.P. Dariel, *Phys. Rev. B* **10**, 2060 (1974)

[44] G. Dublon, U. Atzmony, M.P. Dariel and H. Shaked, *Phys. Rev. B* **12**, 4628 (1975)

[45] U. Atzmony, and M. P. Dariel, *Phys. Rev. B* **13**, 4006 (1976)

[46] K. N. Martin, P. A. J. de Groot, B. D. Rainford, K. Wang, G. J. Bowden, J. P. Zimmermann and H. Fangohr, *J. Phys. Cond. Matter.* **18**, 459 (2006)

[47] A. Mougin, C. Dufour, K. Dumesnil, N. Maloufi, Ph. Mangin and G. Patrat, *Phys. Rev. B* **59**, 5950 (1999)

[48] A. Mougin, C. Dufour, K. Dumesnil, and Ph. Mangin, *Phys. Rev. B* **62**, 9517 (2000)

[49] I.K. Yanson, *Sov. Phys.-JETP* **39**, 506 (1974)

[50] A.G.M. Jansen, F.M. Mueller and P. Wyder, *Phys. Rev.B* **16**, 1325 (1977)

[51] A.G.M. Jansen, J.H. van den Bosch, H. van Kempen, J.H.J.M. Ribot, P.H.H. Smeets and P Wyder, *J. Phys. F: Metal Phys.* **10**, 265 (1980)

[52] J.C. Maxwell, *A Treatise on Electricity and Magnetism*, 1904

[53] M. Knudsen, *Kinetic Theory of Gases*, 1934

[54] Yu.V. Sharvin, *Sov. Phys.-JETP* **21**, 655 (1965)

[55] A.G.M. Jansen, A.P. van Gelder and P. Wyder, *J. Phys. C: Solid St. Phys.* **13**, 6073 (1980)

[56] G. Wexler, *Proc. Phys. Soc.* **89**, 927 (1966)

[57] P.A.M. Dirac, *Proc. R. Soc. Lond. A* **114**, 243 (1927)

[58] A.F. Andreev, *Sov. Phys.-JETP* **19**, 1228 (1964)

[59] Yu V. Sharvin, *Sov. Phys.-JETP* **21**, 655 (1965)

[60] B. Nadgorny, I.I. Mazin, M. Osofsky, R.J. Soulen Jr., P. Broussard, R.M. Stroud, D.J. Singh, V.G. Harris, A. Arsenov and Ya. Mukovskii, *Phys. Rev. B* **63**, 184433 (2001)

[61] I.I. Mazin, *Phys. Rev. Lett.* **83**, 1427 (1999)

[62] R.J. Soulen Jr., J.M. Byers, M.S. Osofsky, B. Nadgorny, T. Ambrose, S.F. Cheng, P.R. Broussard, C.T. Tanaka, J. Nowak, J.S. Moodera, A. Barry and J.M.D. Coey, *Science* **282**, 85 (1998)

[63] G. E. Blonder, M. Tinkham and T. M. Klapwijk, *Phys. Rev. B* **25**, 4515 (1982)

[64] I. I. Mazin, A. A. Golubov and B. Nadgorny, *J. Appl. Phys.* **89**, 7576 (2001)

[65] G.J. Strijkers, Y, Ji, F.Y. Yang, C.L. Chien and J.M. Byers, *Phys. Rev. B* **63**, 104510 (2001)

[66] G.E. Blonder and M. Tinkham, *Phys. Rev. B* **27**, 112 (1983)

[67] A. Pleceník, M. Grajcar, S. Beňačka, P. Seidel and A. Pfuch, *Phys. Rev. B* **49**, 10016 (1994)

[68] R. Häussler, G. Goll, Yu.G. Naidyuk and H.v. Löhneysen, *Physica B* **218**, 197 (1996)

[69] L.F. Rybaltchenko, I.K. Yanson, A.G.M. Jansen, P. Mandal, P. Wyder, C.V. Tomy and D.McK. Paul, *Physica B* **218**, 189 (1996)

[70] Shashi K. Upadhyay, Akilan Palanisami, Richard N. Louie and R.A. Buhrman, *Phys. Rev. Lett.* **81**, 3247 (1998)

[71] M.J.M de Jong and C.W.J. Beenakker, *Phys. Rev. Lett* **74**, 1657 (1995)

[72] S.K. Upadhyay, R.N. Louie and R.A. Buhrman, *Appl. Phys. Lett.* **74**, 3881 (1999)

[73] D.J. Monsma and S.S.P. Parkin, *Appl. Phys. Lett.* **77**, 720 (2000)

[74] M. Tinkham, Introduction to Superconductivity, *McGraw-Hill Publishing*, 1996

[75] M.S. Osofsky, B. Nadgorny, R.J. Soulen Jr., P. Broussard, M. Rubinstein, J. Byers, G. Laprade, Y.M. Mukovskii, D. Shulyatev and A. Arsenov, *J. Appl. Phys.* **85**, 5567 (1999)

[76] B. Nadgorny, I.I. Mazin, M. Osofsky, R.J. Soulen Jr., P. Broussard, R.M. Stroud, D.J. Singh, V.G. Harris, A. Arsenov and Ya. Mukovskii, *Phys. Rev. B* **63**, 184433 (2001)

[77] Y. Ji, C.L. Chien, Y. Tomioka and Y. Tokura, *Phys. Rev. B* **66**, 012410 (2002)

[78] K. Xia, P.J. Kelly, G.E.W. Bauer and I. Turek, *Phys. Rev. Lett.* **89**, 166603 (2002)

[79] G.T. Woods, R.J. Soulen Jr., I.Mazin, B. Nadgorny, M.S. Osofsky, J. Sanders, H. Srikanth, W.F. Engelhoff and R. Datla, *Phys Rev. B* **70**, 054416 (2004)

[80] A.A. Abrikosov and L.P. Gor'kov, *Sov. Phys. JETP* **12**, 1243 (1961)

[81] N. Auth, G. Jacob, T. Block and C. Felser, *Phys. Rev. B* **68**, 024403 (2003)

[82] Electron Microscopy and Analysis 3rd Ed., P. J. Goodhew, J. Humphreys and R. Beanland, *Taylor and Francis* (2001)

[83] M.J. Bentall, R.C.C. Ward, E.J. Grier and M.R. Wells, *J. Phys.: Condens. Matter* **15**, 6493 (2003)

[84] P.J. Kelly and R.D.Arnell, *Vacuum* **56**, 159 (2000)

[85] M. Tinkham, *Introduction to Superconductivity*, McGraw-Hill Publishing 1996

[86] G. Sheet, S. Mukhopadhyay and P. Raychaudhuri, *Phys. Rev. B* **69**, 134507 (2004)

[87] A. Pleceník, M. Grajcar, Š. Beňačka, P. Seidel and A. Pfuch, *Phys. Rev. B* **49**, 10016 (1994)

[88] Y. Bugoslavsky, Y. Miyoshi, S.K. Clowes, W.R. Branford, M. Lake, I. Brown, A.D. Caplin and L.F. Cohen, *Phys. Rev. B* **71**, 104523 (2005)

[89] Y. Ji, G.J. Strijkers, F.Y. Yang, C.L. Chien, J.M. Byers, A. Anguelouch, Gang Xiao and A. Gupta, *Phys. Rev. Lett.* **86**, 5585 (2001)

[90] C.H. Kant, O. Kurnosikov, A.T. Filip, P. LeClair, H.J.M. Swagten and W.J.M de Jonge, *Phys. Rev. B* **66**, 212403 (2002)

[91] F.J. Jedema, M.S. Nijboer, A.T. Filip and B.J. van Wees, *Phys. Rev. B* **67**, 085319 (2003)

[92] F. J. Albert, N. C. Emley, E. B. Myers, D. C. Ralph, and R. A. Buhrman, *Phys. Rev. Lett.* **89**, 226802 (2002)

[93] J.M. Valentine and C.L. Chien, *J. Appl. Phys.* **99**, 08P902 (2006)

[94] S.X. Huang, T.Y. Chen and C.L. Chien, *App. Phys. Lett.* **92**, 242509 (2008)

[95] E.E. Fullerton, J.S. Jiang and S.D. Bader, *J. Magn. Magn. Mater.* **200**, 392 (1999)

[96] K. Dumesnil, M. Dutheil, C. Dufour and Ph. Mangin, *Phys. Rev. B* **62**, 1136 (2000)

[97] R. Jones, Clarendon Laboratory, Oxford (Private communication)

[98] M.S.S. Brooks, L. Nordström and B. Johansson, *J. Phys.: Condens. Matter* **3**, 2357 (1991)

[99] K. Bussman, G.A. Prinz, S.F. Cheng and D. Wang, *App. Phys. Lett.* **75**, 2476 (1999)

[100] S. Mühlbauer, C. Pfleiderer, P. Böni, M. Laver, E. M. Forgan, D. Fort, U. Keiderling and G. Behr, *Phys. Rev. Lett.* **102**, 136408 (2009)

[101] R. Coehoorn, *Phys. Rev. B* **39**, 13072 (1989)

[102] M.J. Bentall, R.A. Cowley, W.J.L Buyers, Z. Tun, W. Lohstroh, R.C.C. Ward and M.R. Wells, *J. Phys.: Condens. Matter* **15**, 4301 (2003)

[103] Y. Miyoshi, Y. Bugoslavsky and L.F. Cohen, *Phys. Rev. B* **72**, 012502 (2005)

[104] V Baltz, A D Naylor, K M Seemann, W Elder, S Sheen, K Westerholt, H Zabel, G Burnell, C H Marrows and B J Hickey, *J. Phys: Condens. Matter* **29**, 095701 (2009)

[105] S.M. Saini, N. Singh, T. Nautiyal and S. Auluck, *J. Phys: Condens. Matter* **19**, 176203 (2007)

[106] M. Tsoi, A.G.M. Jansen, J. Bass, W.-C. Chiang, V. Tsoi and P. Wyder, *Nature* **406**, 46 (2000)

[107] T.Y. Chen, Y. Ji, C.L. Chien and M.D. Stiles, *Phys. Rev. Lett.* **93**, 026601 (2004)

[108] Y. Ji, C.L. Chien and M. D. Stiles, *Phys. Rev. Lett.* **90**, 106601 (2003)

[109] K.N. Martin, *Characterizing the magnetic properties of $REFe_2$ exchange spring multilayers*, University of Southampton (2008)

[110] C. Kittel, *Introduction to Solid State Physics (Eighth Edition)*, Wiley Publishing 2005

[111] G. Shirane, V.J. Minkiewicz, and R. Nathans, *J. Appl. Phys.* 39, 383 (1968)

[112] T. Y. Chen, Z. Tesanovic, R. H. Liu, X. H. Chen and C. L. Chien, *Nature* **453**, 1224 (2008)

[113] K.A. Yates, L.F. Cohen, Zhi-An Ren, Jie Yang, Wei Lu, Xiao-Li Dong and Zhong-Xian Zhao, *Supercond. Sci. Technol.* **21**, 092003 (2008)

[114] P.M. Tedrow and R. Meservey, *Phys. Rev. Lett.* **26**, 192 (1971)

[115] P.D. Johnson, *Rep. Prog. Phys.* **60**, 1217 (1997)

[116] G.M. Müller, J. Walowski, M. Djordjevic, G-X. Miao, A. Gupta, A.V. Ramos, K. Gehrke, V. Moshnyaga, K. Samwer, J. Schmalhorst, A. Thomas, A. Hütten, G. Reiss, J.S. Moodera and M. Münzenberg, *Nature Materials* **8**, 56 (2009)

Publications

Magnetization reversal in micron-sized stripes of epitaxial (110) YFe_2 films
K. Wang, K.N. Martin, C. Morrison, R.C.C. Ward, G.J. Bowden, P.A.J. de Groot, *Phys. Stat. Sol. (a)* **203**, 3831 (2006)

Engineering coercivity in YFe_2 dominated $DyFe_2/YFe_2$ superlattice by patterning
K. Wang, K.N. Martin, C. Morrison, R.C.C. Ward, P.A.J. de Groot, *Appl. Phys. A* **86**, 325 (2007)

Investigation of magnetization reversal in micron-sized stripes of epitaxial-grown (1 1 0) Laves phase DyFe2 films
K. Wang, C. Morrison, K.N. Martin, R.C.C. Ward, G.J. Bowden, P.A.J. de Groot, *J. Alloys and Compounds* **440**, 23 (2007)

Magnetic anisotropy induced by patterning in (1 1 0) MBE-grown ternary Laves phase $TbDyFe_2$ films
K. Wang, K.N. Martin, C. Morrison, R.C.C. Ward, G.J. Bowden, P.A.J. de Groot, *J. Alloys and Compounds* **455**, 31 (2008)

Induced 3d and 4f magnetism in $Gd_{1-x}Pr_xNi_2$ Laves phase alloys
K Bouziane, C Carboni and C Morrison, *J. Phys: Condens. Matter* **20**, 025218 (2008)

Transition metal sublattice magnetization and the anomalous Hall effect in (110)-$ErFe_2/YFe_2$ multilayers
K.N. Martin, C. Morrison, G.J. Bowden, P.A.J. de Groot and R.C.C. Ward, *Phys. Rev. B* **78**, 172401 (2008)

Room temperature magneto optic exchange springs in $DyFe_2/YFe_2$ superlattices
D. Wang, C.G. Morrison, A.R. Buckingham, G.J. Bowden, R.C.C. Ward, P.A.J. de Groot, *J. Magn. Magn. Mater.* **321**, 586 (2009)

Determination of the Spin Polarization of $DyFe_2$ and YFe_2 Epitaxial Films by Point Contact Andreev Reflection
C. G. Morrison, D. Wang, G. J. Bowden, R. C. C. Ward and P. A. J. de Groot, submitted to *J. Magn. Magn. Mater.* (2009)